Stony Brook University

Dynamics of Atomic Matter Waves in Optical Lattices

A Dissertation Presented

by

Jeremy Brian Reeves

to

The Graduate School

in Partial Fulfillment of the Requirements

for the Degree of

Doctor of Philosophy

in

Physics

Stony Brook University

July 2015

Stony Brook University

The Graduate School

Jeremy Brian Reeves

We, the dissertation committee for the above candidate for the Doctor of Philosophy degree, hereby recommend acceptance of this dissertation.

Dominik A. Schneble – Dissertation Advisor
Associate Professor, Department of Physics and Astronomy

Thomas Bergeman – Chairperson of Defense
Adjunct Professor, Department of Physics and Astronomy

Mengkun Liu
Assistant Professor, Department of Physics and Astronomy

Robert Konik
Physicist
Brookhaven National Laboratory

This dissertation is accepted by the Graduate School.

Charles Taber
Dean of the Graduate School

Abstract of the Dissertation

Dynamics of Atomic Matter Waves in Optical Lattices

by

Jeremy Brian Reeves

Doctor of Philosophy

in

Physics

Stony Brook University

2015

Quantum gases in optical lattices allow for fundamental studies in atomic and condensed-matter physics and the exploration of novel effects. After a brief introduction to the fundamentals of quantum gas experiments in optical lattices, we discuss two recent experiments focusing on driven matter waves in a one-dimensional optical lattice.

The first experiment uses a tilted bichromatic optical lattice to investigate the interplay of disorder and collisional interactions in the accelerated transport of a Bose-Einstein condensate. Here, a screening effect is observed, in which the interactions effectively cancel the damping of Bloch oscillations induced by a (quasi-)disordered potential. This effect can be understood through a modification of the underlying band structure by the interactions.

The second experiment studies the dynamics of a weakly trapped condensate resonantly coupled to the orbitals of a strongly confining state-selective lattice. We observe momentum distributions

that correspond to matter wave diffraction from a periodic structure; however, the diffractive dynamics remain strongly linked to the internal-state Rabi oscillations. In the regime investigated, which we call the nonadiabatic regime, no diffracting potential can be defined. We show how only for much stronger coupling, the internal and external dynamics decouple, transitioning from nonadiabatic diffraction to the well-studied Kapitza-Dirac diffraction.

We further investigate prospects for realizing dissipative spin models in our ultracold atomic gas experiment. To this end, we develop and test in the laboratory several possible implementations of effective spins with differential coupling to a superfluid background and examine their viability for a realization of the spin-boson model.

Contents

List of Figures

Acknowledgements

Anyone who has known me these past six years knows I will do my best to keep this as brief as possible. However, it is impossible to overstate the support I have had from so many people during the process of my Ph.D. and I hope that I sufficiently recognize the impact you all have had on me, both personally and professionally.

I want to first thank my adviser Dominik Schneble, whose guidance and enthusiasm has made this long road as enjoyable and rewarding as it has been. Dominik has been an outstanding mentor and teacher from my first introductions to atomic physics and ultracold atoms in my first year as a graduate student to more recent discussions of the physical motivations and technical details of our experiments. In the lab, we can always count on Dominik for advice and motivation. His motivational powers were probably enhanced by his near constant presence in the laboratory. Lastly, he should be recognized as the driving force behind the fact that I began to drink any coffee at all.

I have had the pleasure of working with an outstanding group of physicists in the laboratory. Daniel Pertot and especially Bryce Gadway deserve many thanks for initiating me into the world of ultracold atoms and table-top experimental physics. Both of of my senior colleagues set a shining example to strive toward in their dedication and quality of lab work, that has certainly influenced my own work and will have a lasting impact on the culture of the lab. The younger generation of physicists in the lab have also been integral to the success of the lab and my own project. Ludwig Krinner is a constant source of solid physical intuition, Mike Stewart could always be counted on to arrive early and be ready to get the next set of experiments rolling and Arturo Pazmiño has been invaluable with technical support in his early days in the lab. It has been a pleasure to work with three so dedicated graduate students I want to thank each of them for useful discussions in the lab and at Friday socials, as well as time spent on the soccer field and on road trips. I eagerly look forward to hearing of your successes in the lab in the coming years.

My thesis committee has made the final steps of my Ph.D. official and I

want to thank each of Robert Konik, Mengkun Lui and Thomas Bergeman for their time in reading my dissertation and attending my defense. Tom Bergeman has been a constant resource for discussion and ideas across all aspects of my work the past several years. From working closely with us to model our experiments to pushing us with new ideas, Tom has been important in helping us refine our work in the lab. Martin Cohen has been a valuable help for the lab and myself, especially concerning optics in the lab, and his attentive reading of an early draft of my dissertation definitely help to iron out any kinks and inconsistencies.

The broader atomic physics community at Stony Brook has truly provided a great network for discussion both academic and otherwise. John, Brian, Vlad, Peter, Spencer, Arthur, Oumarou, Bertus, Mehdi, Carl and Vince are a great group of people and have made my time at Stony Brook a pleasure. I wish them all the best.

Beyond the atomic physicists, I would be remiss to leave out Rahul, Omer, Humed, and Josh; my roommates and friends since the first weeks of graduate school. These guys have made the graduate experience so much fun and it is been fantastic to see each of our lives and careers develop to where we are now. Moreover, I would like to thank anyone who has taken to a soccer field with me on Long Island. You all have provided a great outlet, without which I surely would have gone crazy.

My family has always been there to back me throughout my time at Stony Brook. My parents, Bob and Karen, have helped guide me through the challenges and been there to share in my excitement of successes in the lab. Jonathan, Mark and Ben have always been there for me and each has been an inspiration in their own way.

Last and far from least, a heartfelt thank you to Megan for being by my side throughout the entire Ph.D. and patiently sharing in my excitement and frustrations. Your support means all the more as you suffered long commutes and late nights to help make our lives together possible. And as we already begin our lives away from Long Island, I am excited to see what the future holds for us.

We thank IOP Publishing and the American Physical Society for the right to reproduce, in part, several works that are discussed in this thesis.

We are also thankful for the generous support of the Research Foundation of the State of New York, the Department of Education and the GAANN Program, as well as the National Science Foundation.

Chapter 1

Introduction

The 1995 achievement of Bose-Einstein condensation (BEC) in dilute atomic gases [1–3] provided the physics community with a nearly ideal, laser-like coherent matter wave having very narrow momentum spread. The realization of degenerate dilute gases was soon followed by the first experiments with BECs in optical lattice potentials. The early optical lattice experiments focused mostly on the dynamics of matter waves in the lattice. Interference of a BEC released from an adiabatically loaded optical lattice or after interaction with a pulsed potential takes advantage of its spectral narrowness to further refine atom optical techniques [4–8]. BECs in optical lattices readily allow for the study of single particle dynamics, as well as the effects of weak nonlinear interactions on a many body lattice system [9, 10]. Optical lattices further allowed for the study of interacting matter waves in reduced dimensions [11] and of strongly correlated systems [12–14]. These foundational experiments have kicked off the growing field of quantum simulation using ultracold atoms in optical lattices [15, 16].

In recent years, experiments in optical lattices have grown from the initial cubic lattices to include more complex lattice geometries, allowing for the simulation of increasingly complex quantum Hamiltonians [17, 18]. Experiments have also extended to include fermions, allowing for the study of ultracold atomic lattice systems having a more direct comparison with electrons in solid-state systems [19, 20]. Developments in optical lattice quantum simulation techniques have allowed for the study of orbital physics in superlattices [21, 22], and the study of quantum and classical magnetism [23–25], while graphene-like systems have allowed for the study of topological physics [26–28], and spin-orbit coupling from synthetic gauge-fields mimics the effects of large magnetic fields in electronic materials [29–33]. These experiments largely focus on single-band physics in the lattice, while recent efforts have begun to take advantage of the simultaneous use of multiple orbital degrees

of freedom to engineer the excitation spectra of interacting systems [34–36]. Building on experiments in the early 2000s, the most recent experimental efforts today take advantage of the many accessible degrees of freedom inherent to optical lattice systems including; internal states, orbital levels, and tunable interactions. The increased control over the atomic system is showcased by experiments in quantum-gas microscopes with single lattice site control [37–42] and the extremely precise optical lattice clocks [43–46].

Many of the above experiments use the precise control offered by ultracold atomic experiments to realize ideal versions of model Hamiltonians. Real condensed matter materials or systems do not always follow the ideal and the effects of imperfections or disorder can readily be investigated as well. Possible implementations of disorder in ultracold atom experiments include optical speckle [47–49], quasi-periodic lattices [50–52], and atomic disorder from localized impurities [53, 54]. Ultracold atoms provide an ideal system in which to study the properties and dynamics of systems beyond single particle disorder physics. The general behavior of disordered, interacting systems can be broken into two distinct regimes. For strong interactions, in the absence of disorder, it is possible to drive a transition to a localized state known as the Mott insulator [14]. In the presence of disorder, a gap-less insulating state known as the Bose glass replaces the gapped Mott insulator [54–56]. The Bose glass is distinguished by the cooperation of interactions and disorder to spatially localize particles. For weakly or noninteracting particles, disorder can independently drive an insulating transition via Anderson localization, resulting from the destructive interference of quantum mechanical trajectories [47, 51, 57–59]. In this limit, the introduction of weak interactions serves to destroy the Anderson localization, having a delocalizing effect [60, 61]. Recent work investigating this interplay has focused on the equilibrium properties of the interacting disordered system [62].

While this sampling of the applications of ultracold atoms optical lattice is far from comprehensive, it touches on some of the cutting edge of a broad, evolving field. In this thesis, we will focus on applications of weakly interacting Bose gases (matter waves) to the study of disordered systems and a novel regime of atom optical diffraction. We also touch on applications of these systems to designing open quantum systems to study dissipation and decoherence [63–65].

Weakly interacting matter waves in a disordered potential

Following from the study of interactions in strongly correlated lattices [54], we investigate the dynamics of a weakly interacting matter wave in a (quasi-) disordered potential. We study the delocalizing effect of interactions in the

dynamics of Bloch oscillations in a disordered potential. It is well known that disorder [66] and interactions [67] independently dephase Bloch oscillations, leading to damping of the collective motion. In our experiment, we observed that the presence of both disorder and weak interactions lead to competition between the two effects and an interaction induced reduction of the Bloch oscillation damping due to disorder. This effect saturates once the interactions are comparable to the disorder energy scale. The effects studied here can be related to the physics of granular superconductors [68] and other disordered materials such as superfluid helium in porous media [69].

Matter wave diffraction beyond the Born-Oppenheimer regime

Diffraction techniques have become invaluable to experiments using ultracold atoms for applications such as lattice characterization using Kapitza-Dirac diffraction [5], Bragg diffraction for spectroscopy [7], and for atom interferometry [70]. These applications and all previous work on atomic matter wave diffraction [71–73] have relied on the action of a potential. For atoms with internal structure interacting with optical fields, this potential corresponds to the optical potential, deriving from the dressed states of the light-atom system. Here, we present diffractive dynamics in a little explored regime in which the adiabatic potentials are insufficient to describe the time evolution of the system. The diffraction of a superfluid coupled via microwaves to the deep wells of a state-dependent optical lattice is studied. We realize strong coupling between the internal and external state dynamics, in contrast to the familiar regimes of Kapitza-Dirac and Bragg diffraction.

Engineering dissipative spin models

Isolating a quantum system from the environment is imperative for the study of many sensitive quantum effects. An understanding of the system-environment coupling, which typically leads to decoherence and dissipation, is critical for applications in quantum information science. Furthermore, these effects describe the emergence of classical physics in a world governed by quantum mechanics, and ultracold gases are uniquely poised to study such questions [63, 74]. In this context, it is important to identify a quantum system (in this case a spin-1/2) that couples controllably to some environment (in this case a superfluid bath) [75]. We will explore several possibilities for the formation of a pseudospin-1/2 with (potentially) differential spin-bath coupling in our apparatus and present some first studies on their experimental viability.

Outline of thesis

Chapter 2 will briefly outline the theory of BEC in weakly interacting dilute atomic gases and introduce relevant concepts from atomic physics used to trap and manipulate a BEC. With the necessary background established, Chapter 3 will describe experiments on Bloch oscillations of a weakly interacting BEC in bichromatic optical lattices. Here, we review the problem of disordered systems in the strong and weak interaction limit and go on to describe the properties of the bichromatic potential and its use as disorder in our experiments. The experiment and results are discussed and we present a microscopic model to capture the essential physics. Chapter 4 details experiments on matter wave diffraction in a dressed state-dependent optical lattice. A review of conventional matter wave diffraction from optical potentials is given. We then describe our experiments on Rabi oscillations in the presence of a state-dependent potential and highlight qualitative differences in the dynamics before giving an interpretation in terms of nonadiabatic dressed states. We describe, briefly, the possibility of implementing the diffraction scheme here to study dissipative systems and superfluid excitations. Building on this in Chapter 5, and following a brief introduction to the spin-boson model, we examine several mechanisms for realizing effective spins coupled to a superfluid bath and discuss the prospects for practical implementation of each. Finally, we make a few concluding remarks in Chapter 6.

Publications of this PhD work (described either in part or in full):

- Chapter 3
  Superfluid Bloch dynamics in an incommensurate optical lattice
  J. Reeves, B. Gadway, T. Bergeman, I. Danshita, and D. Schneble
  New Journal of Physics **16**, 065011 (2014)

- Chapter 4
  Nonadiabatic diffraction of matter waves
  J. Reeves, L. Krinner, M. Stewart, A. Pazmiño, and D. Schneble
  arXiv 1505.06085 Accepted for publication in Physical Review A (2015)

Chapter 2

Theoretical Background and Experimental Techniques

In this chapter, some of the basic physics behind the creation and manipulation of ultracold atoms will be introduced. There are many excellent reviews on the physics and creation of Bose-Einstein condensates and of ultracold atoms in optical lattices [10, 15, 76–78] and several textbooks have comprehensively covered the subject [16, 79, 80]. This chapter will give a brief review of theory of Bose-Einstein condensates and of important techniques relevant to the experiments described in this thesis.

2.1 Bose-Einstein condensates

From the conception of condensation of photons in 1924 by Bose and its subsequent generalization to particles by Einstein, to its realization in dilute atomic gases in 1995, the subject of Bose-Einstein condensation (BEC) has been of great interest in physics. The concept has found applications in the discussion of superfluid helium [81, 82] and the physics of superconductors, where a condensate of bosonic Cooper pairs occurs [83, 84]. BEC can be extended to the condensation of quasiparticles such as excitons and polaritons [85] and even to photons interacting with dye molecules [86]. The achievement of BEC in dilute atomic gases has since given birth to an ever growing field of research, taking advantage of the remarkable properties of quantum-degenerate gases.

2.1.1 Mean field description

Once cooled below degeneracy, the dilute and weakly interacting gas of bosonic atoms in three-dimensions is well described by a macroscopically populated

single-particle wave function $\Psi(\mathbf{r},t)$ subject to the nonlinear Gross-Pitaevskii equation (GPE) [79]

$$\left[-\frac{\hbar^2}{2m}\nabla^2 + V(\mathbf{r}) + g|\Psi(\mathbf{r},t)|^2\right]\Psi(\mathbf{r},t) = i\hbar\frac{\partial\Psi(\mathbf{r},t)}{\partial t} \tag{2.1}$$

where $V(\mathbf{r})$ describes some external potential. The effects of collisional interactions between atoms in the gas is modeled by the nonlinear term $g|\psi(\mathbf{r})|^2$, where $g = 4\pi\hbar^2 a_s/m$ is parametrized by the s-wave scattering length a_s. We typically work in the Thomas-Fermi approximation in which the kinetic energy term is neglected and we make the ansatz $\Psi(\mathbf{r},t) = \psi(\mathbf{r})\exp(-i\mu t/\hbar)$, with the chemical potential μ. The equilibrium density is thus given by

$$n(\mathbf{r}) = |\psi(\mathbf{r})|^2 = (\mu - V(\mathbf{r}))/g \qquad \text{for} \qquad \mu \geq V(\mathbf{r}). \tag{2.2}$$

In this case $\mu = gn(\mathbf{r}) + V(\mathbf{r})$, such that $gn(\mathbf{r})$ can be considered a local chemical potential, i.e. the energetic level to which the potential $V(\mathbf{r})$ is "filled" at position $\mathbf{r}$ by the condensate.

In addition to the ground state, we are also concerned with the elementary excitations of the condensate as well as its modes of collective motion. The elementary excitations can be found by linearizing the GPE about some change in the wave function $\psi(\mathbf{r},t) + \delta\psi(\mathbf{r},t)$; the result is the Bogoliubov spectrum with dispersion relation [79]

$$\epsilon(q) = \sqrt{\left(\frac{\hbar^2 q^2}{2m}\right)^2 + 2\mu\frac{\hbar^2 q^2}{2m}} \tag{2.3}$$

which is phonon-like (linear) for small q with speed of sound $v_s = \sqrt{\mu/m}$ and particle-like (quadratic) for large q. The length scale associated with the transition between phonon and particle excitations is given by the so-called healing length

$$\xi = \frac{1}{\sqrt{8\pi n a_s}}, \tag{2.4}$$

which is the characteristic length scale required to deform the condensate wave function. Excitations with energy $\epsilon(q) \gg \mu$ (or $2\pi/q \ll \xi$), act like free particles.

It is also of experimental interest to consider the low lying collective modes of a trapped BEC. For our purposes, we will assume the BEC occupies an isotropic harmonic trap of the form $V(\mathbf{r}) = 1/2m\omega^2\mathbf{r}^2$. The lowest energy collective excitations in such a trap correspond to linear center-of-mass motion of the entire condensate, or dipole oscillations. The dipole oscillation is

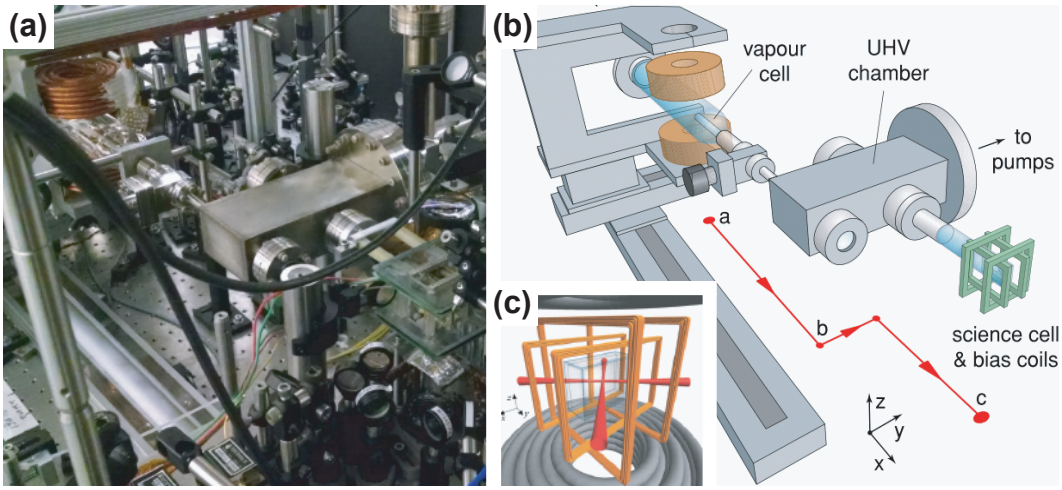

Figure 2.1: The experimental BEC apparatus. (a) Photograph showing the quadrupole field coils, vacuum chamber and science cell along with nearby optics. (b) Schematic drawing of the apparatus showing the main components of the machine. The red line represents the path followed by the transporter coils, including a "dog leg" to minimize ballistic collisions with the background vapor. (c) The science cell with crossed optical dipole trap and Helmholtz coil pairs (used to generate TOP trap in conjunction with the quadrupole coils). Drawing taken from [89].

characterized by a frequency ω and preserves the density profile throughout the collective motion. Such modes are easily excited by spatial displacement of the trap minimum and can be exploited to characterize the trapping potential [87]. Dipole oscillations also apply to anisotropic harmonic traps, where the anisotropic oscillation frequencies can be determined by excitation along different spatial directions. Higher energy collective motion can be excited by sudden squeezing of the trap to create a breathing mode or a scissors mode with oscillation frequencies dependent on the trap geometry [88].

2.1.2 Experimental apparatus

The experimental apparatus used throughout this thesis has been described in detail in [87, 89–91]. The important features of the apparatus will be briefly reviewed here; for reference the bulk of the machine is photographed and schematically drawn in Fig. 2.1. The BEC apparatus begins with a room temperature vapor of natural abundance rubidium (the rubidium source and ion pump maintain a background rubidium pressure of a few 10^{-9} torr). Diode lasers tuned to the ^{87}Rb D_2 line are used to laser cool the atoms in a magneto-

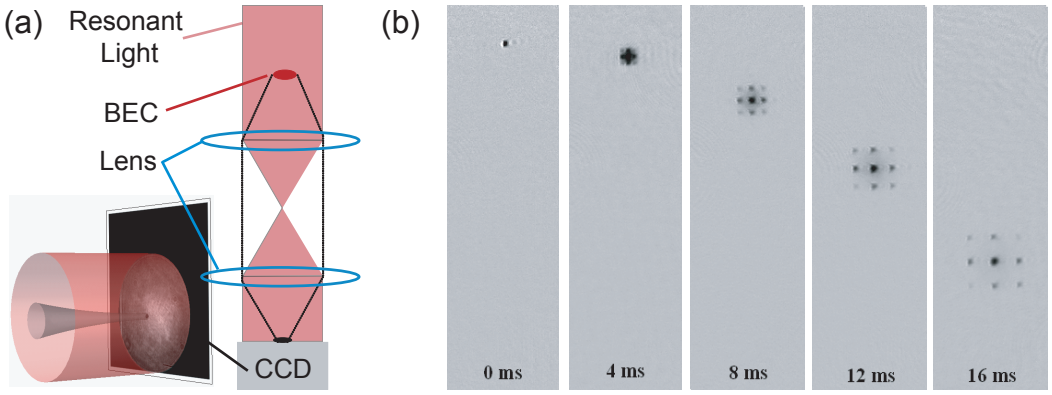

Figure 2.2: Schematic experimental imaging system. (a) Schematic drawing of the absorption imaging process and system. A pair of lenses project the shadow image of the atomic sample onto a CCD chip. Inset shows raw data for the imaging on a CCD of a cold atomic cloud. The transparent tubes represent resonant light and the cold cloud's shadow. (b) Example time-of-flight data following release of a BEC from a periodic optical potential.

optical trap (MOT) [92, 93] formed with a pair of moving quadupole coils. After loading the MOT and performing brief sub-Doppler cooling in an optical molasses [94, 95], the magnetic quadrupole trap is moved by a linear-motor driven translation stage through a differential pumping tube to a small glass "science cell" (maintained at $\sim 10^{-12}$ torr).

In the science cell, the cold atomic cloud is further cooled using forced rf-evaporation in a time orbiting potential (TOP) trap [96] before transfer into a crossed optical dipole trap formed by a pair of 1064 nm laser beams derived from a 20 Watt Ytterbium fiber laser. After a final stage of evaporation in the dipole trap, nearly pure BECs of $10^5 ... 10^6$ ^{87}Rb atoms are obtained with typical temperatures around 100 nK.

The BEC is then manipulated using a combination of optical potentials, magnetic field gradients, and microwave fields before being imaged in time-of-flight, c.f. Fig. 2.2. The imaging system uses resonant laser light to cast a shadow of the BEC on a CCD camera, after release from the optical trap and subsequent ballistic expansion. For sufficiently long time of flight, the captured shadow image reflects the momentum distribution of the trapped atoms and it contains information about the shape, coherence and collective motion of the atomic cloud.

2.2 Atom-light interaction

Many of the most important tools used throughout ultracold atom experiments can be understood by examining the interaction of a simple two-level atom with a classical radiation field. In the case of coupling to an optical field, the interaction consists of dissipative and conservative contributions. The dissipative effects caused by absorption and spontaneous re-emission of photons by atoms are of central importance for laser cooling and trapping [93]. We focus here on the conservative effects associated with the dressing of atomic energy levels by the applied radiation field. The so called light shift (or ac-Stark shift) results from the interaction of the induced dipole moment of the atom with the driving light field. In the presence of spatially inhomogeneous intensity this shift can be utilized in the creation of potential wells or barriers for the confinement of atoms in free space [97]. In the last section, we then generalize the treatment of the two-level atom to that of multilevel atoms and introduce effects beyond those described in the two-level picture.

2.2.1 Interaction Hamiltonian and Rabi oscillations

We begin with a simple atom consisting of a ground state $|g\rangle$ and an excited state $|e\rangle$ with energy separation $\hbar\omega_0 = E_e - E_g$. Consider the atom's interaction with a monochromatic field of the form $\mathbf{E}(\mathbf{r},t) = E_0(x,y)\hat{\epsilon}\cos(\omega t - kz)$ propagating along the $\hat{z}$-axis with polarization vector $\hat{\epsilon}$ (we will ignore the coupling to the magnetic field $\mathbf{B}$ for now as its magnitude is reduced by a factor of speed of light c). We can then write the system Hamiltonian as sum of the free atom H_a and the atom-field interaction H_int as

$$H = H_\mathrm{a} + H_\mathrm{int} = \hbar\omega_0|e\rangle\langle e| - \mathbf{d}\cdot\mathbf{E}(0,t) \tag{2.5}$$

where we have made the dipole approximation, and dropped the spatial dependence of the field, with atomic dipole operator $\mathbf{d} = -e\mathbf{r}_e$ for positive fundamental charge e. The ground state energy has been set to 0. Writing the dipole operator in terms of the atomic states yields $\mathbf{d} = \langle g|\mathbf{d}|e\rangle(|g\rangle\langle e| + |e\rangle\langle g|)$ (if $|g\rangle$ and $|e\rangle$ have the same parity we simply have $\langle g|\mathbf{d}|e\rangle = 0$). Thus we can rewrite the interaction term as

$$H_\mathrm{int} = -\langle g|ed|e\rangle\left(|g\rangle\langle e|e^{-i\omega_0 t} + |e\rangle\langle g|e^{i\omega_0 t}\right)\left(\frac{E_0^*}{2}e^{i\omega t} + \frac{E_0}{2}e^{-i\omega t}\right), \tag{2.6}$$

assuming $\mathbf{d} = d\hat{\epsilon}$; for a two level atom the atomic polarization is always along the field $\hat{\epsilon}$ [93]. For near resonant light $\omega_0 \approx \omega$, the cross terms in Eq. 2.6 carrying rapidly oscillating terms $\exp\left[\pm i(\omega_0+\omega)t\right]$ can be neglected (making

the rotating wave approximation) and H_{int} can be further simplified to

$$H_{\text{int}} \approx |e\rangle\langle g|\frac{\hbar\omega_R}{2}e^{-i\delta t} + |g\rangle\langle e|\frac{\hbar\omega_R}{2}e^{i\delta t}. \tag{2.7}$$

Here, we have introduced the Rabi frequency $\omega_R = eE_0\langle g|d|e\rangle/\hbar$ and the detuning $\delta = \omega - \omega_0$. The terms of the Hamiltonian simply represent the excitation (de-excitation) of the two-level atom by absorption (emission) of a photon. In this form we can solve for the dynamics of the atomic system by applying the time-dependent Schrödinger equation with the ansatz $|\psi\rangle = c_g|g\rangle + c_e|e\rangle$. The equations of motion for the population amplitudes can thus be written as

$$\begin{aligned} i\dot{c_g} &= \frac{\omega_R}{2}c_e \\ i\dot{c_e} &= \delta c_e - \frac{\omega_R}{2}c_g, \end{aligned} \tag{2.8}$$

The solution of Eq. 2.8 describes Rabi oscillations of the internal state populations

$$\begin{aligned} P_e(t) &= |c_e|^2 = \left(\frac{\omega_R}{\Omega_R}\right)^2 \sin^2\left(\frac{\Omega_R}{2}t\right) \\ P_g(t) &= |c_g|^2 = 1 - P_e(t) \end{aligned} \tag{2.9}$$

with generalized Rabi frequency $\Omega_R = \sqrt{\omega_R^2 + \delta^2}$. For resonant coupling $\delta = 0$, Eq. 2.9 predicts full contrast oscillations of the population, while driving off-resonance reduces the amplitude and increases the oscillation frequency as seen in Fig. 2.3. Under realistic conditions, long lived oscillations using optical transitions are limited by the short lifetime of the excited state leading to damping due to dephasing for an ensemble of atoms.

2.2.2 Dressed states and dipole potentials

While resonant light fields drive transitions between the internal states, off-resonant fields still shift the energy levels of the atom. The previous section focused on dynamics in the basis of atomic eigenstates; here we consider the eigenstates (dressed states) of the total light-atom system [93]. For this purpose, it is useful to write Eq. 2.8 in matrix form

$$H = \frac{\hbar}{2}\begin{pmatrix} -2\delta & \omega_R \\ \omega_R & 0 \end{pmatrix} \tag{2.10}$$

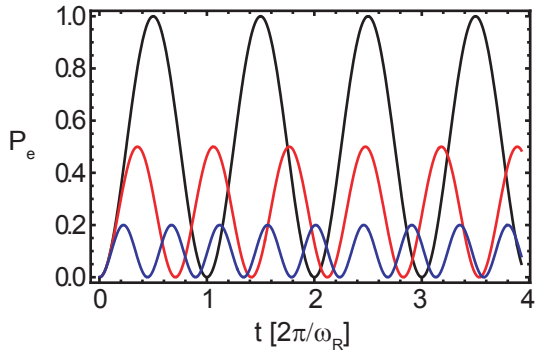

Figure 2.3: Rabi oscillations of the excited state population $P_e(t)$ of a two-level system are plotted for $\delta/\omega_R = 0$ (black), 1 (red), 2 (blue).

and then diagonalize it to find the "dressed" eigenstates and eigenenergies corresponding to the atom-field system. The dressed states are given by,

$$|\chi_+\rangle = \cos\theta|g\rangle - \sin\theta|e\rangle \qquad \text{and} \qquad |\chi_-\rangle = \sin\theta|g\rangle + \cos\theta|e\rangle, \tag{2.11}$$

where θ is the mixing angle, with $\cos(2\theta) = -\delta/\Omega_R$. The dressed states have energies

$$E_\pm = \frac{\hbar}{2}(-\delta \pm \Omega_R). \tag{2.12}$$

For an off resonant field $\delta^2 \gg \omega_R^2$ and $\delta < 0$, the mixing angle $\theta \approx 0$ and the dressed states are nearly given by the bare states, i.e. $|\chi_-\rangle \approx |g\rangle$ and $|\chi_+\rangle \approx |e\rangle$ (and vice versa for $\delta > 0$). In this limit the energy shifts are given by

$$E_g = \frac{\hbar\omega_R^2}{4\delta} \qquad \text{and} \qquad E_e = -\frac{\hbar\omega_R^2}{4\delta}. \tag{2.13}$$

Utilizing spatially dependent Rabi frequencies, these energy shifts can be used to produce optical traps and potential barriers. The optical fields are most typically derived from laser beams with Gaussian profile such that $E_0(x,y) \propto \exp\left[-(x^2+y^2)/w^2(z)\right]$ with beam radius $w(z)$. Since the intensity of the laser field can be related to the Rabi frequency through $I(\mathbf{r}) \propto |E_0|^2 \propto \omega_R^2$, the spatially dependent energy shifts give rise to a force known as the optical dipole force. Moreover, since the energy shift depends on the sign of the detuning, optical dipole traps (barriers) for ground-state atoms can be formed for red $\delta < 0$ (blue $\delta > 0$) detuned optical fields.

It is important to keep in mind that the optical potentials actually correspond to the dressed states of the atom, with generally non-negligible contribu-

tions of both ground and excited states. Thus, it is also necessary to consider the effect of spontaneous scattering. The exact (rotating wave) expressions for the dipole potentials and the scattering rate are given by [97]

$$V_{\rm dip}(\mathbf{r}) = \frac{3\pi c^2}{2\omega_0^3}\frac{\Gamma}{\delta}I(\mathbf{r}), \tag{2.14}$$

$$\Gamma_{\rm sc}(\mathbf{r}) = \frac{3\pi c^2}{2\hbar\omega_0^3}\left(\frac{\Gamma}{\delta}\right)^2 I(\mathbf{r}), \tag{2.15}$$

where the excited state decay rate Γ is given by

$$\Gamma = \frac{\omega_0^3|\mathbf{d}|^2}{3\pi\epsilon_0\hbar c^3}, \tag{2.16}$$

following the work of Wigner and Weisskopf [93].* For off-resonant fields, the scattering rate falls off as δ^{-2}, while the potential only falls off as δ^{-1}. This dependence on the scattering rate calls for the use of larger laser powers $P \propto I$ and larger detunings in order to minimize, for a given potential depth, the unwanted effects of spontaneous photon scattering. The light-induced dissipative effects of photon scattering typically lead to heating and the decay of any coherent dynamics in ultracold atomic samples.

2.2.3 State-dependent optical potentials

Though the two-level description gives good intuition about the effect of an ac electric field's interaction with an atom, it is not always possible or even desirable to isolate a single two-level optical transition. The energy shifts described above are linear in the light intensity and second order in electric field E_0. Thus, second order perturbation theory for a given state $|i\rangle$ with energy E_i (in the following we set the bare atom energy $E_i = 0$ for convenience) in a multilevel system yields the level shifts according to

$$\Delta E_i = \sum_{i\neq j}\frac{|\langle j|H_{\rm int}|i\rangle|^2}{E_i - E_j}, \tag{2.17}$$

where the sum is taken over all other internal states $|j\rangle$ of the atom. Including the driving field, the ground state atom plus light system has energy $E_i = n\hbar\omega$ assuming that the field contains n photons. The system with an excited atom then has energy $E_j = \hbar\omega_0 + (n-1)\hbar\omega = \hbar\delta_{i,j} + n\hbar\omega$; we thus replace the

*Hence, the Rabi frequency is given by $\omega_R = \Gamma\sqrt{I/2I_s}$, where $I_s = 2\pi\hbar c\Gamma/(3\lambda^3)$, with $\lambda = 2\pi c/\omega$, is the saturation intensity.

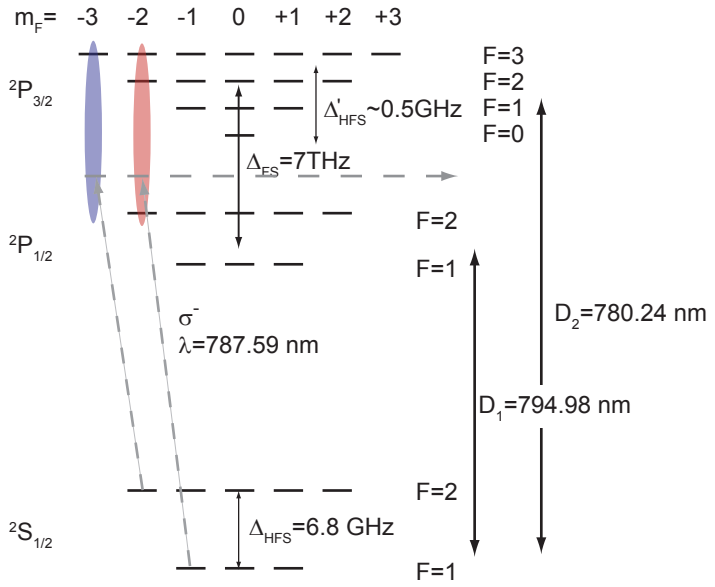

Figure 2.4: Electronic level structure of rubidium-87 [98]. The excited state is split by Δ_{FS} by spin-orbit coupling of the orbital and spin angular momentum. Each fine structure manifold is further split, by coupling to the $I = 3/2$ nuclear spin, into hyperfine levels with typical energy scales Δ_{HFS} and Δ'_{HFS}. For specific applied light fields, for instance σ^- light at 787.59 nm, the ac-Stark shift for specific $S_{1/2}$ levels can be tuned to 0. In the example shown, $|2, -2\rangle$ only couples to a single excited state (shaded in blue), experiencing a two-level light shift. On the other hand, $|1, -1\rangle$ couples to several states (shaded in red) in both hyperfine manifolds, and the net ac-Stark energy shift vanishes.

denominator in Eq. 2.17 with the detuning for each state pair $\delta_{i,j}$. For a two-level atom, we can readily show that this reproduces the result given in Eq. 2.15.

For multilevel atoms, the two-level result generalizes to

$$\Delta E_i = \frac{3\pi c^2}{2} I \sum_{j \neq i} \frac{\Gamma_j c_{i,j}^2}{\omega_{i,j}^3 \delta_{i,j}}, \tag{2.18}$$

where we have already ignored the counter-rotating terms[†] and reduced the

[†]The counter-rotating term is nonnegligible for very large detunings and should generally be included. For now, we concern ourselves with light fields near enough to resonance to justify this exclusion.

matrix elements to transition strengths (Clebsch-Gordan coefficients) $c_{i,j} = \langle F', m'_F | F, 1, m_F, q\rangle$ for initial and final states $|i\rangle = |F, m_F\rangle$ and $|j\rangle = |F', m'_F\rangle$ with a spin-1 photon having polarization $q = 0, \pm 1$ corresponding to linear or $\sigma^{\pm}$ polarization with respect to the quantization axis [93, 97].

We are most concerned with the case of alkali atoms, which have a single unpaired electron in their valence shell and two strong optical transitions in the form of the D_1 and D_2 lines, c.f. Fig. 2.4. We can then recast Eq. 2.18 as [91]

$$\Delta E_i = \frac{3\pi c^2}{2} I \left[\frac{\Gamma_{D_1}}{\omega_{D_1}^3} \sum_j \frac{c_{i,j}^2}{\delta_{i,j}} + \frac{\Gamma_{D_2}}{\omega_{D_2}^3} \sum_k 2 \frac{c_{i,k}^2}{\delta_{i,k}} \right], \tag{2.19}$$

where the sums over j and k are over the states in the $^2P_{1/2}$ and $^2P_{3/2}$ manifolds respectively. For a given polarization q and initial state $|i\rangle$ the participating excited states will be limited to those allowed by dipole selection rules. The factor of 2 in the D_2 sum accounts for the effective line strength compared to the D_1 line.

For most applications, we will be working with detunings that are large compared to the splittings within the hyperfine manifolds (few 100 MHz), but small compared to the fine structure splitting ($\sim$ 7 THz). In the case of effectively unresolved F levels, we can greatly simplify Eq. 2.19 to [99]

$$\Delta E_i = \frac{\pi c^2 \Gamma}{2} I \left(\frac{2 + q g_F m_F}{\Delta_{2,F}} + \frac{1 - q g_F m_F}{\Delta_{1,F}} \right), \tag{2.20}$$

where we have taken $\Gamma_{D_1}/\omega_{D_1}^3 \approx \Gamma_{D_2}/\omega_{D_2}^3 \approx \Gamma/\omega_0^3$ and introduced the Landé factor g_F of the considered hyperfine ground state $|i\rangle = |F, m_F\rangle$. In this form, it is easy to see that for a given m_F state and q, with ω tuned between the D_1 and D_2 transitions, a competition can be engineered between the first and second terms in the brackets, as the detunings from the D_2 and D_1 lines $\Delta_{2,F}$ and $\Delta_{1,F}$ can take on opposite signs. This allows for the simultaneous production of an optical potential for one m_F state while another experiences no ac-Stark shift. In our experiment, we typically use the state pair $|2, -2\rangle$ and $|1, -1\rangle$ for one implementation of this so called "tune-out" scheme, as shown in Fig. 2.4. Other possible configurations of such a lattice are further described in [100]. Optical potentials for a few such configurations are plotted in Fig. 2.5; the potentials are calculated using Eq. 2.19.

As the driving optical field is still close to resonance in this configuration, the admixture of excited states due to the field is relatively high, and spontaneous scattering from these excited state components must be considered.

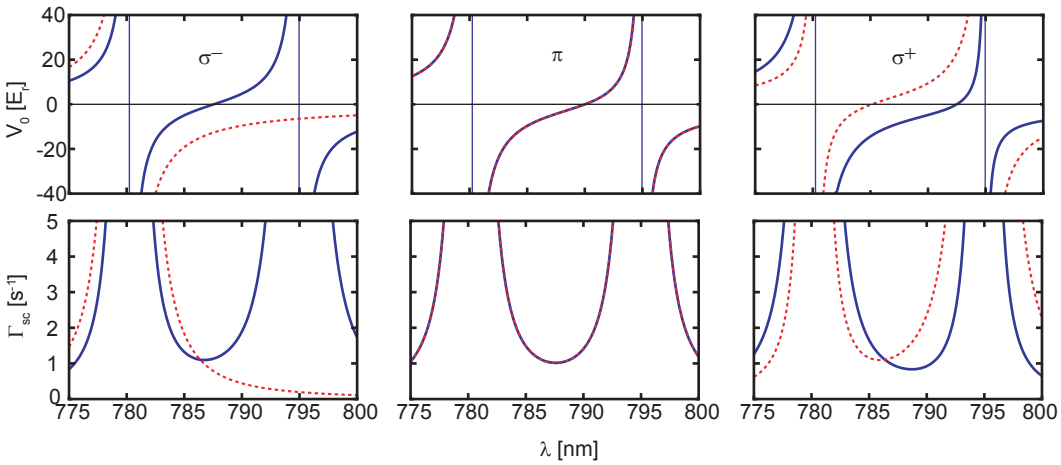

Figure 2.5: State-dependent potentials and scattering rates. (a) Potential depths for an optical standing wave formed by a counter-propagating pair of Gaussian beams with waist $w = 1$ mm and with power 0.75 W. Red, dashed (blue, solid) lines correspond to $|2,-2\rangle$ ($|1,-1\rangle$).Plotted from left to right are q=-1,0,1. (b) Spontaneous scattering rates for an atom trapped in the potential minima formed by the above configuration.

Generalizing Eq. 2.15 and Eq. 2.17 we can write

$$\Gamma_{\mathrm{sc},i} = \frac{1}{2\epsilon_0 c\hbar^2} I \sum_{j\neq i} \frac{\Gamma_j |\langle j|H_{\mathrm{int}}|i\rangle|^2}{\delta_{i,j}^2}. \tag{2.21}$$

Scattering rates, calculated after applying this to the D_1 and D_2 transitions separately, are plotted in Fig. 2.5. For typical intensities applied here, the scattering rates are on the order of a few Hz, which is acceptable for experiments occurring on timescales up to ~ 100 ms.

2.2.4 Two-level dynamics in the ^{87}Rb ground state

The rubidium ground state provides an ideal system for the resonant two-level physics described above, using magnetic-dipole transitions between hyperfine levels. As ^{87}Rb is an alkali atom with a single electron of $J = 1/2$ and nuclear spin $I = 3/2$, its ground state is split into manifolds with total angular momentum $F = 1, 2$ separated by $\Delta_{\mathrm{HFS}} \approx h \times 6.8$ GHz, c.f. Fig. 2.4. In a weak magnetic field these states are described by the Zeeman-split sublevels $|F, m_F\rangle$ with angular momentum projection onto the quantization axis $m_F =$

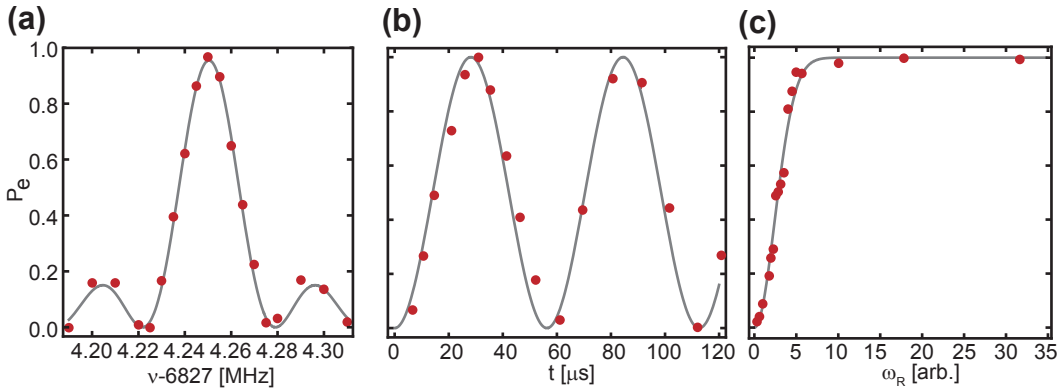

Figure 2.6: Hyperfine-ground state control with applied microwave fields. (a) Typical microwave resonance measured using a Rabi π-pulse with $\omega_R \approx 2\pi \times 17$ kHz and $\tau = 28$ μs. The peak width is given by the Fourier width of the applied square pulse. (b) Resonant Rabi oscillations between $|1, -1\rangle$ and $|2, -2\rangle$ hyperfine sublevels, with $\omega_R = 2\pi \times 17.5$ kHz. (c) Landau-Zener transitions between the same sub-levels for varied microwave power. The detuning is swept from $\delta = -200$ kHz to $\delta = +200$ kHz in 2 ms; near 100% transfer is reliably achieved for the largest Rabi frequencies.

$\{-F, -F+1, ..., F-1, F\}$. There are no electric-dipole transitions between these states; however, the magnetic-dipole interaction $H_{\rm int} = -\boldsymbol{\mu} \cdot \mathbf{B}$ allows for Rabi couplings between them.

In the laboratory, this is done by the application of microwave and rf-fields [90, 91]. We can thus control the internal state population of the condensate by driving Rabi oscillations or performing "Landau-Zener" sweeps of the frequency around resonance.[‡] Both processes coherently alter the state of the trapped atoms, as demonstrated in Fig. 2.6. In principle, arbitrary state superpositions can be prepared, limited only by mean-field effects and systematic imperfections to lifetimes of a few ms. The splitting between levels of a single F manifold, determined by the Zeeman effect, are linear to first order in a small bias field $\mathbf{B} \sim 1$ G and are on the order of MHz. The spectral width of the applied fields can be much narrower (on the order of Hz), which allows for the isolation of transitions between hyperfine sub-levels in different manifolds and selective driving of transitions between them. Transitions within a single hyperfine manifold can be isolated by taking advantage of the quadratic Zeeman effect.

[‡]The case of off-resonant applied microwave fields, applying an ac-Stark shift (described above) has also been used to study spinor gases [101–103].

2.3 Optical lattices and band structure

An optical lattice, in its most basic realization, consists of a single laser beam that is retroreflected back onto itself to form a standing-wave interference pattern with the spatial period $d = \lambda/2$. The standing wave interference creates a series of sub-wavelength-sized optical potential wells that remain coupled through tunneling. More general lattice configurations in higher dimensions can be implemented by interfering multiple mutually coherent laser beams (not necessarily retroreflected) [16, 104]. For the work described in this thesis, we will restrict ourselves to the case of a one-dimensional lattice along the $\hat{z}$ direction

$$V(z) = V_{\text{latt}} \sin^2 (k_{\text{latt}} z) \tag{2.22}$$

where V_{latt} is the lattice depth and $k_{\text{latt}} = 2\pi/\lambda$. As discussed in any basic solid-state physics textbook [105], the dispersion relation for a free particle of mass m in one dimension $E(k) = \hbar^2 k^2/(2m)$ is modified by the lattice into periodic bands because of to the condition that solutions of the time-independent Schrödinger equation $H\psi = E\psi$ with $H = \hat{p}^2/2m + V(z)$ must share the periodicity of the lattice potential $V(z)$. These solutions are known as Bloch waves and have the general form

$$\phi_q(z) = e^{iqz} u_q(z) \tag{2.23}$$

where $u_q(z) = u_q(z + d)$, and q is known as the quasimomentum. As detailed further in e.g. [16, 87, 106], inserting ϕ_q (Eq. 2.23) into the kinetic energy term transforms the Schrödinger equation into $[(\hat{p} + q)^2/(2m) + V(z)]u_q(z) = E_q u_q(z)$. Writing both $u_q(z)$ and $V(z)$ as a Fourier series gives

$$u_q(z) = \sum_l c_l^{(q)} e^{i(lK)z} \qquad \text{and} \qquad V(z) = \sum_j V_j e^{ijKz} \tag{2.24}$$

with reciprocal lattice wave numbers $K = \pi/d$. Inserting the above into the time independent Schrödinger equation results in the eigenvalue problem

$$\sum_l \frac{(Kl + q)^2}{2m} c_l^{(q,n)} e^{ilKz} + \sum_l \sum_j c_l^{(q,n)} V_j e^{i(j+l)Kz} = E_q^{(n)} \sum_l c_l^{(q,n)} e^{i(lK)z} \tag{2.25}$$

where we have included the band index n. This is valid for an any spatially periodic potential and can be written conveniently in matrix form

$$\sum_{l,j} H_{l,j} \cdot c_l^{(q,n)} = E_q^{(n)} c_l^{(q,n)} \tag{2.26}$$

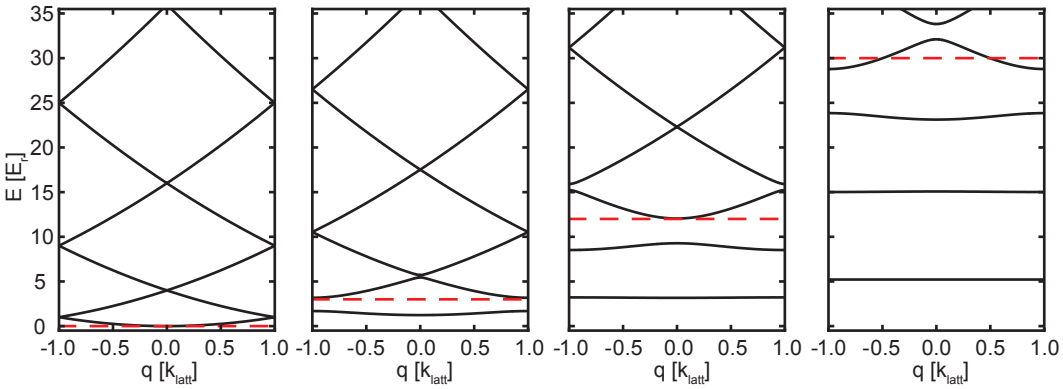

Figure 2.7: Energy bands of the sinusoidal lattice at varying depth. Plotted eigenenergies $E(q)$ for the first five bands of the lattice for $s = 0, 3, 12, 30$ (from left to right) in the first Brillouin zone. The dashed red line gives the lattice depth, indicating the number of bound states in the lattice potential.

where $H_{l,j}$ is a square matrix with diagonal elements of the form $(Kl+q)^2/2m+V_{j=0}$ and off-diagonal elements $V_{|l-j|}$. The one-dimensional optical lattice potential (Eq. 2.22) considered above has $K = 2k_{\text{latt}}$ and the Fourier decomposition $V_0 = V_{\text{latt}}/2$ and $V_1 = -V_{\text{latt}}/4$, leading to a tridiagonal $H_{l,j}$. The eigenvalues and vectors can then be found by taking a finite number of lattice wave numbers $K = [-2l_{\max}, ..., -2l_{\max}]$ and diagonalizing $H_{i,j}$. Plotted in Fig. 2.7 are the eigenenergies of Eq. 2.22 in the first Brillouin zone ($q = [-k_{\text{latt}}, +k_{\text{latt}}]$) for different lattice depths $s = V_{\text{latt}}/E_r$, where the recoil energy $E_r = \hbar\omega_R = \hbar^2 k_{\text{latt}}^2/(2m)$ is the kinetic energy of an atom of mass m recoiling from the absorption of a photon with wave number k_{latt}.

For nonzero V_{latt}, band gaps (with q and n dependent energy Δ_{gap}) are opened in the dispersion relation, leaving bands of allowed eigenstates of the potential separated by gaps with zero density of states. The energy width of a band is related to the tunneling amplitude among neighboring lattice wells.[§] Note that increasing the lattice depth flattens these bands and shifts the zero-point energy up from the free particle case. The flattening of the bands corresponds to an increase in a particle's effective mass and reduction of its kinetic energy. For very deep lattices, the deeply bound energies approach those of a harmonic oscillator with trapping frequency given by $\omega_{\text{ho}} = 2\sqrt{s}\omega_R$. In this limit, each lattice well acts as an isolated, tightly-confining harmonic trap.

The wave functions for these bands are generically given by Bloch waves

[§]In the tight-binding limit, the band width is related to the tunneling parameter by $\Delta_{\text{band}} = 4t$

described in Eq. 2.23. They are identified by a single quasimomentum q and band index n and have infinite spatial extent, thus making the Bloch basis convenient for describing the coherent states of a shallow lattice potential. For deeper lattices, it is often convenient to instead consider the Wannier functions describing a particle localized to a single lattice site [107]. One formulation for the Wannier functions is given by

$$w_n(z - z_i) \propto \sum_q e^{-iqx_i} \phi_q^{(n)}(z). \tag{2.27}$$

While the above relation provides a state localized around z_i, it is not guaranteed to provide the *maximally* localized wave function. While $w_n(z - z_i)$ converge to the harmonic oscillator eigenstates for $V_{\text{latt}} \to \infty$, using the harmonic oscillator wave functions is generally not meaningful, as the most localized Wannier functions that still span the Bloch wave basis still have significant structure beyond the typical harmonic oscillator length of a single well. In fact, even in the case of a deep lattice, the small differences between the harmonic oscillator wave functions and Wannier functions can lead to large discrepancies in calculations of the tunneling rate between wells (see Eq. 2.32). The necessary accurate calculation of the localized Wannier function can be achieved using well established methods, as described in [26, 108].¶ Several of the relevant wave functions are plotted in Fig. 2.8.

2.3.1 Single particle dynamics

The band structure of the lattice significantly modifies the dynamics of non-interacting particles in the periodic potential. If we consider a particle in the lowest band, by convention $n = 0$, of the lattice, we see that the dispersion relation is flattened and gapped. When subjected to a force F the particle's quasimomentum evolves just as in free space

$$\hbar q(t) = Ft + \hbar q(0). \tag{2.28}$$

While for a free particle, this corresponds to continuous acceleration (in the non-relativistic limit), the gapped dispersion relation of the lattice prevents such continuous acceleration as the particle is confined to move on the lowest band of the lattice. This leads to so-called Bloch oscillations, as the particle traverses the Brillouin zone and is Bragg reflected from $+k_{\text{latt}}$ to $-k_{\text{latt}}$ each time it reaches the zone edge. By analogy with optics and the free particle

¶These methods may yield a different set of phase prefactors than in Eq. 2.27 and typically rely on minimizing the total spread of the wave function $\langle z^2 \rangle - \langle z \rangle^2$.

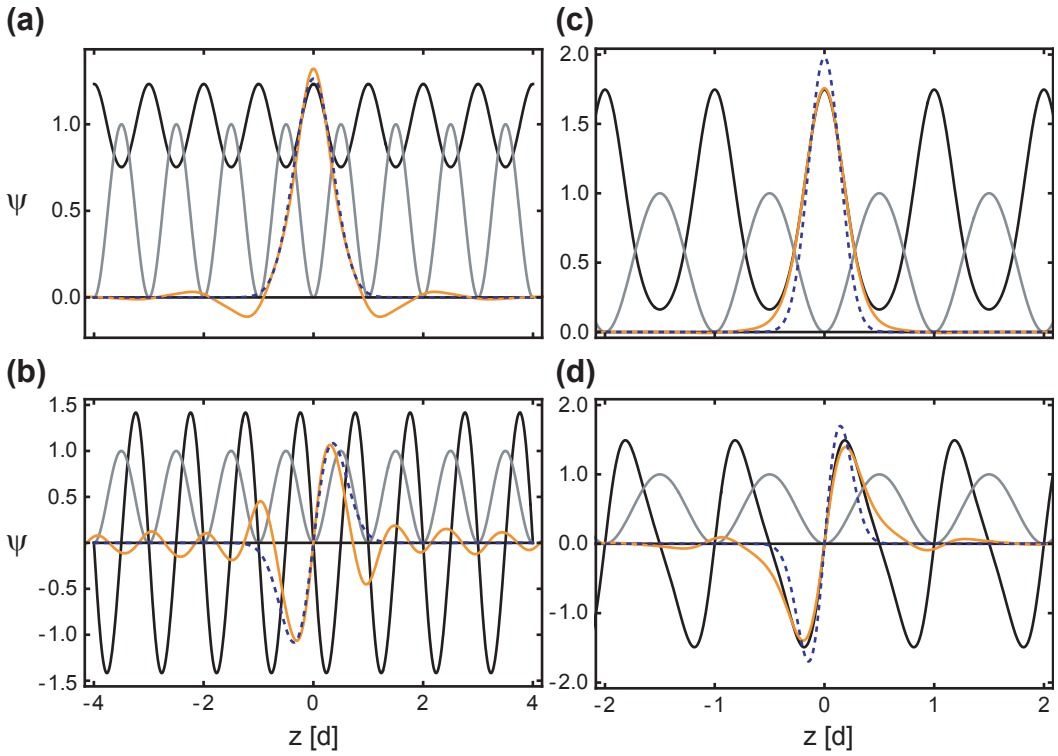

Figure 2.8: Bloch wave and Wannier functions of a sinusoidal potential. Plotted are the lattice potential, the corresponding Bloch wave, Wannier function and harmonic oscillator wave function (gray, black, orange and dashed blue respectively).(a) For s=2, n=0. (b) For s=2, n=1. (c) For s=12, n=0.(d) For s=12, n=1.

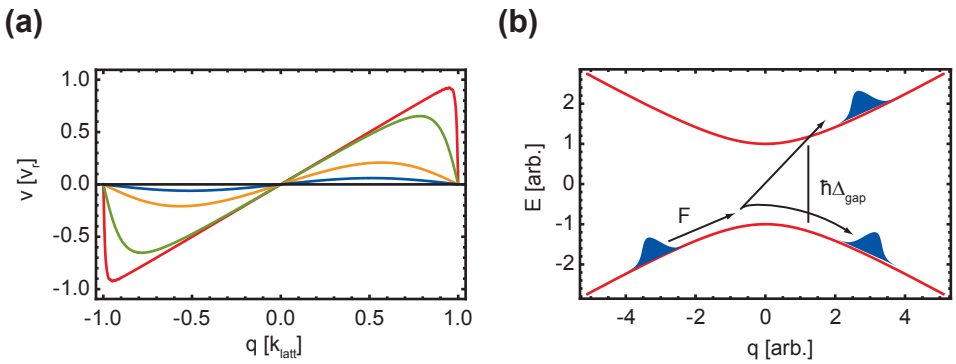

Figure 2.9: Band group velocity and Landau-Zener process in a lattice. (a) Group velocity of a particle moving in the lowest band of the lattice for $s = 0.1, 1, 5, 10$, $s \to \infty$ (red, gree, orange, blue, black). (b) Schematic Landau-Zener process at a gap, for a wave packet evolving under some force F.

case, the group velocity of particle moving in the lattice is given by [105]

$$v_g(q(t)) = \frac{1}{\hbar}\frac{dE^{(n)}(q)}{dq}\bigg|_{q(t)}. \tag{2.29}$$

Bloch oscillations can thus be seen as an oscillation of the mean momentum $\langle \hat{p} \rangle = m v_g$, c.f. Fig. 2.9a.

Bloch oscillations describe the dynamics of a particle as long as it is confined to a given band of the lattice. This is not always true and when $Fd \approx \Delta_{\text{gap}}$, there is a meaningful probability for the particle to leave the band in which it originates. This mechanism underlies Zener breakdown of a non-conducting material, and as Δ_{gap} becomes smaller as the band index increases, this typically leads to rapid population of higher bands, and thus conduction [109]. Near a gap or avoided crossing, the probability to remain in the lowest band of the lattice is described by the Landau-Zener formalism, c.f. Fig. 2.9b, which is closely related to that of adiabatic rapid passage. The rate of transfer into the higher band is given simply by [110]

$$P = 1 - \exp\left(-2\pi \frac{\Omega^2}{\hbar(dE/dt)} \right) \tag{2.30}$$

where $\hbar\Omega \approx \Delta_{\text{gap}}$ is the coupling between bands of the lattice (e.g. the matrix element coupling different bare plane wave states) and $dE/dt \propto F$ describes the slew rate through the avoided crossing.

2.3.2 Effects of weak interactions

In the noninteracting or ideal gas regime, the dynamics of a condensate in a lattice is described well by the single particle physics described above [10] such that Bloch oscillations and Landau-Zener tunneling can be observed and compared to the simple band structure theory [9, 111]. Mean-field interactions tend to alter the properties and dynamics of a lattice-trapped condensate. For sufficiently shallow lattices and weak interactions, the interactions act as an effective potential term that reduces the lattice depth by a factor $(1 + \mu/(2E_r))^{-1}$ [112]. As demonstrated in [9], dynamical effects such as Landau-Zener tunneling then behave indeed as if an effectively shallower lattice were present in this regime.

Some of these dynamical effects can be described microscopically. Taking the case of Landau-Zener tunneling, the effective reduction in lattice depth results from a breakdown of adiabaticity at a band gap caused by the nonlinearity [113]. In the presence of strong interactions, the energy spectrum at the gap can be dramatically modified (see Chapter 3 for details). The bands become multivalued near the gap and loops (or swallowtails) form in the energy spectrum. These loops prevent adiabatic following of the energy levels that would be described by Eq. 2.28, resulting in increased tunneling into higher bands as the gap is traversed.

Interactions also affect the stability of an interacting condensate trapped in a lattice. It can be shown that states near the zone edge are unstable due to interactions [114]. To understand this, consider the dispersion relation in the lowest band near the zone edge. For $q \approx \pi/d$, E_q takes on a negative curvature which corresponds to an effective mass $m^* < 0$ [105]. The negative effective mass implies a change in sign of the interaction parameter g in the GPE, leading to exponential growth of Bogoliubov perturbations $\delta\psi$ to the condensate wave function ψ, instead of the usual oscillating sound solutions. As a result, small perturbations lead to rapid decay of ψ. This so-called dynamical instability has been observed experimentally as a depletion of the condensate wave function [115].

For deeper lattices, the interaction energy can become the largest relevant energy in the system. Consequences for the strongly interacting lattice gas will be briefly discussed below.

2.3.3 Tight-binding and strong interactions

When the lattice is sufficiently deep that the lowest bands can be considered dispersion-free, it is typically more useful to consider the tight binding limit.

Here, the single particle dynamics are determined by the Hamiltonian

$$H = -t \sum_j |j+1\rangle\langle j| + h.c. \tag{2.31}$$

where j is the lattice cite index and t is the energy associated with hopping or tunneling between neighboring sites. The hopping parameter t is given by the matrix element

$$t = t^{(n)} = \int \mathrm{d}z w^{(n)*}(z) \left(\frac{\hat{p}^2}{2m} + V(z) \right) w^{(n)}(z+d) \tag{2.32}$$

and is generically band dependent; for the lowest band t is positive and thus favors delocalization in the lattice.

In the presence of interactions, the system of ultracold atoms restricted to the ground band of a lattice can be mapped onto the Bose-Hubbard model [116], a paradigmatic generalization of Eq. 2.31 [55]:

$$H = -t \sum_{\langle i,j \rangle} (\hat{b}_i^\dagger \hat{b}_j + h.c) + \frac{U}{2} \sum_i \hat{n}_i(\hat{n}_i - 1) - \mu \sum_i \hat{n}_i \tag{2.33}$$

Here the brackets indicate a summation over nearest neighbors, $\hat{b}_i^\dagger$ is the bosonic creation operator at lattice site i, $\hat{n}_i = \hat{b}_i^\dagger \hat{b}_i$ is the number operator and U represents the on-site interaction energy defined as,

$$U = g \int \mathrm{d}z |w(z)|^4. \tag{2.34}$$

Restriction to the ground band allows us to take $t > 0$ and include the negative tunneling energy explicitly. The Bose-Hubbard model contains rich physics including a quantum phase transition between a superfluid and (gapped) Mott insulator driven by the relative strength of the interactions U. Early realizations of the Bose-Hubbard model have demonstrated ultracold atom experiments to be ideal for controlled studies of the relatively simple physics it contains [14]; such experiments have more recently paved the way for the simulation of more complex Hamiltonians [27, 32, 37, 49, 117].

2.3.4 Lattice loading and characterization

In our experiments, the atoms are often loaded into the lattice by beginning with a condensed atomic cloud and introducing the optical lattice potential at a later time. In doing so, we attempt to remain in the ground state of the system

by applying an adiabatic lattice ramp, which must be slow compared to any collective excitations of the superfluid cloud, slow compared to timescales set by the gaps in the band structure [118], and slow with respect to the tunneling rate. The latter requirement assures the atomic density is allowed to rearrange in the trap plus lattice potential. While there is debate over the existence of an ideally adiabatic ramp [119–122], we can achieve sufficiently adiabatic loading of the lattice by keeping the rate of change in V_{latt} slow compared to the overall trapping frequencies and also the instantaneous tunneling time.

When considering deeper lattices where tunneling rates can be on the order of a few Hz, it becomes difficult to satisfy the adiabatic condition. We can check the ramp adiabaticity by entering the Mott insulator regime with a lattice ramp-up and then returning back to superfluid with a lattice ramp-down. For short hold times and filling fractions of order one, we can attribute any heating seen in the final condensate to nonadiabatic processes in the lattice ramp procedure [123].

Once the atoms are loaded into the lattice, several techniques can be used to characterize the lattice depth. A simple and fast technique takes advantage of matter wave diffraction following the application of a pulsed optical potential. This form of Kapitza-Dirac diffraction allows us to measure the lattice depth by looking at the time evolution of diffracted momentum modes during the short lattice pulse. This procedure was previously characterized in [87, 124]. In Fig. 2.10 we show the time of flight momentum distributions after a short lattice pulse along with the corresponding lattice depth calculated by fitting the distributions to calculated diffraction patterns given by the set of equations

$$i\dot{c}_j = \frac{E_r^{(2)} j^2}{\hbar} c_j + \frac{V_{\mathrm{latt}}}{4\hbar}(c_{j-1} + 2c_j + c_{j+1}) \tag{2.35}$$

describing the evolution of the amplitudes for each diffracted mode c_j for integer j, where we define the general $n-$photon recoil energy $E_r^{(n)} = n^2 E_r$.

Other methods include lattice modulation spectroscopy, which we shall touch on in Chapter 5. To briefly introduce the principle, this method relies on measuring Δ_{gap} by modulating the phase or amplitude of the lattice in time. This allows for the excitation of higher bands in the lattice, inferred by a reduced superfluid visibility or measured directly via a band-map to adiabatically transform the Bloch states onto free particle states [12].

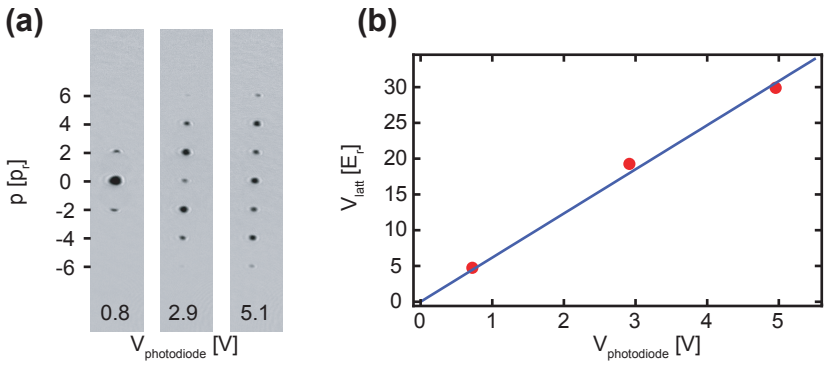

Figure 2.10: (a) Time of flight Kapitza-Dirac diffraction patterns after short lattice pulses ($\tau = 10\mu$s) of variable intensity. (b) Fitted lattice depth as a function of a pick-off photodiode voltage monitoring the power in the lattice beam. The potential depth is found from the TOF images in (a) by comparison with solutions to Eq. 2.35. For details see [87, 124].

Chapter 3

Superfluid Bloch Dynamics in a Tilted Incommensurate Lattice

In this chapter, we investigate the interplay of disorder and interactions in the accelerated transport of a lattice-trapped Bose-Einstein condensate through an incommensurate optical lattice. While there often is a focus on the cleanliness of and the ease of control in optical lattice systems, the properties of real materials critically depend on the presence of "imperfections" such as impurities and lattice defects. Understanding the behavior of *interacting* disordered systems continues to present a challenge to condensed matter theory and experiment alike. By examining the interplay of interactions and disorder in the dynamics of Bloch oscillations in an optical lattice, we demonstrate that weak interactions can effectively cancel the damping of Bloch oscillations induced by disorder due to screening, and we provide a simple model to qualitatively capture this effect. The competition between disorder and weak interactions described in this work complements the cooperation between disorder and strong interactions observed in an earlier experiment on the Bose-glass phase [54].

The following chapter is based on the article *Superfluid Bloch Dynamics in an Incommensurate Lattice*, New Journal of Physics **16**, 065011 (2014) [125].

3.1 Interacting disordered systems

The combined effects of disorder and interactions in condensed-matter systems can influence their transport properties in profound ways. Beyond merely reducing conductivity, disorder can lead to Anderson localization [57] in the absence of interactions, and repulsive interactions can give rise to localized Mott phases [126] without the influence of disorder. While disorder and interaction

act cooperatively in the limit of strong interactions by promoting disordered insulating phases [55, 60], weak interactions in bosonic systems can counteract the localizing effects of disorder by making accessible higher-energy states, thus screening the disorder potential [61, 62]. The often subtle interplay between disorder and interactions is relevant for condensed-matter systems such as superfluid helium in porous media and disordered films [69, 127] and granular superconductors [68, 128], but it can also be studied experimentally with ultracold atoms in optical lattices. While optical lattices are naturally defect free [16], it is possible to implement disorder using laser speckle [47, 58], localized impurity atoms [54], and incommensurate standing waves [129]. Recent experiments with disordered optical potentials have addressed Anderson localization [47, 51, 58], delocalization due to repulsive interactions [50, 62, 130], as well as the formation of glassy, localized phases in the regime of strong repulsive interactions [48, 49, 54, 56, 131]. It has also been proposed that disordered many-body systems may experience a novel form of localization known as many-body localization [132, 133], ultracold atoms have already begun to study these effects [52, 130].

3.2 Bloch oscillation basics

Disorder and interactions also fundamentally affect the dynamics of particles in lattice potentials. Here, we examine the case of static external forcing resulting in coherent Bloch oscillations (BOs) [109, 134] that prevent macroscopic transport unless mechanisms for relaxation exist [135]. While BOs are overdamped in conventional solids due to relaxation times much shorter than an oscillation period, they can be observed in superlattice semiconductors [136] and also with ultracold atoms in optical lattices [4, 10, 137]. Atomic quantum gases in optical lattices naturally provide an environment free of scatterers such as defects and lattice-phonons and allow, in principle, for long lived oscillations, c.f. Fig. 3.1a.

In the atomic system, minimizing the collisional interactions is necessary for the direct observation of extremely long-lived BOs [67, 138, 139]. Typical mean-field interactions in Bose-Einstein condensates already result in significant dephasing, c.f. Fig. 3.1b [67, 139] due to nonlinearities, dynamical instability, and quantum chaotic dynamics [140–142]. (It has recently been observed that in certain parameter regimes, such dephasing can be reversible [143, 144].) A qualitatively similar dephasing of BOs in optical lattices was also observed to occur due to the additional presence of disorder, which scrambles the regular phase evolution between lattice sites [66]. In addition to dephasing, the damping of BOs by disorder was also accompanied by strong depletion of

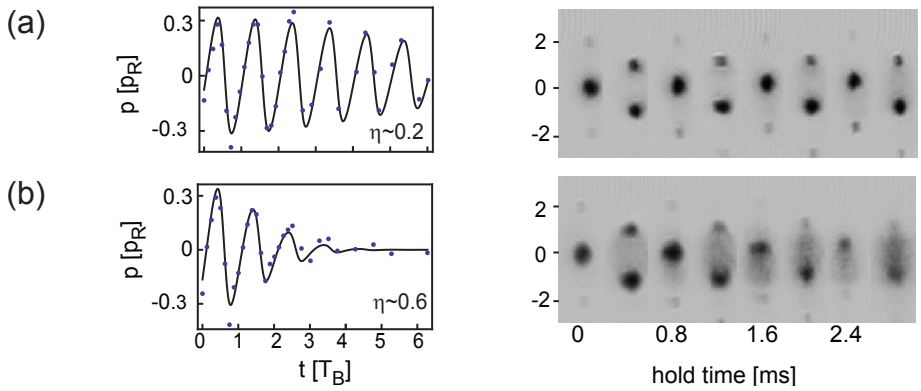

Figure 3.1: Bloch oscillations of an optically trapped atomic cloud. (a) Observed oscillations of the atomic momentum distribution and mean momentum $\langle \hat{p} \rangle$ for a dilute ultracold atomic gas with mean field $\mu \sim 0.1E_r$ in a ~ 20 Hz trap. The damping rate is fit to be $\eta \sim 0.2T_B$. (b) Same for increased mean field $\mu \sim 0.3E_r$. The damping rate is increased to $\eta \sim 0.6T_B$, and a significant spreading of the momentum wave packet can be see in time of flight images. Lines are the result a fit described in the text and points represent the center of mass of the expanded atomic cloud.

the condensate wave function.

For the case that both interactions and disorder are present, it has been predicted that the combined effects can modify the BO dynamics, by either reducing or enhancing the damping due to disorder, depending on their relative magnitude [145, 146]. In the experiment described here, the interplay between disorder and interactions is studied in the dynamics of Bloch oscillations in an incommensurate lattice. The results demonstrate that for a given disorder-induced damping rate, increased interactions can reduce or enhance the overall damping rate. Furthermore, we identify a characteristic interaction strength between the regimes of reduction and enhancement, corresponding to a typical disorder energy scale. A simple model to capture the basic features of the system is proposed and discussed.

3.3 Quasiperiodic potential

For this experiment we choose to implement disorder through the use of a bichromatic lattice potential consisting of two collinear superimposed optical standing waves of different wavelengths λ_1 and λ_2. For rational wavelength ratios, such lattices describe super-lattices or can be used to generate a lattice with a basis of lattice wells at each site. We will consider here the case that the

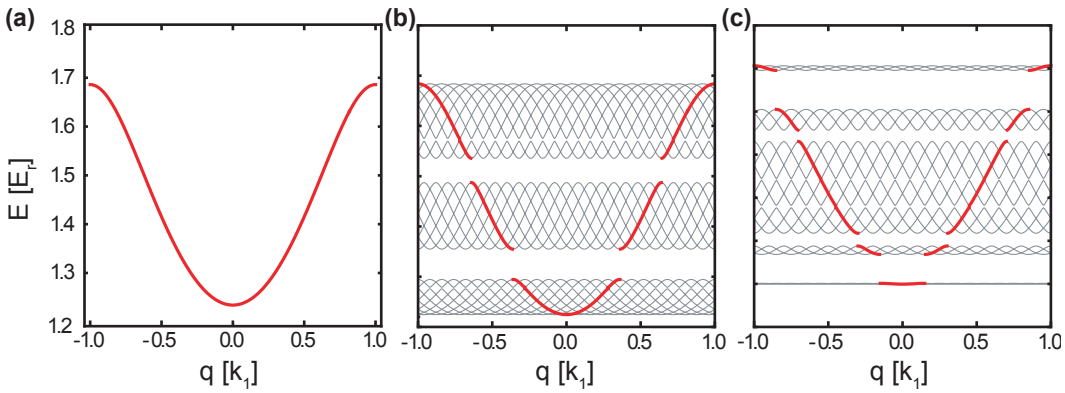

Figure 3.2: Band structure of the quasiperiodic lattice. The red lines represent the lowest ($n = 0$) band of the main lattice, while the gray lines represent all minibands of the total superlattice. The longer periodicity of the bichromatic lattice results in a shrinking of the first Brillouin zone. (a) The unperturbed $n = 0$ band of an $s_1 = 3$ lattice. (b) The lowest set of minibands corresponding to the original unperturbed band in (a) for a quasiperiodic lattice with $\beta = 1.36$ for $s_1 = 3$ and $s_2 = 0.5/\beta^2$. (c) Same as (b) for $\beta = 1.15$.

wavelengths are incommensurate, i.e. have a ratio that cannot be expressed as m/n, where m and n are integers. Such a lattice forms an optical quasicrystal [147] that lacks crystalline translational symmetry, but still maintains order on a shorter length scale [148]. For a quasiperiodic potential generated by the overlap of two incommensurate standing waves, we can approximate the irrational wavelength ratio through a rational number, due to the finite precision with which the laser wavelengths are known. In this case, the superposition leads to a superlattice with long-range translational symmetry, rather than a true quasicrystal. However, as we will see, this is of no practical consequence as long as the period of the superlattice exceeds the size of the atomic cloud. In our experiments, we generate quasiperiodic potentials with $\lambda_1 = 1064$ nm and $\lambda_2 = 785$ nm; the *commensurate* ratio $\beta \equiv \lambda_1/\lambda_2 \approx 1.36$ can be used to describe the band structure.

The bichromatic lattice has long range periodicity Λ such that $V(z) = V(z + \Lambda)$. Assuming a nearly rational β, we find its true period to be given by the ratio

$$\beta = \frac{m}{n} \qquad \text{such that} \qquad \frac{\Lambda}{\lambda_1} = n \qquad \text{and} \qquad \frac{\Lambda}{\lambda_2} = m \tag{3.1}$$

requiring that m/n be written with the smallest possible integers (in reduced terms). Taking $\beta = 1.36$, we find $n = 25$ and $m = 34$. Thus for a potential of

the form

$$V(z) = s_1 E_{r,1} \sin^2 k_1 z + s_2 E_{r,2} \sin^2 k_2 z \tag{3.2}$$

we can use Eq. 2.26 to solve for the band structure of the total quasiperiodic potential if we select $K = 2\pi/\Lambda$. In our example, $H_{i,j}$ has diagonal terms $(Kl + q)^2/2m + s_1 E_{r,1}/2 + s_2 E_{r,2}/2$ and off-diagonal elements $H_{|l-j|=25} = -s_1 E_{r,1}/4$ and $H_{|l-j|=34} = -s_2 E_{r,2}/4$. The leading effect of a weak secondary lattice on the band structure is to break up the unperturbed band in Fig. 3.2a into a series of gapped mini bands in Fig. 3.2b. These gaps are narrow in energy compared with $s_2 E_{r,2}$ due to the second order nature of the process which opens the minigaps.

Quasiperiodicity as Disorder

Optical lattice experiments have been able to implement disordered and quasidisordered systems in several ways. Most common among these are the introduction of optical speckle potentials [47, 48, 129, 149], localized atomic impurities [53, 54, 150], or the bichromatic optical lattices discussed here [50, 51, 54, 62, 151]. We can get an idea of the physics of the bichromatic potential by examining the Harper or Aubry-André model for particles hopping on a quasiperiodic lattice with amplitude disorder [152, 153]

$$H = -t \sum_j (|j\rangle\langle j+1| + |j+1\rangle\langle j|) + \Delta \sum_j \cos(2\pi\beta j)|j\rangle\langle j|. \tag{3.3}$$

A system of noninteracting particles in the tight binding limit of a one-dimensional quasiperiodic potential maps onto this model with [154, 155]

$$t \approx 1.43 s_1^{0.98} e^{-2.07\sqrt{s_1}} \qquad \text{and} \qquad \Delta \approx \frac{s_2 \beta^2}{2}. \tag{3.4}$$

The Aubry-André model shows an Anderson-like transition from extended to exponentially-localized states for $\Delta/t = 2$. Unlike Anderson localization, which occurs for all states and any nonzero amount of disorder (in one dimension), the Aubry-André model exhibits a finite mobility edge E_{mob} for sufficiently small Δ. States with energy larger than E_{mob} are delocalized, while the lowest-lying states experience Anderson-like localization. While this holds for the infinite system with truly irrational β, for rational β the concept of the degree of incommensurability (measured by the ratio of the system size L and the superlattice period Λ) must be considered [155]. For $\Lambda/L \lesssim 1$, the true periodicity of the lattice is not sampled by the system and we can consider the model to be a good approximation for a disordered system. In

this limit, an effectively disordered energy landscape with no long range order is seen by the atoms. The relative ease of implementation and the fact that the essential physics can be captured in the easily calculated spectrum of the potential make the incommensurate bichromatic lattice an attractive system in which to study (quasi-*)disorder.

3.4 Experiment

In our experiment we load a BEC of a few 10^4 ^{87}Rb atoms in the $|F, m_F\rangle \equiv |2, -2\rangle$ hyperfine state into a crossed optical dipole trap (XODT) [89]. A magnetic field gradient levitates the BEC in the trap, before a one-dimensional optical lattice

$$V(z) = s_1 E_r \cos^2(k_1 z) + s_2 E_r \cos^2(k_2 z) \tag{3.5}$$

is adiabatically ramped up along the vertical direction $\hat{z}$. Here $k_j = 2\pi/\lambda_j$, and s_1 (s_2) are the lattice depths in units of the main lattice recoil energy $E_r = (\hbar k_1)^2/(2m)$, $\hbar = h/(2\pi)$ is Planck's reduced constant and $\lambda_1 = 1064$ nm and $\lambda_2 = 785.2$ nm are the wavelengths of the lattice. The ratio $\beta = k_2/k_1 \approx 1.3551$ is used as a measure of the lattice commensurability; for nearly irrational β, the lattices will be periodic on length scales exceeding those relevant to the experiment. Although this true periodicity exceeds the system size, it should be noted that the bichromatic potential has a quasiperiod $d/(\beta - 1) \sim 2.8d$, with $d = \lambda_1/2$ the main lattice spacing. The quasiperiod describes the length scale on which the potential approximately repeats itself and is much shorter than the real period Λ. As our system spans only a few of these quasiperiods and less than a single Λ, for relevant time and length scales the bichromatic potential can be considered a good approximation for disorder. The main lattice has a depth of $s_1 = 3$ for all measurements and the second lattice depth is varied from $s_2 = 0$ to $s_2 \approx 1$. We define the disorder strength Δ as the average energy shift of a lattice site due to the secondary lattice, $\Delta \approx s_2/2$, which also corresponds to the energy scale $E_{\text{gap}} \approx s_2/2E_r$ of perturbations to the band structure.

The chemical potential of the condensate is adjusted in a range $\tilde{\mu} = \mu/E_r = 0.1...0.5$ prior to loading the lattice by varying the atom number as well as the trapping frequency of the XODT from $\sim$ 17 Hz to $\sim$ 80 Hz, corresponding to condensates with radii from $\sim 8d$ to $\sim 12d$. To induce BOs the levitating

*In previous work [54], we did not observe a shift in the transition to an insulating state as a function of U/t, for the case of an incommensurate lattice. On the other hand, a shift in the superfluid-insulator transition is seen for random atomic disorder. The different behavior in each case can be related back to the fact that disorder correlations do not decay over short ranges for the incommensurate lattice, unlike in the case of atomic disorder.

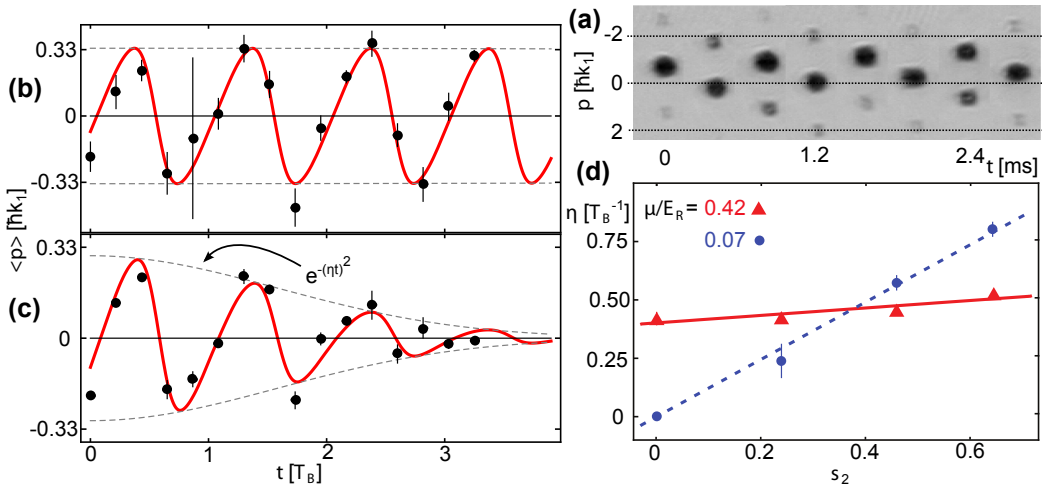

Figure 3.3: Bloch oscillations of weakly interacting atoms in an optical lattice. (a) Absorption images for different evolution times in a single-wavelength lattice. (b,c) Observed average momentum for a weakly interacting cloud ($\tilde{\mu} = 0.07$) for $s_2 = 0$ and 0.46 respectively. The red lines are fits to the data while the dashed gray lines trace the Gaussian envelope with decay rate η. The extracted damping rates in b) and c) are 0.02 ${T_B}^{-1}$ and 0.55 ${T_B}^{-1}$ respectively. (d) Damping rate as a function of secondary lattice depth for $\tilde{\mu} = 0.07$ (blue, dashed, circles) and for $\tilde{\mu} = 0.42$ (red, solid, triangles). The lines are linear fits to guide the eye. In (b-d), each data point represents three repetitions of the experiment, error bars represent standard deviations.

gradient is rapidly switched off in < 200 μs, and the atoms are allowed to evolve in the lattice plus XODT potentials for a variable hold time. During this time, the atoms undergo BOs with period $T_B = h/Fd \approx 0.9$ ms where $F = mg$ is the gravitational force; for our system $Fd = 0.56$ E_r. The atoms are then suddenly released and the atomic momentum distribution is imaged on a CCD camera after 18 ms time of flight, as shown in Fig. 3.3a.

After repeating the experiment for different hold times, the oscillations are recorded as seen in Fig. 3.3b,c. A damping rate η is extracted from the data by fitting the mean of the linear momentum with

$$\langle p_z(t) \rangle = e^{-(\eta t)^2} \frac{dE(q)}{dq}. \tag{3.6}$$

Here $E(q)$ is the energy dispersion of the lowest energy band of the lattice as a function of quasimomentum q which evolves as $\hbar q = Ft$. The Gaussian envelope is chosen because at short times the $p_z(t) \approx (1 - t^2)$ behavior best matches

dephasing due to two beating frequencies [146]. This also matches previously observed and simulated BO damping behavior due to both interactions and incommensurate lattices [144, 146], while a pure exponential envelope has been suggested in the disorder-free case [142].

In the weakly interacting ($\tilde{\mu} = 0.07$) and disorder-free case (Fig. 3.3b) we observe only weakly damped oscillations, with damping due to the nonzero interaction energy and the harmonic confinement of the XODT. When adding the second lattice with $s_2 = 0.46$ the damping time is markedly reduced to just a few T_B, as seen in Fig. 3.3c. As illustrated in Fig. 3.3d, increasing the secondary lattice depth increases the damping rate for a weakly interacting cloud; however, as shown for two interactions $\tilde{\mu} = 0.07$ and 0.42, the effect of the disorder is weaker when stronger interactions are present. Furthermore, the effect of interactions depends on the depth of the disorder potential: for small $s_2 < 0.35$, the damping rate is higher for low $\tilde{\mu}$ while the opposite is true for $s_2 > 0.35$.

3.5 Microscopic model of damping

To better understand the impact of interactions in the disordered lattice, we investigate the damping in the noninteracting and interacting regimes separately. In the noninteracting case, damping can be described by considering the single particle band structure of the lattice potential. Starting with all the atoms at $q = 0$ in the lowest band, for $s_2 = 0$ the atoms experience a continuous, periodic dispersion relation $E(q)$ giving rise to long-lived Bloch oscillations described by Eq. 3.6. The chief effect of the second lattice, seen in Fig. 3.4a, is to open minigaps of energy Δ_{gap} in the band structure at k_2 and $|k_1 - k_2|$ [151]. The minigaps serve to disrupt the evolution of the momentum distribution by splitting the condensate among the minibands of the lattice as described by Landau-Zener tunneling [109], as illustrated in Fig. 3.4b. The minigaps appear at values of q that are irrational fractions of the original Brillouin zone width $2\hbar k_1$. As a result of the incommensurability, the estimated rephasing time for a single particle is much longer than the oscillation lifetime in our experiment.

The fraction of atoms which tunnel to those that pass the minigap adiabatically is given approximately, in the Landau-Zener formalism, by

$$P = \exp\left[\frac{-2\pi\Delta_{\mathrm{gap}}^2}{F(\mathrm{d}E/\mathrm{d}q|_{\mathrm{gap}})}\right]. \tag{3.7}$$

where $\mathrm{d}E/\mathrm{d}q|_{\mathrm{gap}}$ is the slope of the unperturbed band at the gap. In absorption

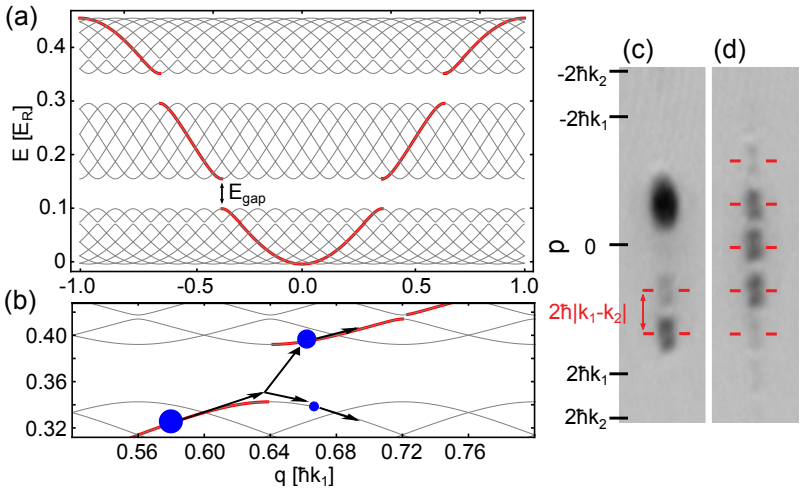

Figure 3.4: Damping due to the band structure of the bichromatic lattice. (a) Band structure of the lowest energy band of the two-color lattice calculated in the tight-binding limit for $s_1 = 3$ and $s_2 = 0.1$. Our irrational $\beta = \lambda_1/\lambda_2$ is approximated by $\beta = 1.36$, which is still nonperiodic on experimental length scales. The bold red curve outlines the perturbed lowest band of the $s_2 = 0$ lattice while the gray lines represent minibands of the bichromatic potential. The primary effect of the second lattice is to open minigaps in the lowest band. (b) Schematic illustration of a Landau-Zener tunneling event at a mini gap. (c,d) Momentum distributions of atoms undergoing oscillations in a band structure described in a) after 0.65 T_B and 2.4 T_B respectively. The red lines represent a relative momentum of $2\hbar|k_1 - k_2|$.

images of the momentum distribution, the splitting among mini-bands of the first Brillouin zone is clearly seen after evolving for just $T_B/4$ (i.e. passing through just one half of the Brillouin zone), Fig. 3.4c. Unlike in Fig. 3.3a, where a single color lattice gives peaks separated by $2\hbar k_1$, we observe an extra peak at a momentum separation of $2\hbar|k_1 - k_2|$. For longer evolution times as in Fig. 3.4d, the condensate breaks up into a series of peaks with spacing $2\hbar|k_1 - k_2|$, spanning a range of momenta between $\pm 2\hbar k_1$ consisting of the first Brillouin zone. This spreading of the momentum wave packet leads to a breakdown of collective oscillation and accelerated damping as described in Fig. 3.3c.

To demonstrate the BO damping effect of the bichromatic lattice, we numerically propagate a wave packet through the bichromatic dispersion relation. For simplicity, the calculation does not include coherent effects involved when the wave packet crosses a minigap, resulting in a purely probabilistic treatment of the Landau-Zener process. At times when a wave packet reaches a minigap,

it is instantaneously split according to the adiabatic crossing probability given by Eq. 3.7. The resulting calculation reproduces the damped BO behavior seen in the experiment and demonstrates spreading of the momentum wave packet in discrete peaks.

Mean-field interactions in the BEC modify the damping by changing the miniband shape near the minigap, causing the minibands to develop a swallow-tail structure [114]. The multivalued (multivalued) energy spectrum can be calculated from a simple model [113]

$$H_{\mathrm{NLZ}} = \begin{pmatrix} \frac{\Delta E(t)}{2} + \frac{cE_r}{2}(|u|^2 - |v|^2) & \frac{\Delta_{\mathrm{gap}}}{2} \\ \frac{\Delta_{\mathrm{gap}}}{2} & -\frac{\Delta E(t)}{2} - \frac{cE_r}{2}(|u|^2 - |v|^2) \end{pmatrix}, \tag{3.8}$$

where $\Delta E(t)$ gives the energy splitting between upper and lower branches of the avoided crossing for an atom moving in the band structure as a function of time, $c = \mu/4E_r$ parameterizes an interaction induced detuning, and $|u|^2$ and $|v|^2$ are the populations in the upper and lower branches respectively. The eigenvalues of this system are shown in Fig. 3.5a for $cE_r \sim \Delta_{\mathrm{gap}}$. The shape of the avoided crossing is effectively changed, with the lower band narrowing near the avoided crossing and becoming multivalued. This change leads to the breakdown of adiabaticity in the strong-interaction limit $\mu \gtrsim \Delta_{\mathrm{gap}}$, resulting in an expected increase in the fraction P of atoms that tunnel through the gap and remain on the perturbed original band.

The probability to tunnel from one band to the next can be calculated from the time evolution of H_{NLZ}. Indeed, the nonadiabatic transition rate increases with increased μ. Including these modified tunneling rates in our numerical calculation allows us to estimate the contribution of the nonlinear Landau-Zener process to the damping rates. The tunneling results for the modified gap, shown for $s_2 = 0.4$ in Fig. 3.5b, predict a reduction of the damping rate as the interactions are increased. Our numerical calculation effectively treats the nonlinearities as rescaling the gap size in Eq. 3.7, according to the interaction energy. The effective Δ_{gap} is as much as 50% smaller for $\mu \approx \Delta_{\mathrm{gap}}$, predicting as much as a 1/3 reduction of the damping rate.

We note that this simple calculation does not separately address the damping induced by the interactions themselves, which perturb the evenly-spaced Wannier-Stark energy levels of the tilted(forced)-lattice, and give rise to irreversible damping for our lattice parameters in which the energy offset between lattice sites is comparable to the tunneling matrix element [142, 144].

The predicted decrease of the minigap-induced damping due to interactions in Fig. 3.5b agrees with our experimental data to within a factor of 3. The discrepancy could result from a number of factors. For example, our calculation

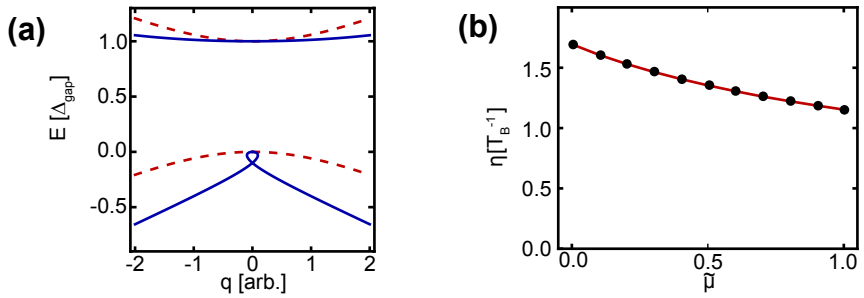

Figure 3.5: Effect of nonlinearities on the structure of the minigaps. (a) Dashed red lines describe the unperturbed energy bands in the vicinity of a minigap, while the solid blue lines describe the band shape for the case of $\mu \sim \Delta_{\rm gap}$. Note the "sharpening" or narrowing of the lower band and the appearance of a loop at the quasimomentum corresponding to the exact avoided crossing. The damping rate due to the minigaps for s_2=0.4 is plotted in (b) for a range of $\tilde{\mu}$ as calculated using a nonlinear Landau-Zener formalism (see text)

does not take into account the three dimensional nature of the experimental setup nor does it include coherent effects involved in the (non)adiabatic crossing of a minigap, which were excluded to minimize computational time and complexity for propagation in the quasiperiodic potential. The assumption that the tunneling through a minigap happens exactly at the gap is also unrealistic as the momentum width of the condensate is comparable to the quasimomentum spacing between the gaps and one would expect coherent dynamics beyond the probabilistic, isolated gap treatment used here to alter the details of the dynamics, but not the qualitative effect observed.

Experimentally, we have selected our parameters to best probe the relationship between interaction-induced damping and Landau-Zener damping due to the potential's quasi-disorder. Fig. 3.6a plots the measured damping rate with varied chemical potential for different disorder depths, as described in Fig. 3.3b,c. In the $s_2 = 0$ case we observe, as expected from earlier related work [67], a steady increase in the interaction-induced damping. For $s_2 > 0$, the initial damping in the weakly interacting case is significantly enhanced. However, for increasing interactions, within an experimentally accessible range, we subsequently observe a *decrease* in the damping rate, only to be followed later by a small increase. A heuristic parabolic fit yields a chemical potential $\tilde{\mu}_{co} = 0.29$ for minimum damping.

The observed behavior is consistent with a simple, qualitative picture in which the interactions initially screen out the disorder, thus allowing for longer lived oscillations. Above $\tilde{\mu}_{co}$, the damping driven by interactions out-

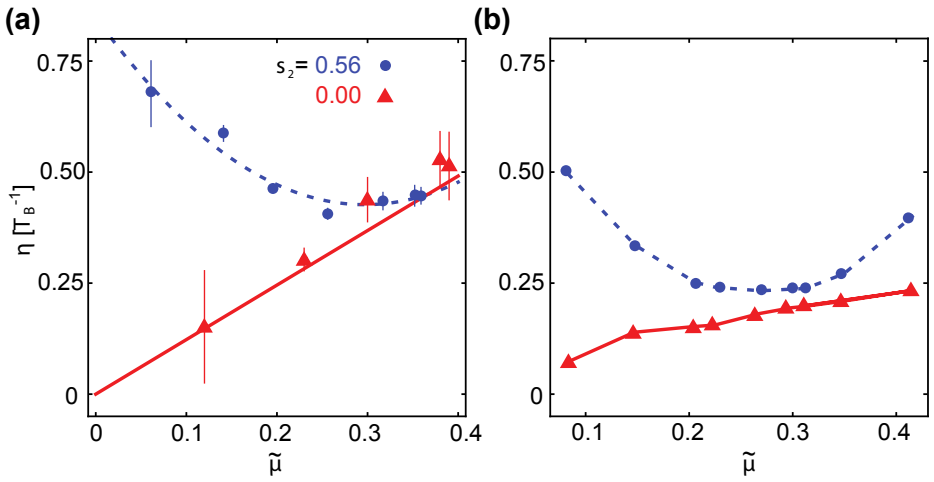

Figure 3.6: Damping rates of BOs as a function of chemical potential. (a) Measured damping rate as a function of $\tilde{\mu}$ for different s_2. For the $s_2 = 0$ case (red, solid, triangles), the damping rate increases roughly linearly with $\tilde{\mu}$. For a larger disorder $s_2 = 0.56$ (blue, dashed, circles) a clear decrease in the damping rate is observed as the $\tilde{\mu}$ is increased. Lines are fits to guide the eye. From a parabolic fit to the $s_2 = 0.56$ data a minimum at $\tilde{\mu}_c = 0.29$ is obtained. In b) we plot the same data obtained from a 3DGPE simulation. A fit finds a minimum damping rate at $\tilde{\mu}_c = 0.26$.

weighs the screening and the damping rate begins to increase. We note that $\tilde{\mu}_{co} \approx \Delta = 0.28$, indicating that the crossover from disorder-dominated to mean-field-dominated behavior occurs when the interacton strength becomes comparable to the disorder. This is consistent with findings for the equilibrium case [62], where a weakly-interacting condensate with $\tilde{\mu} < \Delta$ tends to become fragmented, corresponding to a breakdown of global coherence across the cloud, and where the fragmentation becomes less severe leading to increased phase coherence as the potential is "filled" by the interaction energy. Above $\tilde{\mu}_{co}$, the amount of fragmentation is limited with only weak dependence $\tilde{\mu}$ and mean-field effects take over as the disorder is of minimal significance to the cloud's coherence.

To confirm our experimental finding that $\mu_{co} \simeq \Delta$, we perform a three dimensional Gross-Pitaevskii equation (3DGPE) simulation with experimental parameters as inputs (see Fig. 3.6b) [156]. Data from the simulation is analyzed in a manner identical to the experimental data and a very similar behavior of the damping rate is observed, with a minimum at $\tilde{\mu}_{co} = 0.26$ in good agreement with our experimental findings. We note that the factor of ~ 1.3 absolute discrepancy between the experimental and simulated rates

could result from the fact that the full 3DGPE does not account for depletion of the condensate.

3.6 Conclusions

In summary, we have demonstrated that interactions and disorder can compete to determine the transport properties of a lattice-trapped superfluid. The competition results in the decrease of the disorder-induced damping rate of BOs. Our findings for Bloch oscillations are also consistent with other recent transport measurements in disordered potentials, including dipole oscillations in a quasiperiodic potential [50] and in a 2D speckle potential [49]. The observed effect saturates at a minimum damping rate when the interaction energy becomes comparable to the characteristic energy scale of the disorder.

The interaction-induced delocalization effects observed here are also relevant for the description of systems ranging from superfluid helium in porous materials to superconductivity in granular or disordered materials [68, 69, 127, 128]. Here the competition between disorder and interactions ultimately contrasts with cooperative behavior in the regime of stronger interactions, which can give rise to strongly localized, disordered phases such as the Bose glass [55, 60]. Our findings in the crossover between the two regimes give an example of how subtle the parameter dependence can be in a given system.

Chapter 4

Nonadiabatic Diffraction of Matter Waves

While diffraction phenomena usually can be formulated in terms of a potential that induces the redistribution of a wave's momentum, we demonstrate in this chapter a novel regime of matter wave diffraction from an optical lattice in which the diffractive dynamics cannot be captured by the action of an optical potential, but in which the adiabatic dressed states are strongly mixed. We show how, in the adiabatic limit (characterized by strong coupling), the observed coupling between internal and external dynamics gives way to standard Kapitza-Dirac diffraction. We demonstrate the utility of our scheme for atom interferometry and discuss prospects for studies of dissipative superfluid phenomena.

The contents of this chapter are based on the preprint *Nonadiabatic Diffraction of Matter Waves*, arXiv 1505.06085, accepted for publication in Physical Review A (2015) [157].

4.1 Introduction

Diffraction, the bending of waves around obstacles, is one of the most fundamental and ubiquitous phenomena in optics, with a centuries-old history going back to the works of Grimaldi, Huygens, and Young on the wave nature of light. In the modern era, it has led to the understanding of x-rays [158, 159], has provided direct proof for the wave nature of particles [160], and today finds many applications in physics and materials science, ranging from electron, x-ray and neutron diffraction, to applications in atom optics [70, 161].

Quite generally, diffraction is caused by a position-dependent potential

with absorptive (imaginary) and/or dispersive (real) character. While the former includes material structures and diffraction gratings, an example for the latter is the ponderomotive potential exerted on electrons by an optical standing wave, as originally suggested by Kapitza and Dirac [162]. Kapitza-Dirac diffraction (KDD) of electrons was first demonstrated only fairly recently [163], long after the first observation of an analogous effect on neutral atoms based on the ac Stark shift near an atomic resonance [71]. It has also been applied to Bose-Einstein condensates (BEC) [5, 7] and has become an important and often-used tool in atom interferometry and metrology [70].

Here, we demonstrate a regime of diffraction for which the potential description does not describe the dynamics of the system. In our experiment, we diffract an atomic matter wave from a microwave-dressed optical lattice, with a diffractive dynamics that is qualitatively different from Kapitza-Dirac diffraction of dressed matter waves from a periodic optical potential. We note that the coherent mixing of states interacting with an external field is often used for the engineering of dressed potentials [96, 164–171]. Deviations from adiabaticity have previously been found to have deleterious effects on dressed-state lifetimes in rf-dressed lattices [172, 173]. In our experiment, we enter the strongly nonadiabatic regime, in which coherent Landau-Zener transitions of the atomic wave function between the adiabatic dressed potentials (driven by zero-point motion) induce a strong coupling between internal and external degrees-of-freedom, leading to a breakdown of the usual Born-Oppenheimer (adiabatic) approximation [30].

4.2 Kapitza-Dirac diffraction

For reference, we first describe the usual case of "adiabatic" diffraction. We focus on the atom optical implementation of diffraction in which an atomic sample (a trapped cold gas, atomic beam, or degenerate gas) interacts for a short time τ with a standing wave optical potential. Diffraction of atomic matter waves can be described in terms of the two-level Hamiltonian Eq. 2.10 with spatially varying Rabi couplings corresponding to the spatially periodic intensity pattern [161]

$$H = \frac{p^2}{2m} + \frac{\hbar}{2}\begin{pmatrix} 0 & \omega_R(t)\cos(k_{\mathrm{latt}}z) \\ \omega_R(t)\cos(k_{\mathrm{latt}}z) & -2\delta \end{pmatrix}. \tag{4.1}$$

To limit the effects of spontaneous emission, atomic diffraction is typically performed with light far detuned from resonance. This makes it possible to calculate an adiabatic potential felt by the atomic ground state. We consider

only the action of this adiabatic potential on the ground state atoms and write the Hamiltonian

$$H = \frac{p^2}{2m} + \frac{\hbar\omega_R(t)^2}{4\delta}\cos^2(k_{\text{latt}}z) \tag{4.2}$$

where the potential depth is given by Eq. 2.13. Working in the plane-wave basis by taking the ansatz

$$\Psi(z,t) = \sum_j c_j e^{-i(2j)k_{\text{latt}}z} \times e^{-i4j^2\hbar k_{\text{latt}}^2/(2m)t}, \tag{4.3}$$

with c_j is the amplitude for the plane wave state with $\langle p\rangle = 2j\hbar k_{\text{latt}}$, we can recover Eq. 2.35

$$i\dot{c}_j = \frac{E_r^{(2)}j^2}{\hbar}c_j + \frac{V_{\text{latt}}(t)}{4\hbar}(c_{j-1} + 2c_j + c_{j+1}) \tag{4.4}$$

where we have replaced the potential depth $V_{\text{latt}} = \hbar\omega_R(t)^2/(4\delta)$ and defined the $n-$photon recoil energy $E_r^{(n)} = n^2E_r$. To allow for easy solution of Eq. 4.4, we assume the time dependence of $\omega_R(t)$ to follow a simple rectangular pulse of duration τ. The solutions of this equation are typically split into the short pulse (Raman-Nath) regime and the long pulse (Bragg) regime [124]. These regimes differ in the relative importance of the detuning introduced by the kinetic energy of a diffracted (recoiling) atom. In the long pulse regime, the small uncertainty of the pulse energy prevents resonant excitation of the higher lying states. This leads to Pendellösung behavior in which atoms are exchanged between the $j = 0$ and the $j = \pm 1$ diffraction orders. This population oscillation never fully depletes initial $j = 0$ state without populating at least $j \geq 2$ orders.

In the short pulse limit, the kinetic detuning is washed out by the spectral width of the pulse. This allows for higher order scattering events to take place and the population of many diffracted orders when the potential depth V_{latt} is large. In this limit, we can ignore the kinetic term in Eq. 4.4 and find the solutions for the population in each diffraction order P_j in the form [5]

$$P_j = |c_j|^2 = J_j^2\left(\frac{V_{\text{latt}}\tau}{2\hbar}\right), \tag{4.5}$$

where $J_j(x)$ are Bessel functions of the first kind. This describes a spreading of the momentum wave packet due to the short interaction with the optical standing wave. For practical purposes, this picture and thus the wave packet spreading, is limited by the potential strength. For finite lattices and nonzero τ, the wave packet will undergo revivals.

We will explore below just how this picture breaks down in the limit of weak coupling, even while we are able to satisfy a resonant condition for all diffraction orders.

4.3 Experiment

Our experimental procedure, as sketched in Fig. 4.1a, uses microwave radiation to coherently couple an optically-trapped condensate of ^{87}Rb atoms (chemical potential $\mu = h \times 1.0(1)$ kHz in a 60Hz trap at 1064nm [89]) in internal state $|b\rangle = |F = 1, m_F = -1\rangle$ to another internal state $|r\rangle = |2, -2\rangle$ (separated from $|b\rangle$ by 6.8 GHz) exposed to a deep ($30E_r$) state-selective 1D optical lattice (wavelength $\lambda = 2\pi/k = 792$ nm, σ^+ polarization) not seen by the condensate [99, 174]. We study the transfer of population into the lattice upon applying a pulse of microwave radiation, as a function of the applied Rabi frequency Ω up to $h \times 17$ kHz, the pulse duration τ, and the detuning δ from the bare (i.e. no lattice) resonance between $|b\rangle$ and $|r\rangle$. In our experiments, residual magnetic-field instabilities limit the shot-to-shot stability of the $|b\rangle \leftrightarrow |r\rangle$ transition to $\delta_Z/2\pi \sim 0.6$ kHz; the typical uncertainty in the determination the Rabi frequency is ~ 0.2 kHz.

The presence of the lattice potential $V_r(z) = V_0 \sin^2(kz)$ modifies the microwave resonance condition, since the atoms in $|r\rangle$ are now confined to lattice orbitals $|n\rangle$ (band index $n = 0, 1, 2, ...$). In our effectively blue-detuned lattice, the orbital resonances are shifted upward by the zero-quasimomentum (q) band energies $\hbar\omega_n$. We characterize the lattice depth $V_0 = sE_r$ with $s = 30(2)$ in terms of the recoil energy $E_r = \hbar\omega_r = (\hbar k)^2/2m = h \times 3.7$ kHz, where m is the atomic mass (we also define the n-photon recoil energy $E_r^{(n)} = \hbar\omega_r^{(n)} = (n\hbar k)^2/2m$ used below). In the harmonic limit, $\hbar\omega_n \approx (n + \frac{1}{2})\hbar\omega_{ho}$, with $\hbar\omega_{ho} = 2\sqrt{s}E_r = h \times 40(1)$ kHz.

To study the orbital transfer, we first apply a rectangular microwave pulse of fixed duration $\tau = 60\mu$s and Rabi frequency $\omega/2\pi = 8.1$kHz (corresponding to a π-pulse in the bare case), but variable detuning δ. We determine the orbital populations P_n after applying the microwave pulse followed by a band-map sequence, consisting of a fast (1 ms) ramp down of the lattice depth, subsequent free expansion (18 ms), Stern-Gerlach separation of $|r\rangle$ and $|b\rangle$, and absorption imaging.* The spectroscopic location of the transitions, cf. Fig. 4.1b, is in excellent agreement with the expectation from the lattice calibration, with line shapes that follow theory for a Rabi pulse with a spectrally

*The band-map sequence prevents residual four-wave mixing during the time-of-flight evolution [174, 175]. We correct for differential detection efficiencies for $|r\rangle$ and $|b\rangle$ by removing correlations between $N_{b,r}$ and N_{r+b}.

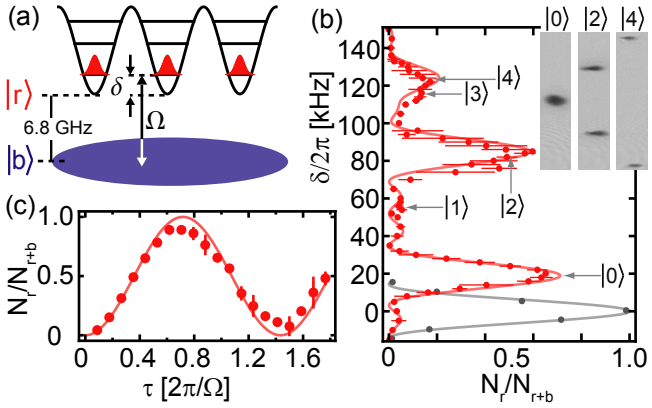

Figure 4.1: Experimental scheme for microwave induced diffraction. (a) Experimental scheme, for resonant coupling (see text). (b) Fraction of atoms in the $30E_r$ deep lattice after applying a rectangular pulse (coupling strength $\Omega/2\pi = 8.1$kHz, duration $\tau = 60\mu$s) for variable detuning δ. The red solid line is the incoherent sum of predicted line shapes for resonances centered at detunings given by the $q = 0$ level structure of the lattice; the pulse areas are $\pi\gamma_n$, where $\gamma_n = 0.72, 0, 0.61, 0, 0.32$ for $n = 0, 1, 2...$ are the Franck-Condon overlaps between BEC and the orbitals $|n\rangle$. The light gray points and line refer to a reference measurement without lattice (pulse area π). The inset shows time-of-flight absorption images after band-mapping, revealing the orbital populations. (c) Population dynamics in orbital $|0\rangle$ for resonant driving with $\Omega/2\pi = 8.8$kHz and $\delta/2\pi = 19.2$kHz. The curve is a resonant Rabi oscillation with frequency $\gamma_0\Omega$. All error bars represent statistical standard deviations of at least three experimental iterations.

limited FWHM of 14 kHz. However, while the free-space Rabi frequency is given by $\Omega = \langle r|\boldsymbol{\mu}\cdot\mathbf{B}|b\rangle/\hbar$, it now is modified by the Franck-Condon overlaps $\gamma_n = \langle n|\psi_0\rangle$ between the orbital Wannier functions $|n\rangle$ and the locally flat, single-particle BEC wave function $|\psi_0\rangle$. In particular, parity conservation imposes an orbital selection rule disallowing transfer to the odd-n orbitals. For the lowest orbital, $|0\rangle$, on which we will concentrate in the following, Ω is effectively reduced by $\gamma_0 = 0.72$.

We next study the coherent dynamics on resonance with the transition to the $|0\rangle$ orbital. For parameters comparable to the spectroscopic measurement, Rabi-type oscillations between BEC and orbital population can be observed for times up to $(\delta_Z)^{-1} \sim 0.3$ ms. The first cycle for resonant (within a systematic uncertainty of 1.1 kHz) coupling is shown in Fig. 4.1c. Comparing the fitted frequency to Ω yields a reduction by 0.70(1), consistent with the calculated Franck-Condon factor and the spectroscopic data. We note that

the oscillation amplitude is slightly reduced below unity, corresponding to a finite detuning of 1.5(1) kHz in the Rabi model, which is within the systematic lattice calibration error (and comparable to differential mean-field shifts from the density compression in the lattice [176]).

However, the simple Rabi picture breaks down for stronger couplings. We find that, while the measured oscillation frequency increases with Ω, the amplitude of the orbital population oscillation is strongly suppressed (by up to 30% for the maximum Ω), cf. Fig. 4.2a. At the same time, the population in $|b\rangle$ undergoes high-contrast, Pendellösung-type (albeit not number-conserving) oscillations between the initial momentum state $|p = 0\hbar k\rangle$ and $|p = \pm 2\hbar k\rangle$, cf. Fig. 4.2b, in phase with the population oscillation. As discussed further below, the coupled internal-external dynamics is the characteristic feature for the breakdown of the Born-Oppenheimer approximation. To further characterize the coupling, the fraction of atoms remaining in $|0\hbar k\rangle$ and the fraction of atoms transferred to $|\pm 2\hbar k\rangle$, for an effective π pulse with $\gamma_0 \Omega \tau = \pi$, are plotted together in Fig. 4.2c. We find that, as a function of Ω, the diffracted fraction increases rapidly once the coupling strength becomes comparable to $E_r^{(2)}$, while the population in $|0\hbar k\rangle$ gets suppressed nearly completely, cf. Fig. 4.2c. We note that for the smallest couplings $\Omega \lesssim 5$kHz a significant fraction of $|b\rangle$ atoms remain in $|0\hbar k\rangle$. However, this behavior is explained by the Rabi model if one allows for a small effective detuning of 1.1 kHz, which is similar to our experimental uncertainty for the microwave transition frequency.

4.4 Dressed states and adiabatic approximation

To capture the appearance of additional momentum orders, one might naively describe the effect of extracting atoms from the condensate as that of an imaginary potential formed by the $q = 0$ Bloch wave (i.e. the array of "absorbing" Wannier functions). However, as for the case of a real periodic potential, the observed complete depletion of the initial state $|0\hbar k\rangle$ in this case would entail significantly populating at least one higher order $|\pm 2j\hbar k\rangle$ ($j = 2, 3, ...$), while the observed Pendellösung dynamics involving $|0, \pm 2\hbar k\rangle$ exists only in the perturbative limit of a weak optical potential [124]. Our observations are thus qualitatively inconsistent with such a description.

In order to properly describe our system, we first write down the full Hamiltonian in the internal state basis $\{|r\rangle, |b\rangle\}$ after making a rotating wave ap-

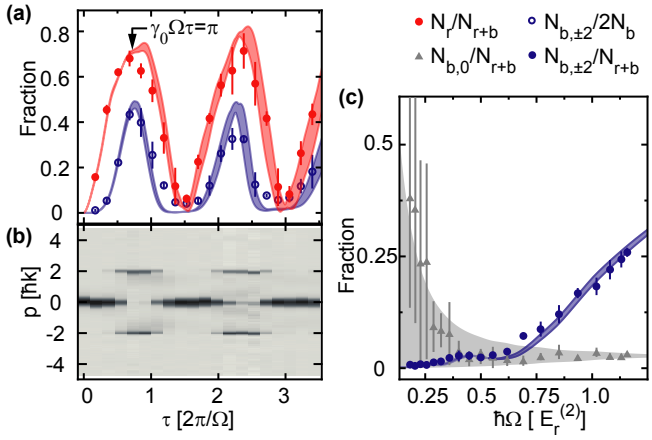

Figure 4.2: (a) Resonant orbital transfer to $|0\rangle$ and diffraction for stronger coupling $\Omega/2\pi = 16.9$kHz. Shown are the transferred fraction (red filled points), and the diffracted fraction (blue open circles) in the momentum state $|\pm 2\hbar k\rangle$. The red and blue shaded regions are the results of a numerical simulation including experimental uncertainties in δ and Ω. The population in higher orders (not shown) is less than 2% of the total number. (b) Observed diffraction patterns for $|b\rangle$ atoms. Shown is a sequence of time-of-flight images for varying pulse duration τ. Each line is a single image summed over the direction perpendicular to the lattice. (c) Total diffraction signal as a function of Ω for a Rabi pulse with $\gamma_0\Omega\tau = \pi$. The shaded blue (gray) area shows the band-structure prediction for atoms in the first diffracted order $N_{b,\pm2}/N_{r+b}$ (undiffracted fraction $N_{b,0}/N_{r+b}$) allowing for effective detunings up to 1.1 kHz (see text).

proximation,

$$H = \frac{\hat{p}^2}{2m}\mathbf{I} + \frac{\hbar}{2}\begin{pmatrix} 2V_r(z)/\hbar - \delta & \Omega \\ \Omega & \delta \end{pmatrix} \equiv H_T + H_V, \tag{4.6}$$

where $\hat{p} = -i\hbar\partial_z$ is the canonical momentum operator. Usually, one then diagonalizes H_V in order to obtain the dressed states $|\chi_i\rangle = \alpha_i|b\rangle + \beta_i|r\rangle$ $(i = 1, 2)$ and corresponding dressed optical potentials $\tilde{V}_i$, cf. Fig. 4.3a, and the state of the system evolving under H is then expressed as $\Psi = \Sigma_j c_j|\chi_j\rangle$. However, this approach only works if $\partial_z|\chi_j\rangle \ll \partial_z c_j$ (Born-Oppenheimer approximation) [30]. This is typically satisfied in optical potentials where both Ω and δ can be very large compared to the energy associated with the spatial variation of the coupling fields. In this limit, $\partial_z|\chi_j\rangle \sim 0$ and thus the resulting dressed potentials describe the eigenstates of the system. In our case (cf. Fig. 4.3a), the bare-state energies cross at two positions within each lattice site and for weak coupling (in our experiment, $\hbar\Omega \leq 0.17V_0$) the dressed-state mixing angle experiences a rapid spatial variation around these positions. Hence, the adiabatic condition is not fulfilled, and off-diagonal terms of the form $A_{ij} \propto \langle\chi_i|\hat{p}|\chi_j\rangle$ become significant, leading to momentum-dependent mixing of the adiabatic states. With inseparable kinetic and potential terms in H, the notion of an optical potential is not meaningful (i.e. the eigenstates associated with the adiabatic potentials do not describe the system dynamics), and we therefore diagonalize the full Hamiltonian H, with numerical results shown in Fig. 4.3b.

We first discuss the case of very weak microwave couplings $\hbar\Omega/E_r^{(2)} \ll 1$ (where $E_r^{(2)}/V_0 < 1$). Here, the energy levels are split by the two-level ac Stark shift corresponding to the leading-order matrix element in the coupling. For the energetically lowest states $|e_0\rangle$ and $|e_1\rangle$, the shifts are given by $\pm 0.72\hbar\Omega/2$, consistent with the Franck-Condon overlap γ_0 of the states $|b, 0\hbar k\rangle$ and $|r, n = 0\rangle$ between which the Rabi oscillation is observed. The next-higher $|e_\pm\rangle$ states experience a shift due to off-resonant coupling of the symmetric (antisymmetric) momentum-state combinations $(|b, 2\hbar k\rangle \pm |b, -2\hbar k\rangle)/\sqrt{2}$ to $|r, n = 0\rangle$ $(|r, n = 1\rangle)$. For all Ω of experimental interest, these are the primary couplings describing the dressed levels (note that parity conservation forbids population of the state $|e_-\rangle$).

For intermediate couplings $\hbar\Omega \sim E_r^{(2)}$, the admixture of the symmetric momentum-state combination to $|e_0\rangle$ and $|e_1\rangle$ induces a downward curving of their energies and gives them the periodicity of the lattice, cf. Fig. 4.3c. While at $t = 0$ the two states add to produce $|b, 0\hbar k\rangle$, at $\Omega t \approx \pi/(\gamma_0)$ they acquire a π phase shift and add to $(|b, 2\hbar k\rangle + |b, -2\hbar k\rangle)/\sqrt{2}$, which produces the observed diffraction pattern (with a small contamination by $|b, 0\hbar k\rangle$ due to the admixture of $|e_+\rangle$).

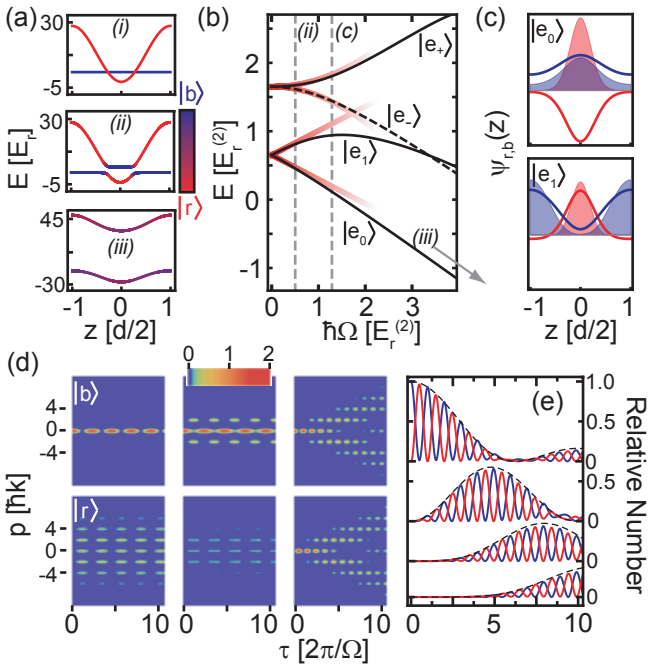

Figure 4.3: Calculated dynamics from the nonadiabatic regime to the adiabatic regime. (a) (i-iii) Adiabatic dressed potentials for coupling strengths $\hbar\Omega = \{0, 1, 15\}E_r^{(2)}$ and s=30. The position dependent internal state composition is encoded in color. (i) shows the bare potentials, while (iii) shows potentials in the adiabatic limit characterized by a near-constant dressed-state mixing angle. For weak coupling (ii), gaps are small and the mixing angle varies rapidly. (b) Nonadiabatic $q = 0$ band energies for the four lowest states as a function of Ω with $\delta = \hbar\omega_0$. The dashed line is a state of opposite parity that is decoupled from the other three states. (c) Spatial structure of the ground and first excited states in the bare-state basis, for $\hbar\Omega = 1.25E_r^{(2)}$. The shaded red and blue areas denote the square of the wave function, and the solid lines the wave function itself. (d) Diffractive dynamics in three regimes characterized by $\Omega/V_0 = 0.01, 0.05, 15$ with $V_0 = 100E_r$, and (e) internal state dynamics in the case $\Omega/V_0 = 15$. The red and blue lines trace total population in $|r\rangle$ and $|b\rangle$ while the dashed lines represent the expected envelopes for the $m = 0, 1, 2, 3$ (from top to bottom) diffraction orders for standard Kapitza-Dirac diffraction.

Strong couplings $\hbar\Omega \gg E_r^{(2)}$ lead to the admixture of higher-order momentum-state combinations, and since $E_r^{(2)} \sim \hbar\omega_{ho}$ (for $s \sim 10$) the dynamics also involves higher even orbitals. Taken together, the internal and external dynamics eventually decouple: the internal dynamics proceeds as a fast oscillation between $|b\rangle$ and $|r\rangle$ (with Rabi frequency Ω), while in the rotating frame the adiabatic dressed states $|\chi_{1,2}\rangle = (|b\rangle \pm |r\rangle)/\sqrt{2}$ undergo diffraction in the half-depth optical potentials $V_{1,2} = V(z)/2 \pm \hbar\Omega/2$, with populations $P_n(\tau) = J_n^2[V_0\tau/4\hbar]$ spread over many orders n as expected for standard Kapitza-Dirac diffraction Fig. 4.3d and 4.3e. Indeed, for a π-pulse with $\tau\Omega \sim \pi$, the condition $\Omega \gg \omega_{ho}$ reproduces the usual Raman-Nath criterion $\tau\omega_{ho} \ll 1$ [5]. The predicted transition from weak to strong coupling is illustrated in Fig. 4.3d. We caution that using our scheme in this adiabatic limit would require increasing the microwave power by three orders of magnitude, which is outside our technical capabilities.

Our model accurately reproduces all the observed dynamics for $\hbar\Omega \approx 4E_r^{(2)}$ shown in Fig. 4.2. We note that the narrowing of the diffraction signal in Fig. 4.2b (as compared to the orbital transfer) is easily explained by considering that the signal gets more pronounced with the depletion of the background in $|b, 0\hbar k\rangle$.

4.5 Satisfying the adiabatic condition

In the previous section, it is noted that we can reproduce typical adiabatic diffraction patterns in the limit of very strong microwave coupling. The huge microwave powers needed prevent this from being easily achieved; however, it is possible to examine the transition to adiabaticity along another path in parameter space. The adiabatic potentials describe the dynamics of the Hamiltonian, equation (4.6), as long as the mixing angle does not vary strongly in space. The mixing angle $\theta(z)$ for a two-level system is given by $\cos 2\theta(z) = -\delta(z)/\sqrt{\Omega + \delta(z)^2}$, where $\delta(z)$ includes the spatial detuning introduced by the state dependent potential. It can clearly be seen that for large Ω ($\langle\delta(z)\rangle_z$), $\theta(z) \to \pi/4$ ($\to 0$). In either case, the spatial dependence of θ becomes negligible.

Though we do not access the large Ω limit, we can observe a transition to adiabaticity by increasing the overall detuning such that δ becomes comparable to V_0. The dynamics of the system, c.f. Fig. 4.4, transition from being described by the nonadiabatic spectrum described in Fig. 4.3, to being described by the generalized Rabi model with population dynamics described by frequency $\tilde{\Omega} = \sqrt{\Omega^2 + \delta^2}$. In an intermediate regime, with $\delta \sim 4E_r$, the two time scales can readily be seen in the dynamics of the system, c.f. Fig. 4.4a.

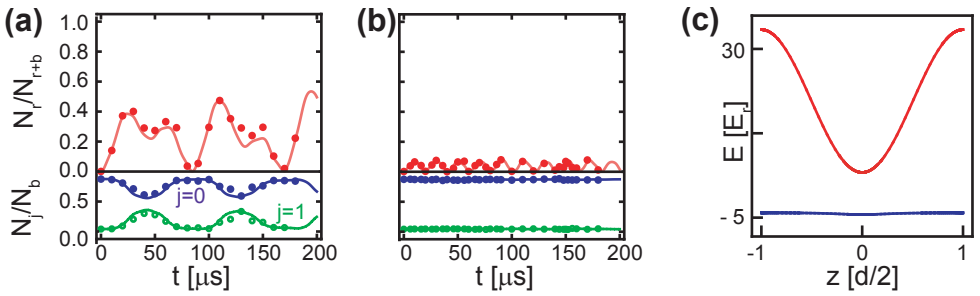

Figure 4.4: Transition to adiabatic dynamics in large detuning limit. (a) Dynamics for $\Omega/2\pi = 17$ kHz, $\delta \sim E_r^{(2)}$, two separate timescales can easily be discerned. These correspond to the dressed potential splitting and the timescale set by the two-photon recoil. (b) For larger detuning $\delta \sim 3E_r^{(2)}$, Rabi oscillations at the generalized Rabi frequency anticipated by the two-level Rabi model are recovered. In (a) and (b) the upper portions show the population oscillation of $|r\rangle$ in red, the lower sections show $N_{b,0\hbar k}$ in blue and $N_{b,\pm 2\hbar k}$ in green. (c) The dressed states in this limit are split by δ and feature very weak mixing of the bare states. As seen in the color code, the mixing angle is largely uniform within one lattice site.

For larger detunings, e.g. $\delta \sim 13E_r$ in Fig. 4.4b, we recapture the typical Rabi dynamics with oscillation frequency consistent with the generalized Rabi frequency.

Because the population transfer in the limit is very weak, we observe no significant diffraction of the bath. This is expected if the adiabatic potentials Fig. 4.4c are considered. Here, the dressed potentials do not exhibit strong mixing of $|r\rangle$ and $|b\rangle$ and the dressed potential for the mostly $|b\rangle$ state remains flat. Previous experiments have adiabatically prepared the dressed states studied here in the strong coupling limit and noted the formation of periodic structures in the atomic species not confined to the lattice [170, 173]. On the other hand, we study these states in the time domain and demonstrate coherent dynamics in the dressed state picture.

4.6 Application to interferometry

As a simple application of our orbital transfer scheme going beyond mere diffraction, we implement an in-situ detection scheme for matter wave interferometry, in which the initially unpopulated lattice sites act as an array of probes for the condensate, cf. Fig. 4.5a. The orbital transfer can be viewed as (microwave-induced) local tunneling of atoms into individual lattice sites.

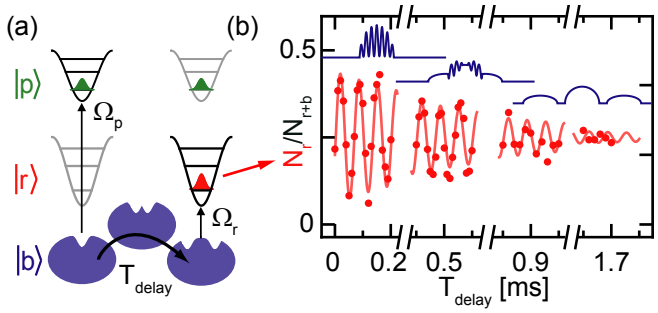

Figure 4.5: In-situ probing of matter wave interference. (a) A pump pulse ($\gamma_0\Omega\tau = 2\pi/3$, $\tau = 40\mu$s)) creates excitations in the BEC by removing atoms into a second trapped state $|p\rangle \equiv |2,-1\rangle$, and is followed by free evolution of the BEC density profile for time $T_{\rm delay}$ before a probe pulse ($\gamma_0\Omega\tau = 2\pi/5$, $\tau = 14\mu$s) transferring atoms into the trapped state $|r\rangle$. (b) Probe pulse yield as a function of delay time, displaying oscillations at the recoil frequency. The solid line is an oscillatory fit with frequency $\omega/2\pi = 15.0$ kHz, and damping time $\tilde{\tau} = 0.66$ms, corresponding to the beat note and characteristic time for the wave packets separating after the probe pulse. The insets illustrate the evolving wave-packet interference after application of the pump pulse.

When the transferred atoms are detected, the operation is thus reminiscent of that of a tunneling electron microscope. We first imprint a modulation into the BEC ("pump"), again using orbital transfer. To keep this step separate from the subsequent detection ("probe"), a third internal state $|p\rangle \equiv |2,-1\rangle$ with a lattice potential $V_p = (2/3)V_r$ is used, precluding any coherence effects in detection. Figure 4.5b shows the resulting probe signal N_r as a function of the time delay $T_{\rm delay}$ between the two pulses. We observe an oscillation in N_r, consistent with an on-site beat note at $\omega_r^{(2)}$, generated by matter wave interference between recoiling $|b,\pm 2\hbar k\rangle$ and stationary $|b,0\hbar k\rangle$ packets. The decaying envelope reflects a gradual loss of spatial overlap between the wave packets. Compared to Kapitza-Dirac-based matter wave interferometry schemes [177, 178], our 2-pulse sequence allows for a direct, in-situ detection of the matter wave interference contrast, without the need for an additional probe laser.

4.7 Conclusion and outlook

In the present chapter, we have studied the dynamics of a BEC coupled to the orbitals of an array of lattice sites. We point out that we do not observe effects of the collisional interaction μ (such as a modification of the

ground-state wave functions [179]), as it is on the order of fluctuations of the orbital-resonance frequency. In the interacting regime $\hbar\Omega < \mu$, the healing length $\xi = \hbar/(2m\mu)^{-1/2}$ is compatible with phonon excitation in the BEC, at a wavelength $\lambda_s/(2\pi) = (\mu/m)^{1/2}/\Omega = (\mu/\hbar\Omega)\xi > \xi$. The coupling of the single-site dynamics to phonons should allow for the study of dissipative phenomena [63], including dissipative quantum phase transitions driven by phonon-mediated coupling between sites [74]. The physics of these systems and methods for engineering them will be discussed in Chapter 5. Entering this regime in our setup will require a reduction of the ambient-magnetic field fluctuations down to $\lesssim 100\mu$G, which is reachable with present-day technology.

In summary, we have demonstrated a novel regime for the diffraction of weakly-dressed matter-waves from an optical lattice. In this regime, nonadiabatic transitions induce a strong coupling between the internal and external degrees-of-freedom, such that a description of the diffracting object through a potential is not possible. In the limit of strong microwave coupling, the decoupling of the internal and external dynamics results in the well known Kapitza-Dirac diffraction from an optical potential. While the coherent internal dynamics give rise to particle-like excitations in the regime explored in this work, an extension into the regime of even weaker microwave coupling, in which the superfluid excitations become sound-like, should prove useful in the study of dissipative phenomena.

Chapter 5

Towards the Realization of a Dissipative Quantum Model

In this chapter, we consider a proposed implementation of the so called spin-boson model using an ultracold atomic system. The spin-boson model describes the controlled coupling of a two-level system to a dissipative bath and allows for the study of decoherence and dissipation in open quantum systems. While a bath can in principle be easily realized using an ultracold or quantum degenerate atomic gas, the implementation of an effective two-level system coupling to it is more challenging. Since differential interactions between hyperfine states for ultracold atoms can be weak,* this endeavor may involve realizing effective spins, such as mapping the occupation number of a lattice site or the use of motional states of a lattice potential (similar to ion trap qubits) [34, 180]. We further note that the manipulation of the motional degrees of freedom of a lattice-trapped gas has led to a number of other effective spin models and has been useful in engineering novel Hamiltonians [25, 27, 29, 31, 34–36, 181, 182]. This chapter will focus on experimental techniques that may be used to implement localized, driven spin impurities coupled to a superfluid. We highlight three possibilities for implementing such an effective spin in our experiment, and preliminary experimental results for, and the prospects of, each option are presented.

5.1 The model

Macroscopic objects rarely exhibit quantum effects due to their many degrees of freedom and coupling to the environment. In defining a system interacting

*Use of a Feshbach resonance or species with large differential scattering lengths can overcome this limitation.

with an environment, one starts by selecting the degrees of freedom of importance to the system and integrating out the remaining degrees of freedom pertaining to the environment. We consider here the two-level spin system and its interaction with a superfluid, c.f. Fig. 5.1. While dynamics of the spin in the superfluid will be of concern, the dynamics of the superfluid itself will be ignored. We start by considering a bath of bosonic harmonic oscillator modes. This so-called spin-boson model can be written down as [75, 183]

$$H_{\mathrm{SB}} = -\frac{\hbar\Delta}{2}\sigma_x - \frac{\hbar\epsilon}{2}\sigma_z + \frac{1}{2}\sum_\alpha \left(\frac{p_\alpha^2}{m_\alpha} + m_\alpha\omega_\alpha^2 x_\alpha^2 - \sigma_z c_\alpha x_\alpha\right). \tag{5.1}$$

Here, the first two terms describe the two-level system (much like Eq. 2.10) with tunneling (coupling) Δ and bias (detuning) ϵ; $\sigma_{x,y,z}$ are the Pauli matrices. The sum is over bosonic modes, with $[x_\alpha, p_\alpha] = i\hbar$, indexed by α. Within the sum, the bosons each have kinetic and potential energies, and the third term describes the interaction of the spin with each bosonic mode. This interaction can be thought of as a fluctuating polarization energy or bias $\mathcal{E}(t) = 1/2\sum_\alpha c_\alpha x_\alpha(t)$ with coupling strength c_α (for details see [75, 183]).

We define the familiar bosonic annihilation and creation operators; $\hat{b}_\alpha$, $\hat{b}_\alpha^\dagger$, with $[\hat{b}_\alpha, \hat{b}_{\alpha'}^\dagger] = \delta_{\alpha,\alpha'}$, using

$$x_\alpha = \sqrt{\frac{\hbar}{2m_\alpha\omega_\alpha}}(\hat{b}_\alpha + \hat{b}_\alpha^\dagger) \qquad \text{and} \qquad p_\alpha = i\sqrt{\frac{\hbar m_\alpha\omega_\alpha}{2}}(\hat{b}_\alpha^\dagger - \hat{b}_\alpha) \tag{5.2}$$

This leads to a reformulation of Eq. 5.1 as

$$H_{\mathrm{SB}} = -\frac{\hbar\Delta}{2}\sigma_x - \frac{\hbar\epsilon}{2}\sigma_z - \frac{1}{2}\sigma_z\sum_\alpha \hbar\lambda_\alpha(\hat{b}_\alpha + \hat{b}_\alpha^\dagger) + \sum_\alpha \hbar\omega_\alpha\hat{b}_\alpha^\dagger\hat{b}_\alpha \tag{5.3}$$

where bosonic mode α is coupled to the spin with strength

$$\lambda_\alpha = \sqrt{\frac{c_\alpha^2}{2\hbar m_\alpha\omega_\alpha}}. \tag{5.4}$$

The third term encapsulates coupling between bosons and the spin state, while the fourth term gives the total energy of the bosonic field (zero-point energy disregarded).

The details of the coupling are given by the bath's spectral density

$$J(\omega) = \sum_\alpha \lambda_\alpha\delta(\omega - \omega_\alpha). \tag{5.5}$$

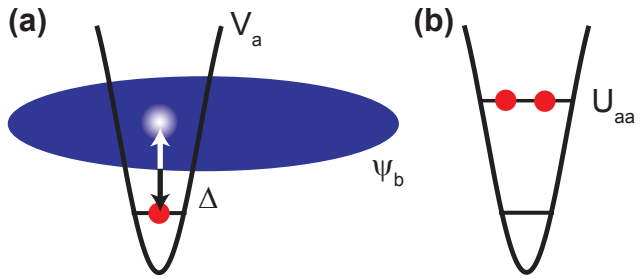

Figure 5.1: Atomic occupational spins in a bath. (a) A strongly localizing state dependent optical trap V_a is coupled to a bath, ψ_b, via microwave or Raman transitions with Rabi frequency Δ.(b) Interactions between localized atoms U_{aa} prevent multiple occupations of the site.

Let us consider how this system can be engineered in our ultracold atomic system and look at the implications of a bath of phonon modes in a superfluid. To this end, we consider detailed proposals from [63, 184]. A schematic of the proposed system is sketched in Fig. 5.1. A strongly confined atom in a state-selective potential well is immersed in a degenerate Bose gas. External coupling (derived from Raman lasers or microwaves as in Chapter 4) drives internal state transitions (with Rabi frequency ω_r) between the trapped state labeled $|a\rangle$ and untrapped states, i.e. the Bose gas labeled with $|b\rangle$. The localized atoms interact strongly with Hubbard U_{aa}, thus multiple occupation of the site is energetically forbidden due to collisional blockade. The interaction between the localized atom $|a\rangle$ and the bath $|b\rangle$ can then be described by the Hamiltonian [63, 184]

$$H_a + H_{ab} = \left[-\hbar\delta_0 + g_{ab} \int d\mathbf{x} |\psi_a(\mathbf{x})|^2 \hat{\rho}_b(\mathbf{x}) \right] \hat{a}^\dagger \hat{a} + \frac{U_{aa}}{2} \hat{a}^\dagger \hat{a}^\dagger \hat{a} \hat{a} + \int d\mathbf{x} \hbar\omega_r (\hat{\Psi}_b(\mathbf{x}) \psi_a(\mathbf{x}) \hat{a}^\dagger + \text{h.c.}), \tag{5.6}$$

where we have the annihilation (creation) operators for the localized atom $\hat{a}^{(\dagger)}$ and $\hat{\rho}_b(\mathbf{x})$ is the density operator for the bath atoms with bosonic field operators $\hat{\Psi}_b(\mathbf{x})$. The first term includes the detuning δ_0 and collisional interactions with interspecies g_{ab}. The second term describes a collisional blockade for atoms in ground state wave function $\psi_a(\mathbf{x})$. The last term describes the induced coupling between a and b atoms.

The Bose gas is assumed to be degenerate, described hydrodynamically by

the Hamiltonian

$$H_b = \frac{1}{2}\int d\mathbf{x}\left(\frac{\hbar^2}{m}\rho_b|\nabla\hat{\phi}|^2(\mathbf{x}) + g_{bb}\hat{\Pi}(\mathbf{x})\right), \tag{5.7}$$

with density ρ_b and intraspecies interaction g_{bb}. Here, we have introduced the phonon operators in terms of the canonical pair of phase $\hat{\phi}(\mathbf{x})$ and fluctuation $\hat{\Pi}(\mathbf{x})$ operators

$$\hat{\phi}(\mathbf{x}) = i\sum_{\mathbf{q}}\left|\frac{mv_s}{2\hbar\mathbf{q}V\rho_b}\right|^{1/2} e^{i\mathbf{q}\cdot\mathbf{x}}(\hat{b}_{\mathbf{q}} - \hat{b}^\dagger_{-\mathbf{q}}) \tag{5.8}$$

$$\hat{\Pi}(\mathbf{x}) = \sum_{\mathbf{q}}\left|\frac{\hbar\mathbf{q}\rho_b}{2v_sVm}\right|^{1/2} e^{i\mathbf{q}\cdot\mathbf{x}}(\hat{b}_{\mathbf{q}} + \hat{b}^\dagger_{-\mathbf{q}}) \tag{5.9}$$

with phonon wave vector $\mathbf{q}$, speed of sound v_s, and volume of the condensate V.

Working in the perturbative limit such that $\rho_b(\mathbf{x}) \approx \rho_b(\mathbf{x}) + \hat{\Pi}(\mathbf{x})$ and assuming long wavelength excitations (small $\mathbf{q}$ such that $\hat{\Pi}(\mathbf{x}) \approx \hat{\Pi}(0)$) under the condition $U_{aa}/\hbar \gg \delta_0, \omega_R$ it is possible to map Eqs. 5.6, and 5.7 onto the spin-boson Hamiltonian Eq. 5.1 [63, 184], by setting $\omega_r = \Delta$ and $\epsilon = \delta_0$. The sum is now over phonon modes indexed by wave vector $\mathbf{q}$. Given the contact interaction between the localized spin and the superfluid, we find the phonon coupling parameter

$$\lambda_{\mathbf{q}} = \left|\frac{g_{bb}\omega_{\mathbf{q}}}{2\hbar V}\right|^{1/2}\left(\frac{g_{ab}}{g_{bb}} - 1\right). \tag{5.10}$$

With phonon coupling of this form, we find the spectral density is given by $J(\omega) \propto (g_{ab}/g_{bb} - 1)^2\omega^{\mathcal{D}}$ for a $\mathcal{D}$-dimensional bath. Here we immediately see the importance of differential interactions in the prefactor to $\omega^{\mathcal{D}}$.

When $\mathcal{D} > 1$, the system realizes "super-Ohmic" dissipation, which leads to damped oscillations [63]; such dissipation is analogous to spontaneous emission of an excited atom in free space.

For $\mathcal{D} = 1$, corresponding to "Ohmic" dissipation, the physics exhibits nontrivial dynamics. In one dimension, the system undergoes a dissipative quantum phase transition for $\alpha \approx (g_{ab}/g_{bb} - 1)^2 = 1$. For $\alpha < 1$, the spin exhibits damped Rabi oscillations, but for $\alpha > 1$, the spin can become frozen in the "spin-up" (occupied trap) state, as is discussed in detail in [75].

The spin-boson model in atomic gases has been generalized to extended spin arrays coupled to a shared bath [74]. This model exhibits similar order-disorder quantum phase transitions and is naturally applicable to our state-dependent lattice.

5.2 Options for implementation

For the model above, we discuss possible generalizations of the two-level spin in order to identify an optimal system which allows for tunable interactions and coupling strengths. We focus here on using the internal state degrees of freedom and lattice degrees of freedom to create pseudospin models.

5.2.1 Occupational spin

Let us first consider the spin described in the previous section. Chapter 4 demonstrates the relevant theory and experimental technique behind driving transitions between the bath $|b\rangle$ and localized states $|a\rangle$. To successfully realize this model, we must work in the collisional blockade where U_{aa} is the largest energy scale in the system. This will require a very strongly confining state dependent trap (such as a lattice site in our state dependent optical lattice). For $U_{aa}/\hbar \gg \delta_0, \omega_R$, the Rabi driving leads to the transfer of maximally a single atom per site, due to the large detuning associated with the multiply occupied potential well [185–187]. This collisional blockade allows us to associate the Fock states $n_a = 1$ with $|\uparrow\rangle$ and $n_a = 0$ with $|\downarrow\rangle$ and thus create an "occupational spin."

We also note that the phonon coupling strength scales with $\alpha \sim (g_{ab}/g_{bb} - 1)^2$; to maximize the coupling effects, an interspecies Feshbach resonance is required. For any pair of ^{87}Rb hyperfine ground states, typical differential interactions are $g_{ab} = (1 \pm 0.03)g_{bb}$ [188], limiting the coupling strength. Fortunately, there exist low field ($\sim$ 9 G) Feshbach resonances in ^{87}Rb that should allow us to adjust the elastic interspecies scattering length up to 30% [188], allowing for stronger coupling to the phonon bath. Associating $|\uparrow\rangle \equiv |F = 2, m_F = 0\rangle$ and $|\downarrow\rangle \equiv |F = 1, m_F = 1\rangle$ would allow for occupational spins to be realized using the microwave coupling described above and the scheme realized here.

5.2.2 Internal states

A second natural candidate for a spin in any atomic system utilizes the internal states of the atoms themselves. For localized spins, this setup would require the use of atomic clock states in the ^{87}Rb ground state which experience nearly identical state-dependent lattice potentials. The spins are Rabi coupled by two-photon transitions, c.f. Fig. 5.2. The localized spins would interact collisionally with the superfluid consisting of a third hyperfine ground state.

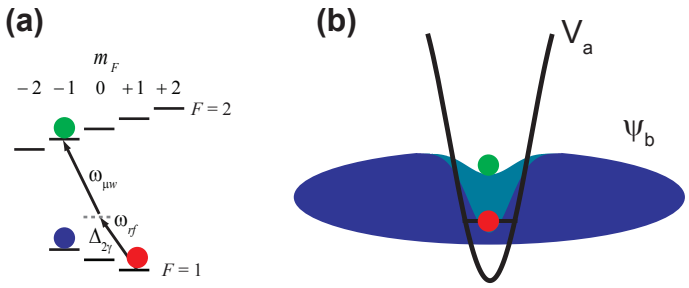

Figure 5.2: The internal state spin. A strongly localizing state dependent optical trap V_a traps an atom driven on a clock transition between hyperfine states. The transitions is driven by two field with radio and microwave frequencies ω_{rf} and $\omega_{\mu w}$ decoupled from the intermediate state by two photon detuning $\Delta_{2\gamma}$. The atom $|a\rangle$ is immersed in a superfluid bath of $|b\rangle$ atoms with wave function ψ_b, with which the trapped atomic states have differential interactions with the superfluid atoms.

This scheme for spins can be realized by defining the spin to consist of $|\downarrow\rangle \equiv |1,1\rangle$ and $|\uparrow\rangle \equiv |2,-1\rangle$ while the background environment would consist of weakly trapped gas of $|2,-2\rangle \equiv |\mathrm{bg}\rangle$. To achieve differential interaction strengths with the background, we can again turn to a Feshbach resonance [188]. A Feshbach resonance between $|\mathrm{b}\rangle$ and $|\downarrow\rangle$ establishes a tunable differential interaction strength that, in principle, allows even for a decoupling of the spin from the bath.

5.2.3 Vibrational levels

A second set of discrete levels that can be selectively addressed consists of the quantized motional levels of the lattice, see Fig. 5.3. An effective spin can be created by applying a drive, such as lattice amplitude or phase modulation, that couples vibrational degrees of freedom of the potential. Alternatively, Bragg or Raman lasers can be used to drive transitions between internal states and vibrational levels of the lattice [182, 189].

Bands of opposite parity can be addressed by "shaking" the lattice via phase modulation. The time-dependent potential we consider here is given by

$$V(z,t) = V_0 \cos^2\left[k_1(z + z_0(t))\right] \tag{5.11}$$

where $z_0(t)$ describes the displacement of the lattice. The simple case is given by $z_0(t) = L\sin(\omega t + \phi)$, with L the amplitude of the lattice displacement in space with frequency ω and arbitrary phase ϕ. In the frame co-moving with

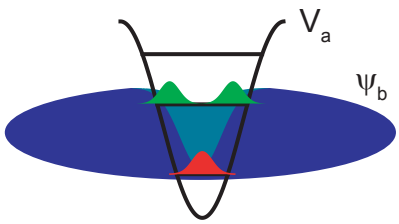

Figure 5.3: An orbital level spin. A strongly-localizing state dependent optical trap V_a traps an atom immersed in a superfluid bath ψ_b. Raman lasers (or parametric modulation of the trap) drive transitions between orbital levels of the localizing trap V_a, giving rise to differential interactions with the superfluid.

the lattice, a coordinate transformation recasts Eq. 5.11 as

$$V(z,t) = V_{\text{latt}} \cos^2(k_{\text{l}} z) + mL\omega^2 z \cos(\omega t) \tag{5.12}$$

thus introducing a time-dependent term describing an inertial force [190, 191].† Using this transformed potential and for modulation near resonance with the band splitting Δ_{gap} we write an effective two-level model in analogy with Eq. 2.5

$$H = H_{\text{a}} + H_{\text{int}} = \hbar\Delta_{\text{gap}}|n\rangle\langle n| + V_{\text{latt}} \cos^2(k_{\text{l}} z) + mL\omega^2 z \cos(\omega t) \tag{5.13}$$

where the assumed basis states are the relevant Bloch waves (or equivalently Wannier functions). Paralleling the derivation in Chapter 2, we can write a Rabi frequency for the transition between lattice bands $|n\rangle$ and $|n+1\rangle$.

$$\Omega_n = \frac{2mL\omega^2}{\hbar}\langle n+1, q|z|n, q\rangle \tag{5.14}$$

which has general behavior illustrated in Fig. 5.4. Note that the z perturbation only couples bands with $\Delta n = 1$‡. We consider an effective spin formed by the s ($n = 0$) and p-bands ($n = 1$) of a strongly-confining lattice (denoted again as $|\downarrow\rangle$and $|\uparrow\rangle$ respectively), see Fig. 5.6a.

Using vibrational levels as spins may naturally provide a differential colli-

†It should be noted that the transformation in Eq. 5.12 requires the atoms to adiabatically follow the lattice, i.e. $\omega \ll \omega_{\text{ho}}$. While this is not true when $\hbar\omega$ approaches the band gap, we can still get an intuitive picture of the physics involved here

‡A similar Rabi frequency can be found for amplitude modulation $\Omega_{n,n+2j} = \frac{\alpha V_0}{i\hbar}\langle n|\cos^2 k_{\text{l}} z|n+2j\rangle$, which connects bands separated by $\Delta n = 2j$ for $j = 1, 2, 3, ...$

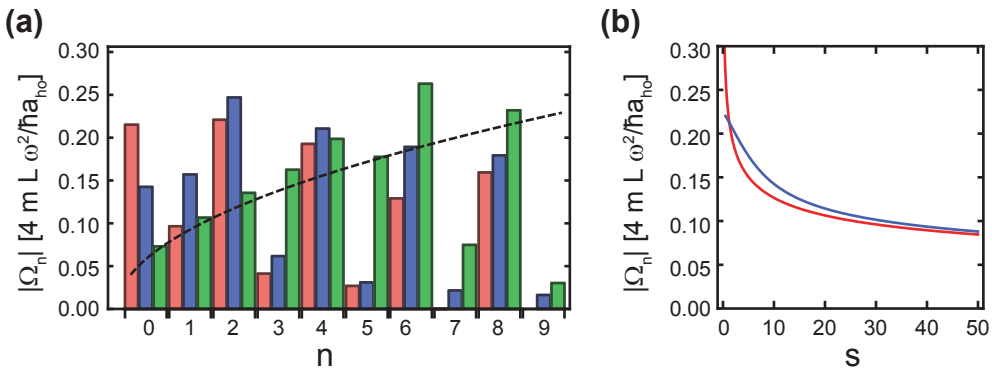

Figure 5.4: Rabi frequencies for shaken lattice. (a) Amplitude of matrix elements $|\langle n+1|z|n\rangle|$ for $s = 1, 10, 100$ (in red, blue, green respectively). The dashed line represents the harmonic oscillator limit for $s = 100$. (b) Amplitude of the matrix element $|\langle 1|z|0\rangle|$ as a function of s is plotted in blue. The red line represents the harmonic oscillator limit for a lattice of depth $V_{\text{latt}} = sE_r$.

sional interaction strength. Consider the energy U of the interaction with the superfluid

$$U = g_{ab} \int d\mathbf{x} |w_a^{(n)}(\mathbf{x})|^2 \hat{\rho}_b(\mathbf{x}), \tag{5.15}$$

with the Wannier state $w_a^{(n)}(\mathbf{x})$, for the localized atom in band n. In the long wavelength limit as considered in Eq. 5.3, $U = g_{ab}\hat{\rho}_b(0) * V$ does not depend on the band index n. Therefore, applications of this spin model will require more careful consideration of the b atoms' local response to the impurity wave function, as the total energy will depend on the curvature of $\psi_b(\mathbf{x})$. One may intuit, however, that the larger spatial extent of a vibrationally excited state will require more "gentle" curvature of $\psi_b(\mathbf{x})$ and lead to an effectively reduced spin-bath interaction energy compared to the $n = 0$ state.

5.3 Implementation and evaluation

The above methods have been experimentally explored in our apparatus, each having its own advantages and limitations. Below, we consider each method's practical prospects and discuss results associated with each measurement.

5.3.1 Coherence times

To access the long-wavelength phonon excitations the driving energy Δ must be small compared to the local mean field μ. Practical considerations in our experiment, set $\mu/\hbar \approx 2\pi \times 1$ kHz. Thus, to avoid creation of particle-like excitations, $\Delta \lesssim 2\pi \times 500$ Hz would be ideal. This requires long spin coherence times; for this purpose any damping and or decoherence must be understood and eliminated.

Hyperfine-state degrees of freedom

In the case of internal state based pseudospins, the main damping/dephasing mechanisms seem to be due to instability of the bias magnetic field. Based on measurements of the ambient field using a fluxgate magnetometer (Bartington Instruments, Mag-03MS1000), we estimate the ac-line-driven field fluctuations to have a magnitude of ~ 5 mG and offset drifts on the order of ~ 1 mG/hour. This is particularly concerning for the occupational spin as realized in our apparatus, since the microwave transition resonance center shifts by ~ 2.1 kHz/mG. Synchronizing the experiment timing to the 60 Hz ac-power-line signal can mitigate these issues. As discussed in Chapter 4, for the $|1,-1\rangle \leftrightarrow |2,-2\rangle$ transition, we experience only ~ 300 μs of coherent oscillation,[§] corresponding to shot-to-shot fluctuations on the order of 0.1 mG. In order to observe Rabi oscillations at 500 Hz, this number would need to be improved by at least an order of magnitude.

Using a clock-state transition requires a two-photon transition, this second-order coupling naturally provides a narrow resonance feature, plotted in Fig. 5.5a. Furthermore, the clock states allow for long lived Rabi oscillations due to insensitivity to background field fluctuations, where the bias field-induced detuning is on the order of $\sim 10^{-2}$ Hz/μG. The 20 ms of high contrast oscillation plotted in Fig. 5.5b compares very favorably with $< 500\mu$s of stability observed for magnetically sensitive transitions described above.

Orbital degrees of freedom

To engineer the coupling model described in Eq. 5.13, we realize a shaken lattice by passing the retroreflected lattice beam through a pair of AOMs arranged to give a time-dependent frequency difference $\Delta\nu(t)$ between the interfering lattice beams, for details see [87]. This frequency difference is related to the lattice shake amplitude by $L = \pi\Delta\nu_{\max}/(k_{\text{latt}}\omega)$. After applying

[§]Using the $|1,1\rangle \leftrightarrow |2,0\rangle$ as proposed above would result in a factor of 3 improvement in these numbers.

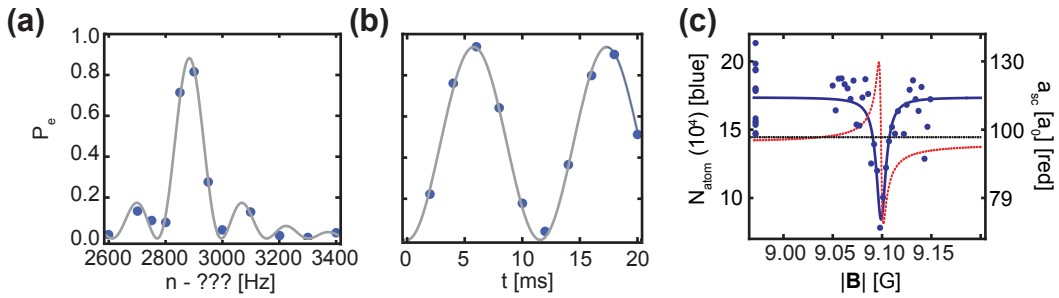

Figure 5.5: Properties of the internal state spin. (a) Two photon resonance, the width of the resonance is just ~ 100 Hz. (b) Two photon Rabi oscillations with Rabi frequency of ~ 80 Hz. Here, we see coherent oscillations over 20 ms; much longer than observed for a typical single photon transition (see text). (c) The measured Feshbach loss feature for $|\mathrm{bg}\rangle$ and $|\downarrow\rangle$ as well as the blue line shows a fit to a three-body loss process. The red curve shows the elastic change in a_{sc} due to the Feshbach resonance.

shaking, we read out the band populations using the band-map technique. The experimental signature of transfer out of the s-band into the p- and d-bands is shown in Fig. 5.6b.

Using the shaken lattice we can measure the excitation spectrum for a $s = 35E_r$ lattice as in Fig. 5.6c. We see here a clear two-photon excitation into the second excited band along with strong single photon transfer into the first excited band. The second order process can be suppressed by reducing the lattice depth (creating a more anharmonic spectrum) or the shaking amplitude L. Indeed we note, while a harmonic potential has a ladder of evenly spaced states, the transformation to an isolated two-level system is justified by the anharmonic nature of the lattice band spectrum. A single pair of bands can be isolated for $\Omega_n < \Delta_{\mathrm{gap}}(n = 0 \to 1) - \Delta_{\mathrm{gap}}(n = 1 \to 2)$[¶]. Driving for longer times we observe coherent dynamics over several ms. Coherent lattice band dynamics is plotted in Fig. 5.6d; Rabi oscillations between s- and p-bands are observed and some contamination in further excited bands is also seen.

While orbital spins are not sensitive to the magnetic field instabilities experienced here, their coherence lifetime still seems to be limited to ~ 2 ms. To elucidate the short coherence times of these oscillations, we consider the lifetime of atoms located in the first excited band of the lattice. To do so we quickly pulse the shaken lattice for $\tau = 0.3$ ms and allow the atoms to relax in the lattice potential. Typical observed relaxation data can be seen in

[¶]The detuning $\Delta_{\mathrm{gap}}(n = 0 \to 1) - \Delta_{\mathrm{gap}}(n = 1 \to 2)$ here becomes worse for deeper lattices as the harmonic approximation for a single lattice site is improved for deeply bound levels.

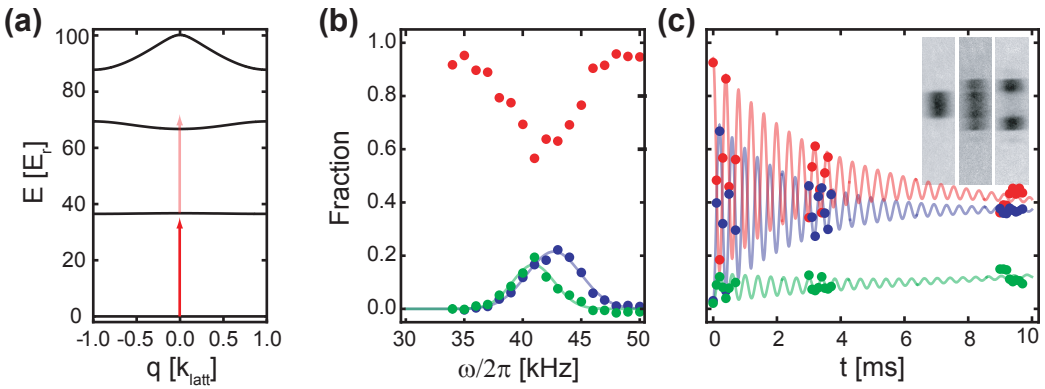

Figure 5.6: Coherent behavior in a phase modulated lattice. (a) Transition of interest illustrated in a $s = 30$ lattice. The two photon transition to the second excited band is off resonant even for modest s. (b) Spectroscopy of the bands. Population in the bands $n = 0, 1, 2$ are plotted in red, blue and green respectively. For the $35E_r$ lattice, the two photon transfer into the second band of the lattice represents a strong feature in the spectrum. The resonant features are consistent with band structure calculations. (c) Resonant driving of the $n = 0$ to $n = 1$ transition. We see several oscillations at a Rabi frequency of ∼kHz as well as damping over a 1.5 ms time scale. Solid lines represent fits to a decaying cosine with some offset, colors are the same as in (b). Inset shows raw TOF band map images for the first half period of oscillation. Clear transfer of most of the atoms into the first excited lattice band can be seen, with faint signal in higher bands. The maximal transfer is limited to $\sim 70\%$ of the total atom number.

Fig. 5.7. The number of atoms in the excited band experiences a rapid decay to a nonzero final value over ~ 10 ms.

The decay from the excited band is driven by collisional processes in the excited band like those illustrated in Fig. 5.7a [192, 193]. The most significant collisional decay channel consists of a collision between atoms in $n = 1$ band with the atoms relaxing into the $n = 0$ and $n = 2$ bands of the lattice. For sufficiently deep lattices, this band-changing collision is energetically allowed due to the near harmonic nature of the spectrum. However, collisions can only occur in lattices shallow enough to exhibit significant tunneling in the $n = 1$ band. We expect to observe a rapid decay of sites with $n_a > 1$, followed by a slow decay of singly-occupied sites. The initial decay to a steady state (steady up to at least 1 s) in a time slower than typical tunneling rates, suggesting that we eliminate multiple occupations before decay is eventually frozen out. Decay from an excited band can also occur for collisions between bands and

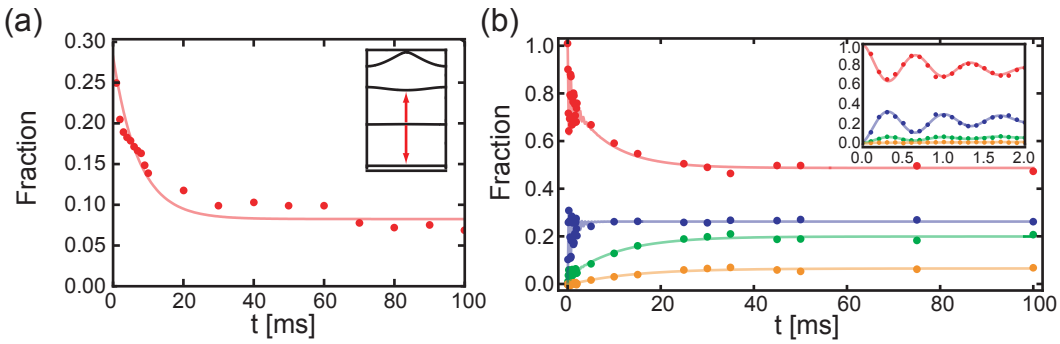

Figure 5.7: Coherence decay and the driven steady state. (a) Decay of the $n = 1$ excited state population. Line represents a fit to a decaying exponential with $1/e$ decay time of 8 ms. (Inset: collisional mechanism of decay from first excited band.) (b) Coherent dynamics for weakly driven, off-resonant transitions. Decay of coherence is observed similarly to that seen in Fig. 5.6c, while relaxation to a steady state is observed to occur on a timescale consistent with the band decay rate. Steady state populations in bands with $n = 2$ and $n = 3$ are significant. (Inset shows coherent behavior at short times.)

due to a superfluid bath [194].

To suppress transfer to a higher bands, we look at the coherent dynamics for blue detuned driving. We see for short times a similar coherence decay rate of ~ 2 ms. On a longer timescale, consistent with the band decay rate we see a relaxation to a steady state, including a significant population transfer into the $n = 2$ band. This observation is consistent with the collisional decay process described above. While the decay data do not demonstrate accumulation in the $n = 2$ band, this is to be expected as collisional decay for atoms in $n = 2$ can be very rapid in dense atomic clouds [192].

While the measured decay and decoherence rates are slow compared to the tunneling rates as predicted by [195]; we do not observe lifetimes consistent with those measured by early realizations of p-band lattice gases [193] (most likely due to an overly dense atomic sample increasing the collisional decay rates). Furthermore, we do not measure a significant change of the coherence decay rate over a wide range of parameters varying the shake amplitude and the total atom number. The persistent 400 Hz timescale could be due to inhomogeneous lattice potential or perhaps due to unstable differential light shifts in the lattice. The vibrational level pseudospin may be very practical if the lattice depth can be further stabilized and the density of spins reduced.[‖]

[‖]Amplitude modulation may be used to similar effect. This excitation couples only states separated by $\Delta n = 2$, and is thus further sensitive to tunneling effects and lattice

5.3.2 Differential interactions

Using the internal state spins requires using one of the three low-field Feshbach resonances described in [188]. These resonances allow, in principle, for the modulation of g_{ab} of up to 30%. Given that $\alpha \sim (g_{ab}/g_{bb} - 1)^2$, this precludes observation of the dissipative quantum phase transition, but it should allow for measurement of enhanced damping due to the superfluid bath. The calculated damping rate is given approximately by [63]

$$\Gamma \approx \sin\left(\frac{\pi\alpha}{2(1-\alpha)}\right)\Delta. \tag{5.16}$$

Away from the Feshbach resonance, $\alpha \sim (1.02 - 1)^2 = 4 \times 10^{-4}$ corresponds to a damping rate of $6 \times 10^{-4}\Delta$, which is prohibitively slow. However, for $g_{ab} = 1.3g_{aa}$, $\alpha \sim 0.1$ and the damping rate is $\sim 0.17\Delta$. For reasonable $\Delta \sim 2\pi \times 500$ Hz, this would require driving the spin for about 10 ms to see damping to a steady state of $P_e = 1/2$, a very realistic figure for our experiment considering the coherence times above.

Practical application of these resonances will be limited by the resonance widths ΔB. Theoretical elastic widths are on the order of $\Delta B \approx 1$ mG and inelastic widths $\gamma_B = 3$ mG. Comparing to a representative three-body loss measurement in Fig. 5.5c, we see that the measured elastic width is ~ 10 mG. Preliminary measurements suggest that this broadening is due to averaging over several ac-power line cycles during the loss measurement. We have recently succeeded in reducing these fluctuations to the $\sim 100\mu$G level [196], making use of the Feshbach resonance a realistic prospect.

In terms of driving, these reduced fluctuations would amount to a time varying detuning with amplitude 200 Hz for the occupational spin and 1 Hz for the clock transition. Together with the tuning of g_{ab}, this should indeed allow for the observation of phonon-induced damping of Rabi oscillations.

Compared to hyperfine state spins, orbital levels will not allow for tuning of the relative interaction strength. If we argue based on the relative size $\sqrt{\langle x^2\rangle^{(n=0)}/\langle x^2\rangle^{(n=1)}} = 1/\sqrt{3}$, we might suggest $\alpha \sim 0.17$ and a damping rate of $\sim 0.3\Delta$. Because of the rapid damping already observed for "bare" spins, it does not appear that this implementation could lead to immediate success.

depth instabilities. At present we are not yet able to observe even a single period of coherent oscillation using an amplitude modulated lattice.

5.4 Summary and outlook

The methods explored here are promising for the implementation of quantum dissipative models in our experimental setup. Coherence times and differential interaction strengths are of the correct order-of-magnitude to observe dissipative effects in the spin-boson model. However, to implement this model we require increased stability of the bias magnetic field, particularly against 60 Hz noise leaking into the setup from the wall power. Recent work has characterized this noise and the use of some compensating fields has allowed for significant coherence time improvements of a factor of three or more. These methods may be further improved by the use of active stabilization.

Recent work, in other groups, has focused on the interaction of a bath with a spin superposition state using a few of the pseudospins described above. Efforts have used the vibrational-level effective spin to investigate the decoherence and decay of a spin superposition due to interactions with a bosonic bath [64, 189]. The effects of a Fermi sea on mobile bosonic spins has also been studied and a loss of coherence of the $(|\uparrow\rangle + |\downarrow\rangle)/\sqrt{2}$ superpostion state due to quasiparticle scattering from the fermionic background has been observed [65]. However, these systems do not fully realize the spin-boson model as there is no active tunneling between $|\uparrow\rangle$ and $|\downarrow\rangle$ and in each case, scattering of free particle-like excitations of the reservoir dominate the dissipative effects. The experimental methods described here should allow for the extension of this experimental work into the regime of a driven spin coupled to a phonon bath.

Chapter 6

Conclusion

In this thesis, I have described two experiments investigating the dynamics of atomic matter waves in optical lattices. Further, I have detailed the experimental requirements and prospects for the implementation of effective spin-1/2 systems coupled to a superfluid bath. The first experiment reveals an interplay between disorder and interactions in the dynamics of a matter wave in a tilted optical lattice [125]. A reduction of disorder induced damping is observed due to the addition of mean field energy to the system, an effect that is maximized for comparable disorder and interaction strengths, and which can be explained through a screening argument. The second experiment investigates the dynamics of microwave induced diffraction of a superfluid from a state-dependent optical lattice [157]. The dynamics are interpreted in terms of the nonadiabatic dressed states, revealing diffractive behavior in an unfamiliar regime compared to typical atom diffraction experiments. This experiment establishes a technique for simple interferometric measurements. Furthermore, we propose the use of this diffraction scheme in a limit which probes the mean field excitations of the superfluid. In this limit, we suggest to use this scheme to realize an effective spin-1/2, along with other options in orbital and internal state spin models. The possibility of realizing the spin-boson model in an atomic system is discussed.

Current directions in the laboratory are working to improve the feasibility of experimentally realizing the spin-boson model and other dissipative phenomena. Much of the work has initially been in improving the field stability of the apparatus, with the dual purpose of improving the usefulness of rubidium's low-field Feshbach resonances and extending the coherent lifetime of driven microwave transitions.

These improvements, will allow for the investigation of dissipative models in optical lattices such as [63, 74, 194, 197]. The techniques established here could be used to investigate the concept of quantum parallelism in disordered

potentials [150]. Our system, capitalizing on state-dependent optical lattices, may be greatly enhanced by the stabilization of a Feshbach resonance, since this would potentially open up the possibilities to study in detail bosonic lattice polarons [123, 198, 199], perhaps extending the dynamical spin-boson model into the equilibrium setting. More general studies of impurity physics may also provide fruitful research directions [200–202].

Bibliography

[1] M. H. Anderson, J. R. Ensher, M. R. Matthews, C. E. Wieman, and E. A. Cornell. Observation of Bose-Einstein Condensation in a Dilute Atomic Vapor. *Science*, **269**, 198 (1995).

[2] K. B. Davis, M. O. Mewes, M. R. Andrews, N. J. van Druten, D. S. Durfee, D. M. Stamper-Kurn, and W. Ketterle. Bose-Einstein Condensation in a Gas of Sodium Atoms. *Phys. Rev. Lett.*, **75**, 3969 (1995).

[3] C. C. Bradley, C. A. Sackett, J. J. Tollett, and R. G. Hulet. Evidence of Bose-Einstein Condensation in an Atomic Gas with Attractive Interactions. *Phys. Rev. Lett.*, **75**, 1687 (1995).

[4] B. P. Anderson and M. A. Kasevich. Macroscopic Quantum Interference from Atomic Tunnel Arrays. *Science*, **282**, 1686 (1998).

[5] Y. B. Ovchinnikov, J. H. Müller, M. R. Doery, E. J. D. Vredenbregt, K. Helmerson, S. L. Rolston, and W. D. Phillips. Diffraction of a Released Bose-Einstein Condensate by a Pulsed Standing Light Wave. *Phys. Rev. Lett.*, **83**, 284 (1999).

[6] M. Kozuma, L. Deng, E. W. Hagley, J. Wen, R. Lutwak, K. Helmerson, S. L. Rolston, and W. D. Phillips. Coherent Splitting of Bose-Einstein Condensed Atoms with Optically Induced Bragg Diffraction. *Phys. Rev. Lett.*, **82**, 871 (1999).

[7] J. Stenger, S. Inouye, A. P. Chikkatur, D. M. Stamper-Kurn, D. E. Pritchard, and W. Ketterle. Bragg Spectroscopy of a Bose-Einstein Condensate. *Phys. Rev. Lett.*, **82**, 4569 (1999).

[8] E. W. Hagley, L. Deng, M. Kozuma, M. Trippenbach, Y. B. Band, M. Edwards, M. Doery, P. S. Julienne, K. Helmerson, S. L. Rolston, and W. D. Phillips. Measurement of the Coherence of a Bose-Einstein Condensate. *Phys. Rev. Lett.*, **83**, 3112 (1999).

[9] O. Morsch, J. Müller, M. Cristiani, D. Ciampini, and E. Arimondo. Bloch Oscillations and Mean-Field Effects of Bose-Einstein Condensates in 1D Optical Lattices. *Phys. Rev. Lett.*, **87** (2001).

[10] O. Morsch and M. Oberthaler. Dynamics of Bose-Einstein conensates in optical lattices. *Rev. Mod. Phys.*, **78**, 179 (2006).

[11] M. A. Cazalilla, R. Citro, T. Giamarchi, E. Orignac, and M. Rigol. One dimensional bosons: From condensed matter systems to ultracold gases. *Rev. Mod. Phys.*, **83**, 1405 (2011).

[12] M. Greiner, I. Bloch, O. Mandel, T. W. Hänsch, and T. Esslinger. Exploring Phase Coherence in a 2D Lattice of Bose-Einstein Condensates. *Phys. Rev. Lett.*, **87**, 160405 (2001).

[13] C. Orzel, A. K. Tuchman, M. L. Fenselau, M. Yasuda, and M. A. Kasevich. Squeezed States in a Bose-Einstein Condensate. *Science*, **291**, 2386 (2001).

[14] M. Greiner, O. Mandel, T. Esslinger, T. W. Hänsch, and I. Bloch. Quantum phase transition from a superfluid to a Mott insulator in a gas of ultracold atoms. *Nature*, **415**, 39 (2002).

[15] I. Bloch and W. Zwerger. Many-body physics with ultracold gases. *Rev. Mod. Phys.*, **80**, 885 (2008).

[16] M. Lewenstein, A. Sanpera, and V. Ahufinger. *Ultracold Atoms in Optical Lattices: Simulating Quantum Many-Body Systems*. Oxford University Press, Oxford (2012).

[17] P. Windpassinger and K. Sengstock. Engineering novel optical lattices. *Rep. Prog. Phys.*, **76**, 086401 (2013).

[18] O. Dutta, M. Gajda, P. Hauke, M. Lewenstein, D.-S. Lühmann, B. A. Malomed, T. Sowiński, and J. Zakrzewski. Non-standard Hubbard models in optical lattices: a review. *Rep. Prog. Phys.*, **78**, 066001 (2015).

[19] M. Köhl, H. Moritz, T. Stöferle, K. Günter, and T. Esslinger. Fermionic Atoms in a Three Dimensional Optical Lattice: Observing Fermi Surfaces, Dynamics, and Interactions. *Phys. Rev. Lett.*, **94**, 080403 (2005).

[20] R. Jordens, N. Strohmaier, K. Günter, H. Moritz, and T. Esslinger. A Mott insulator of fermionic atoms in an optical lattice. *Nature*, **455**, 204 (2008).

[21] M. Ölschläger, G. Wirth, and A. Hemmerich. Unconventional Superfluid Order in the F Band of a Bipartite Optical Square Lattice. *Phys. Rev. Lett.*, **106**, 015302 (2011).

[22] G. Wirth, M. Ölschläger, and A. Hemmerich. Evidence for orbital superfluidity in the P-band of a bipartite optical square lattice. *Nature Phys.*, **7**, 147 (2011).

[23] D. Greif, T. Uehlinger, G. Jotzu, L. Tarruell, and T. Esslinger. Short-Range Quantum Magnetism of Ultracold Fermions in an Optical Lattice. *Science*, **340**, 1307 (2013).

[24] R. A. Hart, P. M. Duarte, T.-L. Yang, X. Liu, T. Paiva, E. Khatami, R. T. Scalettar, N. Trivedi, D. A. Huse, and R. G. Hulet. Observation of antiferromagnetic correlations in the Hubbard model with ultracold atoms. *Nature*, **519**, 211 (2015).

[25] J. Struck, C. Ölschläger, R. Le Targat, P. Soltan-Panahi, A. Eckardt, M. Lewenstein, P. Windpassinger, and K. Sengstock. Quantum simulation of frustrated classical magnetism in triangular optical lattices. *Science*, **333**, 996 (2011).

[26] T. Uehlinger, G. Jotzu, M. Messer, D. Greif, W. Hofstetter, U. Bissbort, and T. Esslinger. Artificial Graphene with Tunable Interactions. *Phys. Rev. Lett.*, **111**, 185307 (2013).

[27] G. Jotzu, M. Messer, R. Desbuquois, M. Lebrat, T. Uehlinger, D. Greif, and T. Esslinger. Experimental realization of the topological Haldane model with ultracold fermions. *Nature*, **515**, 237 (2014).

[28] L. Duca, T. Li, M. Reitter, I. Bloch, M. Schleier-Smith, and U. Schneider. An Aharonov-Bohm interferometer for determining Bloch band topology. *Science*, **347**, 288 (2015).

[29] A. Zenesini, H. Lignier, D. Ciampini, O. Morsch, and E. Arimondo. Coherent Control of Dressed Matter Waves. *Phys. Rev. Lett.*, **102**, 100403 (2009).

[30] J. Dalibard, F. Gerbier, G. Juzeliūnas, and P. Öhberg. Colloquium: Artificial gauge potentials for neutral atoms. *Rev. Mod. Phys.*, **83**, 1523 (2011).

[31] J. Struck, C. Ölschläger, M. Weinberg, P. Hauke, J. Simonet, A. Eckardt, M. Lewenstein, K. Sengstock, and P. Windpassinger. Tunable Gauge

Potential for Neutral and Spinless Particles in Driven Optical Lattices. *Phys. Rev. Lett.*, **108** (2012).

[32] M. Aidelsburger, M. Lohse, C. Schweizer, M. Atala, J. T. Barreiro, S. Nascimbene, N. R. Cooper, I. Bloch, and N. Goldman. Measuring the Chern number of Hofstadter bands with ultracold bosonic atoms. *Nature Phys.*, **11**, 162 (2015).

[33] C. J. Kennedy, W. C. Burton, W. C. Chung, and W. Ketterle. Observation of Bose-Einstein Condensation in a Strong Synthetic Magnetic Field. *arXiv:1503.08243* (2015).

[34] C. V. Parker, L.-C. Ha, and C. Chin. Direct observation of effective ferromagnetic domains of cold atoms in a shaken optical lattice. *Nature Phys.*, **9**, 769 (2013).

[35] M. A. Khamehchi, Y. Zhang, C. Hamner, T. Busch, and P. Engels. Measurement of collective excitations in a spin-orbit-coupled Bose-Einstein condensate. *Phys. Rev. A*, **90**, 063624 (2014).

[36] L.-C. Ha, L. W. Clark, C. V. Parker, B. M. Anderson, and C. Chin. Roton-Maxon Excitation Spectrum of Bose Condensates in a Shaken Optical Lattice. *Phys. Rev. Lett.*, **114**, 055301 (2015).

[37] W. S. Bakr, A. Peng, M. E. Tai, R. Ma, J. Simon, J. I. Gillen, S. Fölling, L. Pollet, and M. Greiner. Probing the SuperfluidtoMott Insulator Transition at the Single-Atom Level. *Science*, **329**, 547 (2010).

[38] M. Endres, M. Cheneau, T. Fukuhara, C. Weitenberg, P. Schauß, C. Gross, L. Mazza, M. C. Bañuls, L. Pollet, I. Bloch, and S. Kuhr. Observation of Correlated Particle-Hole Pairs and String Order in Low-Dimensional Mott Insulators. *Science*, **334**, 200 (2011).

[39] P. M. Preiss, R. Ma, M. E. Tai, A. Lukin, M. Rispoli, P. Zupancic, Y. Lahini, R. Islam, and M. Greiner. Strongly correlated quantum walks in optical lattices. *Science*, **347**, 1229 (2015).

[40] L. W. Cheuk, M. A. Nichols, M. Okan, T. Gersdorf, V. V. Ramasesh, W. S. Bakr, T. Lompe, and M. W. Zwierlein. Quantum-Gas Microscope for Fermionic Atoms. *Phys. Rev. Lett.*, **114**, 193001 (2015).

[41] E. Haller, J. Hudson, A. Kelly, D. A. Cotta, B. Peaudecerf, G. D. Bruce, and S. Kuhr. Single-atom imaging of fermions in a quantum-gas microscope. *arXiv:1503.02005* (2015).

[42] M. Miranda, R. Inoue, Y. Okuyama, A. Nakamoto, and M. Kozuma. Site-resolved imaging of ytterbium atoms in a two-dimensional optical lattice. *Phys. Rev. A*, **91**, 063414 (2015).

[43] N. Hinkley, J. A. Sherman, N. B. Phillips, M. Schioppo, N. D. Lemke, K. Beloy, M. Pizzocaro, C. W. Oates, and A. D. Ludlow. An Atomic Clock with 10^{-18} Instability. *Science*, **341**, 1215 (2013).

[44] M. J. Martin, M. Bishof, M. D. Swallows, X. Zhang, C. Benko, J. von Stecher, A. V. Gorshkov, A. M. Rey, and J. Ye. A Quantum Many-Body Spin System in an Optical Lattice Clock. *Science*, **341**, 632 (2013).

[45] B. J. Bloom, T. L. Nicholson, J. R. Williams, S. L. Campbell, M. Bishof, X. Zhang, W. Zhang, S. L. Bromley, and J. Ye. An optical lattice clock with accuracy and stability at the 10^{-18} level. *Nature*, **506**, 71 (2014).

[46] M. McDonald, B. H. McGuyer, G. Z. Iwata, and T. Zelevinsky. Thermometry via Light Shifts in Optical Lattices. *Phys. Rev. Lett.*, **114**, 023001 (2015).

[47] J. Billy, V. Josse, Z. Zuo, A. Bernard, B. Hambrecht, P. Lugan, D. Clement, L. Sanchez-Palencia, P. Bouyer, and A. Aspect. Direct observation of Anderson localization of matter waves in a controlled disorder. *Nature*, **453**, 891 (2008).

[48] M. White, M. Pasienski, D. McKay, S. Q. Zhou, D. Ceperley, and B. DeMarco. Strongly Interacting Bosons in a Disordered Optical Lattice. *Phys. Rev. Lett.*, **102**, 055301 (2009).

[49] S. Krinner, D. Stadler, J. Meineke, J.-P. Brantut, and T. Esslinger. Superfluidity with disorder in a thin film of quantum gas. *Phys. Rev. Lett.*, **110**, 100601 (2013).

[50] J. Lye, L. Fallani, C. Fort, V. Guarrera, M. Modugno, D. Wiersma, and M. Inguscio. Effect of interactions on the localization of a Bose-Einstein condensate in a quasiperiodic lattice. *Phys. Rev. A*, **75**, 061603 (2007).

[51] G. Roati, C. D'Errico, L. Fallani, M. Fattori, C. Fort, M. Zaccanti, G. Modugno, M. Modugno, and M. Inguscio. Anderson localization of a non-interacting Bose-Einstein condensate. *Nature*, **453**, 895 (2008).

[52] M. Schreiber, S. S. Hodgman, P. Bordia, H. P. Lüschen, M. H. Fischer, R. Vosk, E. Altman, U. Schneider, and I. Bloch. Observation of many-body localization of interacting fermions in a quasi-random optical lattice. *arXiv:1501.05661* (2015).

[53] U. Gavish and Y. Castin. Matter-Wave Localization in Disordered Cold Atom Lattices. *Phys. Rev. Lett.*, **95** (2005).

[54] B. Gadway, D. Pertot, J. Reeves, M. Vogt, and D. Schneble. Glassy Behavior in a Binary Atomic Mixture. *Phys. Rev. Lett.*, **107**, 145306 (2011).

[55] M. P. A. Fisher, P. B. Weichman, G. Grinstein, and D. S. Fisher. Boson localization and the superfluid-insulator transition. *Phys. Rev. B*, **40**, 546 (1989).

[56] L. Tanzi, E. Lucioni, S. Chaudhuri, L. Gori, A. Kumar, C. D'Errico, M. Inguscio, and G. Modugno. Transport of a Bose Gas in 1D Disordered Lattices at the Fluid-Insulator Transition. *Phys. Rev. Lett.*, **111**, 115301 (2013).

[57] P. W. Anderson. Absence of Diffusion in Certain Random Lattices. *Phys. Rev.*, **109**, 1492 (1958).

[58] S. S. Kondov, W. R. McGehee, J. J. Zirbel, and B. DeMarco. Three-Dimensional Anderson Localization of Ultracold Matter. *Science*, **334**, 66 (2011).

[59] F. Jendrzejewski, A. Bernard, K. Muller, P. Cheinet, V. Josse, M. Piraud, L. Pezze, L. Sanchez-Palencia, A. Aspect, and P. Bouyer. Three-dimensional localization of ultracold atoms in an optical disordered potential. *Nature Phys.*, **8**, 398 (2012).

[60] T. Giamarchi and H. J. Schulz. Anderson localization and interactions in one-dimensional metals. *Phys. Rev. B*, **37**, 325 (1988).

[61] R. Scalettar, G. Batrouni, and G. Zimanyi. Localization in interacting, disordered, Bose systems. *Phys. Rev. Lett.*, **66**, 3144 (1991).

[62] B. Deissler, M. Zaccanti, G. Roati, C. D'Errico, M. Fattori, M. Modugno, G. Modugno, and M. Inguscio. Delocalization of a disordered bosonic system by repulsive interactions. *Nature Phys.*, **6**, 354 (2010).

[63] A. Recati, P. O. Fedichev, W. Zwerger, J. von Delft, and P. Zoller. Atomic Quantum Dots Coupled to a Reservoir of a Superfluid Bose-Einstein Condensate. *Phys. Rev. Lett.*, **94**, 040404 (2005).

[64] R. Scelle, T. Rentrop, A. Trautmann, T. Schuster, and M. K. Oberthaler. Motional Coherence of Fermions Immersed in a Bose Gas. *Phys. Rev. Lett.*, **111**, 070401 (2013).

[65] M. Cetina, M. Jag, R. S. Lous, J. T. M. Walraven, R. Grimm, R. S. Christensen, and G. M. Bruun. Decoherence of Impurities in a Fermi Sea of Ultracold Atoms. *arXiv:1505.00738* (2015).

[66] S. Drenkelforth, G. Kleine Büning, J. Will, T. Schulte, N. Murray, W. Ertmer, L. Santos, and J. J. Arlt. Damped Bloch oscillations of BoseEinstein condensates in disordered potential gradients. *New J. Phys.*, **10**, 045027 (2008).

[67] M. Gustavsson, E. Haller, M. Mark, J. Danzl, G. Rojas-Kopeinig, and H. C. Nägerl. Control of Interaction-Induced Dephasing of Bloch Oscillations. *Phys. Rev. Lett.*, **100**, 080404 (2008).

[68] M. Y. Azbel. Charged bosons in a random potential. *Phys. Lett. A*, **77**, 347 (1980).

[69] J. D. Reppy. Superfluid helium in porous media. *J. Low Temp. Phys.*, **87**, 205 (1992).

[70] A. D. Cronin, J. Schmiedmayer, and D. E. Pritchard. Optics and interferometry with atoms and molecules. *Rev. Mod. Phys.*, **81**, 1051 (2009).

[71] P. L. Gould, G. A. Ruff, and D. E. Pritchard. Diffraction of atoms by light: The near-resonant Kapitza-Dirac effect. *Phys. Rev. Lett.*, **56**, 827 (1986).

[72] P. J. Martin, B. G. Oldaker, A. H. Miklich, and D. E. Pritchard. Bragg scattering of atoms from a standing light wave. *Phys. Rev. Lett.*, **60**, 515 (1988).

[73] T. Sleator, T. Pfau, V. Balykin, O. Carnal, and J. Mlynek. Experimental demonstration of the optical Stern-Gerlach effect. *Phys. Rev. Lett.*, **68**, 1996 (1992).

[74] P. P. Orth, I. Stanic, and K. Le Hur. Dissipative quantum Ising model in a cold-atom spin-boson mixture. *Phys. Rev. A*, **77**, 051601 (2008).

[75] A. J. Leggett, S. Chakravarty, A. T. Dorsey, M. P. A. Fisher, A. Garg, and W. Zwerger. Dynamics of the dissipative two-state system. *Rev. Mod. Phys.*, **59**, 1 (1987).

[76] W. Ketterle, D. S. Durfee, and D. M. Stamper-Kurn. Making, probing and understanding Bose-Einstein condensates. *arXiv:9904034* (1999).

[77] F. Dalfovo, S. Giorgini, L. P. Pitaevskii, and S. Stringari. Theory of Bose-Einstein condensation in trapped gases. *Rev. Mod. Phys.*, **71**, 463 (1999).

[78] A. J. Leggett. Bose-Einstein condensation in the alkali gases: Some fundamental concepts. *Rev. Mod. Phys.*, **73**, 307 (2001).

[79] C. J. Pethick and H. Smith. *Bose-Einstein Condensation in Dilute Gases*. Cambridge University Press, Cambridge, 2nd edition (2008).

[80] M. Weidemüller and C. Zimmermann, eds. *Cold Atoms and Molecules*. Wiley-VCH, Weinheim (2009).

[81] F. London. The-phenomenon of liquid helium and the Bose-Einstein degeneracy. *Nature*, **141**, 643 (1938).

[82] B. C. Crooker, B. Hebral, E. N. Smith, Y. Takano, and J. D. Reppy. Superfluidity in a Dilute Bose Gas. *Phys. Rev. Lett.*, **51**, 666 (1983).

[83] W. Ketterle. Nobel lecture: When atoms behave as waves: Bose-Einstein condensation and the atom laser. *Rev. Mod. Phys.*, **74**, 1131 (2002).

[84] A. Leggett and S. Zhang. *The BEC-BCS Crossover: Some History and Some General Observations*, 33–47. Springer (2012).

[85] H. Deng, H. Haug, and Y. Yamamoto. Exciton-polariton Bose-Einstein condensation. *Rev. Mod. Phys.*, **82**, 1489 (2010).

[86] J. Klaers, J. Schmitt, F. Vewinger, and M. Weitz. Bose-Einstein condensation of photons in an optical microcavity. *Nature*, **468**, 545 (2010).

[87] B. Gadway. Matter-Wave Dynamics in Tailored Optical and Atomic Lattices. Phd thesis, Stony Brook University (2012).

[88] O. M. Maragò, S. A. Hopkins, J. Arlt, E. Hodby, G. Hechenblaikner, and C. J. Foot. Observation of the Scissors Mode and Evidence for Superfluidity of a Trapped Bose-Einstein Condensed Gas. *Phys. Rev. Lett.*, **84**, 2056 (2000).

[89] D. Pertot, D. Greif, S. Albert, B. Gadway, and D. Schneble. Versatile transporter apparatus for experiments with optically trapped Bose-Einstein condensates. *J. Phys. B: At., Mol. Opt. Phys.*, **42**, 215305 (2009).

[90] D. Greif. Evaorative Cooling and Bose-Einstein Condensation of Rb-87 in a moving coil TOP trap geometry. Masters thesis, Stony Book University (2007).

[91] D. Pertot. Two-Component Bosons in State-Dependent Optical Lattices. Phd thesis, Stony Brook University (2011).

[92] E. L. Raab, M. Prentiss, A. Cable, S. Chu, and D. E. Pritchard. Trapping of Neutral Sodium Atoms with Radiation Pressure. *Phys. Rev. Lett.*, **59**, 2631 (1987).

[93] H. J. Metcalf and P. van der Straten. *Lasr Cooling and Trapping.* Springer, New York (1999).

[94] J. Dalibard and C. Cohen-Tannoudji. Dressed-atom approach to atomic motion in laser light: the dipole force revisited. *J. Opt. Soc. Am. B*, **2**, 1707 (1985).

[95] J. Dalibard and C. Cohen-Tannoudji. Laser cooling below the Doppler limit by polarization gradients: simple theoretical models. *J. Opt. Soc. Am. B*, **6**, 2023 (1989).

[96] W. Ketterle and N. J. V. Druten. Evaporative Cooling of Trapped Atoms. *Adv. At., Mol., Opt. Phys.*, **37**, 181 (1996).

[97] R. Grimm, M. Weidemüller, and Y. B. Ovchinnikov. Optical Dipole Traps for Neutral Atoms. *Adv. At., Mol., Opt. Phys.*, **42**, 95 (2000).

[98] D. Steck. Rubidium 87 D Line Data (2010). Available online at http://steck.us/alkalidata (revision 2.1.4, 23 December 2010).

[99] I. H. Deutsch and P. S. Jessen. Quantum-state control in optical lattices. *Phys. Rev. A*, **57**, 1972 (1998).

[100] L. LeBlanc and J. Thywissen. Species-specific optical lattices. *Phys. Rev. A*, **75** (2007).

[101] F. Gerbier, A. Widera, S. Fölling, O. Mandel, and I. Bloch. Resonant control of spin dynamics in ultracold quantum gases by microwave dressing. *Phys. Rev. A*, **73**, 041602 (2006).

[102] L. Zhao, J. Jiang, T. Tang, M. Webb, and Y. Liu. Dynamics in spinor condensates tuned by a microwave dressing field. *Phys. Rev. A*, **89**, 023608 (2014).

[103] D. M. Stamper-Kurn and M. Ueda. Spinor Bose gases: Symmetries, magnetism, and quantum dynamics. *Rev. Mod. Phys.*, **85**, 1191 (2013).

[104] I. Bloch. Ultracold quantum gases in optical lattices. *Nature Phys.*, **1**, 23 (2005).

[105] N. W. Ashcroft and N. Mermin. *Solid State Physics*. Thomson Learning, Toronto (1976).

[106] D. Jaksch. Bose-Einstein Condensation and Applications. Phd thesis, Leopold-Franzens-Universität Innsbruck (1999).

[107] G. H. Wannier. Wave Functions and Effective Hamiltonian for Bloch Electrons in an Electric Field. *Phys. Rev.*, **117**, 432 (1960).

[108] N. Marzari and D. Vanderbilt. Maximally localized generalized Wannier functions for composite energy bands. *Phys. Rev. B*, **56**, 12847 (1997).

[109] C. Zener. A Theory of the Electrical Breakdown of Solid Dielectrics. *Proc. R. Soc. Lond. A*, **145**, 523 (1934).

[110] J. R. Rubbmark, M. M. Kash, M. G. Littman, and D. Kleppner. Dynamical effects at avoided level crossings: A study of the Landau-Zener effect using Rydberg atoms. *Phys. Rev. A*, **23**, 3107 (1981).

[111] E. Peik, M. B. Dahan, I. Bouchoule, Y. Castin, and C. Salomon. Bloch oscillations of atoms, adiabatic rapid passage, and monokinetic atom beams. *Phys. Rev. A*, **55**, 2989 (1997).

[112] D. Choi and Q. Niu. Bose-Einstein Condensates in an Optical Lattice. *Phys. Rev. Lett.*, **82**, 2022 (1999).

[113] B. Wu and Q. Niu. Nonlinear Landau-Zener tunneling. *Phys. Rev. A*, **61**, 023402 (2000).

[114] M. Machholm, C. J. Pethick, and H. Smith. Band structure, elementary excitations, and stability of a Bose-Einstein condensate in a periodic potential. *Phys. Rev. A*, **67**, 053613 (2003).

[115] L. Fallani, L. De Sarlo, J. Lye, M. Modugno, R. Saers, C. Fort, and M. Inguscio. Observation of Dynamical Instability for a Bose-Einstein Condensate in a Moving 1D Optical Lattice. *Phys. Rev. Lett.*, **93** (2004).

[116] D. Jaksch, C. Bruder, J. I. Cirac, C. W. Gardiner, and P. Zoller. Cold Bosonic Atoms in Optical Lattices. *Phys. Rev. Lett.*, **81**, 4 (1998).

[117] H. Miyake, G. A. Siviloglou, C. J. Kennedy, W. C. Burton, and W. Ketterle. Realizing the Harper Hamiltonian with Laser-Assisted Tunneling in Optical Lattices. *Phys. Rev. Lett.*, **111**, 185302 (2013).

[118] J. H. Denschlag, J. E. Simsarian, H. Häffner, C. McKenzie, A. Browaeys, D. Cho, K. Helmerson, S. L. Rolston, and W. D. Phillips. A Bose-Einstein condensate in an optical lattice. *J. Phys. B: At., Mol. Opt. Phys.*, **35**, 3095 (2002).

[119] T. Gericke, F. Gerbier, A. Widera, S. Fölling, O. Mandel, and I. Bloch. Adiabatic loading of a Bose-Einstein condensate in a 3D optical lattice. *J. Mod. Opt.*, **54**, 735 (2007).

[120] E. Edwards, M. Beeler, T. Hong, and S. Rolston. Adiabaticity and Localization in One-Dimensional Incommensurate Lattices. *Phys. Rev. Lett.*, **101**, 260402 (2008).

[121] S. S. Natu, D. C. McKay, B. DeMarco, and E. J. Mueller. Evolution of condensate fraction during rapid lattice ramps. *Phys. Rev. A*, **85**, 061601 (2012).

[122] S. Li, S. R. Manmana, A. M. Rey, R. Hipolito, A. Reinhard, J.-F. Riou, L. A. Zundel, and D. S. Weiss. Self-trapping dynamics in a two-dimensional optical lattice. *Phys. Rev. A*, **88**, 023419 (2013).

[123] B. Gadway, D. Pertot, R. Reimann, and D. Schneble. Superfluidity of Interacting Bosonic Mixtures in Optical Lattices. *Phys. Rev. Lett.*, **105**, 045303 (2010).

[124] B. Gadway, D. Pertot, R. Reimann, M. G. Cohen, and D. Schneble. Analysis of Kapitza-Dirac diffraction patterns beyond the Raman-Nath regime. *Opt. Express*, **17**, 19173 (2009).

[125] J. B. Reeves, B. Gadway, T. Bergeman, I. Danshita, and D. Schneble. Superfluid Bloch dynamics in an incommensurate optical lattice. *New J. Phys.*, **16**, 065011 (2014).

[126] J. Hubbard. Electron Correlations in Narrow Energy Bands. *Proc. R. Soc. Lond. A*, **276**, 238 (1963).

[127] P. A. Crowell, F. W. Van Keuls, and J. D. Reppy. Onset of superfluidity in ^{4}He films adsorbed on disordered substrates. *Phys. Rev. B*, **55**, 12620 (1997).

[128] B. I. Shklovskii. Simple model of Coulomb disorder and screening in graphene. *Phys. Rev. B*, **76**, 224511 (2007).

[129] J. Lye, L. Fallani, M. Modugno, D. Wiersma, C. Fort, and M. Inguscio. Bose-Einstein Condensate in a Random Potential. *Phys. Rev. Lett.*, **95**, 070401 (2005).

[130] S. S. Kondov, W. R. McGehee, W. Xu, and B. DeMarco. Disorder-Induced Localization in a Strongly Correlated Atomic Hubbard Gas. *Phys. Rev. Lett.*, **114**, 083002 (2015).

[131] L. Fallani, J. E. Lye, V. Guarrera, C. Fort, and M. Inguscio. Ultracold Atoms in a Disordered Crystal of Light: Towards a Bose Glass. *Phys. Rev. Lett.*, **98**, 130404 (2007).

[132] D. M. Basko, I. L. Aleiner, and B. L. Altshuler. Metalinsulator transition in a weakly interacting many-electron system with localized single-particle states. *Ann. Phys.*, **321**, 1126 (2006).

[133] J. Eisert, M. Friesdorf, and C. Gogolin. Quantum many-body systems out of equilibrium. *Nature Phys.*, **11**, 124 (2015).

[134] F. Bloch. Über die Quantenmechanik der Elektronen in Kristallgittern. *Z. Phys. A*, **52**, 555 (1929).

[135] L. Esaki and R. Tsu. Superlattice and Negative Differential Conductivity in Semiconductors. *IBM J. Res. Dev.*, **14**, 61 (1970).

[136] C. Waschke, H. Roskos, R. Schwedler, K. Leo, H. Kurz, and K. Köhler. Coherent submillimeter-wave emission from Bloch oscillations in a semiconductor superlattice. *Phys. Rev. Lett.*, **70**, 3319 (1993).

[137] M. Ben Dahan, E. Peik, J. Reichel, Y. Castin, and C. Salomon. Bloch Oscillations of Atoms in an Optical Potential. *Phys. Rev. Lett.*, **76**, 4508 (1996).

[138] G. Roati, E. de Mirandes, F. Ferlaino, H. Ott, G. Modugno, and M. Inguscio. Atom Interferometry with Trapped Fermi Gases. *Phys. Rev. Lett.*, **92**, 230402 (2004).

[139] M. Fattori, C. D'Errico, G. Roati, M. Zaccanti, M. Jona-Lasinio, M. Modugno, M. Inguscio, and G. Modugno. Atom Interferometry with a Weakly Interacting Bose-Einstein Condensate. *Phys. Rev. Lett.*, **100**, 080405 (2008).

[140] D. Witthaut, M. Werder, S. Mossmann, and H. Korsch. Bloch oscillations of Bose-Einstein condensates: Breakdown and revival. *Phys. Rev. E*, **71**, 036625 (2005).

[141] A. Kolovsky, H. Korsch, and E.-M. Graefe. Bloch oscillations of Bose-Einstein condensates: Quantum counterpart of dynamical instability. *Phys. Rev. A*, **80**, 023617 (2009).

[142] A. Buchleitner and A. Kolovsky. Interaction-Induced Decoherence of Atomic Bloch Oscillations. *Phys. Rev. Lett.*, **91**, 253002 (2003).

[143] A. R. Kolovsky and A. Buchleitner. Floquet-Bloch operator for the Bose-Hubbard model with static field. *Phys. Rev. E*, **68**, 056213 (2003).

[144] F. Meinert, M. J. Mark, E. Kirilov, K. Lauber, P. Weinmann, M. Grbner, and H. C. Nägerl. Interaction-Induced Quantum Phase Revivals and Evidence for the Transition to the Quantum Chaotic Regime in 1D Atomic Bloch Oscillations. *Phys. Rev. Lett.*, **112**, 193003 (2014).

[145] T. Schulte, S. Drenkelforth, G. Büning, W. Ertmer, J. Arlt, M. Lewenstein, and L. Santos. Dynamics of Bloch oscillations in disordered lattice potentials. *Phys. Rev. A*, **77**, 023610 (2008).

[146] S. Walter, D. Schneble, and A. C. Durst. Bloch oscillations in lattice potentials with controlled aperiodicity. *Phys. Rev. A*, **81**, 033623 (2010).

[147] A. Görlitz, T. Kinoshita, T. W. Hänsch, and A. Hemmerich. Realization of bichromatic optical superlattices. *Phys. Rev. A*, **64**, 011401 (2001).

[148] D. Levine and P. J. Steinhardt. Quasicrystals: A New Class of Ordered Structures. *Phys. Rev. Lett.*, **53**, 2477 (1984).

[149] D. Clément, A. F. Varn, J. A. Retter, L. Sanchez-Palencia, A. Aspect, and P. Bouyer. Experimental study of the transport of coherent interacting matter-waves in a 1D random potential induced by laser speckle. *New J. Phys.*, **8**, 165 (2006).

[150] B. Paredes, F. Verstraete, and J. I. Cirac. Exploiting Quantum Parallelism to Simulate Quantum Random Many-Body Systems. *Phys. Rev. Lett.*, **95**, 140501 (2005).

[151] R. B. Diener, G. A. Georgakis, J. Zhong, M. Raizen, and Q. Niu. Transition between extended and localized states in a one-dimensional incommensurate optical lattice. *Phys. Rev. A*, **64**, 033416 (2001).

[152] P. G. Harper. The General Motion of Conduction Electrons in a Uniform Magnetic Field, with Application to the Diamagnetism of Metals. *Proc. Phys. Soc., London, Sect. A*, **68**, 879 (1955).

[153] S. Aubry and G. André. Analyticity breaking and Anderson localization in incommensurate lattices. *Ann. Israel Phys. Soc*, **3**, 18 (1980).

[154] G. L. Ingold, A. Wobst, C. Aulbach, and P. Hänggi. Delocalization and Heisenberg's uncertainty relation. *Eur. Phys. J. B*, **30**, 175 (2002).

[155] M. Modugno. Exponential localization in one-dimensional quasi-periodic optical lattices. *New J. Phys.*, **11**, 033023 (2009).

[156] T. Bergeman. Private Communication.

[157] J. Reeves, L. Krinner, M. Stewart, A. Pazmio, and D. Schneble. Nonadiabatic Diffraction of Matter Waves. *arXiv:1505.06085* (2015). (accepted in Phys. Rev. A.).

[158] W. H. Bragg and W. L. Bragg. The Reflection of X-rays by Crystals. *Proc. R. Soc. Lond. A*, **88**, 428 (1913).

[159] M. Laue. Kritische Bemerkungen zu den Deutungen der Photogramme von Friedrich und Knipping. *Physik. Z.*, **14**, 421 (1913).

[160] C. Davisson and L. H. Germer. The Scattering of Electrons by a Single Crystal of Nickel. *Nature*, **119**, 558 (1927).

[161] P. Meystre. *Atom Optics*. Springer, New York (2001).

[162] P. L. Kapitza and P. A. M. Dirac. The reflection of electrons from standing light waves. *Math. Proc. Cambridge*, **29**, 297 (1933).

[163] D. L. Freimund, K. Aflatooni, and H. Batelaan. Observation of the Kapitza-Dirac effect. *Nature*, **413**, 142 (2001).

[164] O. Zobay and B. M. Garraway. Two-Dimensional Trapping in Field-Induced Adiabatic Potentials. *Phys. Rev. Lett.*, **86**, 1195 (2001).

[165] Y. Colombe, E. Knyazchyan, O. Morizot, B. Mercier, V. Lorent, and H. Perrin. Ultracold atoms confined in rf-induced two-dimensional trapping potentials. *Europhys. Lett.*, **67**, 593 (2004).

[166] C. Cohen-Tannoudji, J. Dupont-Roc, and G. Grynberg. *Atom Photon Interactions*. Wiley-VCH, Weinheim (2004).

[167] I. Lesanovsky, T. Schumm, S. Hofferberth, L. M. Andersson, P. Krüger, and J. Schmiedmayer. Adiabatic radio-frequency potentials for the coherent manipulation of matter waves. *Phys. Rev. A*, **73**, 033619 (2006).

[168] M. White, H. Gao, M. Pasienski, and B. DeMarco. Bose-Einstein condensates in rf-dressed adiabatic potentials. *Phys. Rev. A*, **74**, 023616 (2006).

[169] S. Hofferberth, I. Lesanovsky, B. Fischer, J. Verdu, and J. Schmiedmayer. Radiofrequency-dressed-state potentials for neutral atoms. *Nature Phys.*, **2**, 710 (2006).

[170] N. Lundblad, P. J. Lee, I. B. Spielman, B. L. Brown, W. D. Phillips, and J. V. Porto. Atoms in a Radio-Frequency-Dressed Optical Lattice. *Phys. Rev. Lett.*, **100**, 150401 (2008).

[171] Y. J. Lin, R. L. Compton, K. Jimenez-Garcia, J. V. Porto, and I. B. Spielman. Synthetic magnetic fields for ultracold neutral atoms. *Nature*, **462**, 628 (2009).

[172] W. Yi, A. J. Daley, G. Pupillo, and P. Zoller. State-dependent, addressable subwavelength lattices with cold atoms. *New J. Phys.*, **10**, 073015 (2008).

[173] N. Lundblad, S. Ansari, Y. Guo, and E. Moan. Observations of $\lambda/4$ structure in a low-loss radio-frequency-dressed optical lattice. *Phys. Rev. A*, **90**, 053612 (2014).

[174] D. Pertot, B. Gadway, and D. Schneble. Collinear Four-Wave Mixing of Two-Component Matter Waves. *Phys. Rev. Lett.*, **104**, 200402 (2010).

[175] B. Gadway, D. Pertot, J. Reeves, and D. Schneble. Probing an ultracold-atom crystal with matter waves. *Nature Phys.*, **8**, 544 (2012).

[176] P. Pedri, L. Pitaevskii, S. Stringari, C. Fort, S. Burger, F. S. Cataliotti, P. Maddaloni, F. Minardi, and M. Inguscio. Expansion of a Coherent Array of Bose-Einstein Condensates. *Phys. Rev. Lett.*, **87**, 220401 (2001).

[177] S. Gupta, K. Dieckmann, Z. Hadzibabic, and D. E. Pritchard. Contrast Interferometry using Bose-Einstein Condensates to Measure h/m and α. *Phys. Rev. Lett.*, **89**, 140401 (2002).

[178] G. K. Campbell, A. E. Leanhardt, J. Mun, M. Boyd, E. W. Streed, W. Ketterle, and D. E. Pritchard. Photon Recoil Momentum in Dispersive Media. *Phys. Rev. Lett.*, **94**, 170403 (2005).

[179] M. Abad and A. Recati. A study of coherently coupled two-component Bose-Einstein condensates. *Eur. Phys. J. D*, **67**, 1 (2013).

[180] F. Meinert, M. J. Mark, E. Kirilov, K. Lauber, P. Weinmann, A. J. Daley, and H. C. Nägerl. Quantum Quench in an Atomic One-Dimensional Ising Chain. *Phys. Rev. Lett.*, **111**, 053003 (2013).

[181] M. A. Khamehchi, C. Qu, M. E. Mossman, C. Zhang, and P. Engels. Spin-momentum coupled Bose-Einstein condensates with lattice band pseudospins. *arXiv:1506.03887* (2015).

[182] D. Chen, C. Meldgin, P. Russ, E. Mueller, and B. DeMarco. Quasi-momentum Cooling and Relaxation in a Strongly Correlated Optical Lattice. *arXiv:1503.07606* (2015).

[183] U. Weiss. *Quantum Dissipative Systems*. World Scientific, Hackensack, 3$^{\text{rd}}$ edition (2008).

[184] P. Orth. Dissipative dynamics and novel quantum phases in strongly correlated cold-atom mixtures. Phd thesis, Yale University (2011).

[185] N. Schlosser, G. Reymond, and P. Grangier. Collisional Blockade in Microscopic Optical Dipole Traps. *Phys. Rev. Lett.*, **89**, 023005 (2002).

[186] T. Grunzweig, A. Hilliard, M. McGovern, and M. F. Andersen. Near-deterministic preparation of a single atom in an optical microtrap. *Nature Phys.*, **6**, 951 (2010).

[187] W. S. Bakr, P. M. Preiss, M. E. Tai, R. Ma, J. Simon, and M. Greiner. Orbital excitation blockade and algorithmic cooling in quantum gases. *Nature*, **480**, 500 (2011).

[188] A. Kaufman, R. Anderson, T. Hanna, E. Tiesinga, P. Julienne, and D. Hall. Radio-frequency dressing of multiple Feshbach resonances. *Phys. Rev. A*, **80** (2009).

[189] D. Chen, C. Meldgin, and B. DeMarco. Bath-induced band decay of a Hubbard lattice gas. *Phys. Rev. A*, **90**, 013602 (2014).

[190] K. W. Madison, M. C. Fischer, R. B. Diener, Q. Niu, and M. G. Raizen. Dynamical Bloch Band Suppression in an Optical Lattice. *Phys. Rev. Lett.*, **81**, 5093 (1998).

[191] S. Arlinghaus and M. Holthaus. Driven optical lattices as strong-field simulators. *Phys. Rev. A*, **81**, 063612 (2010).

[192] I. B. Spielman, P. R. Johnson, J. H. Huckans, C. D. Fertig, S. L. Rolston, W. D. Phillips, and J. V. Porto. Collisional deexcitation in a quasi-two-dimensional degenerate bosonic gas. *Phys. Rev. A*, **73**, 020702 (2006).

[193] T. Müller, S. Fölling, A. Widera, and I. Bloch. State Preparation and Dynamics of Ultracold Atoms in Higher Lattice Orbitals. *Phys. Rev. Lett.*, **99**, 200405 (2007).

[194] A. J. Daley, P. O. Fedichev, and P. Zoller. Single-atom cooling by superfluid immersion: A nondestructive method for qubits. *Phys. Rev. A*, **69**, 022306 (2004).

[195] A. Isacsson and S. M. Girvin. Multiflavor bosonic Hubbard models in the first excited Bloch band of an optical lattice. *Phys. Rev. A*, **72**, 053604 (2005).

[196] L. Krinner. Private Communication. (July 2015).

[197] I. de Vega, D. Porras, and J. I. Cirac. Matter-Wave Emission in Optical Lattices: Single Particle and Collective Effects. *Phys. Rev. Lett.*, **101**, 260404 (2008).

[198] M. Bruderer, A. Klein, S. Clark, and D. Jaksch. Polaron physics in optical lattices. *Phys. Rev. A*, **76** (2007).

[199] F. Grusdt, A. Shashi, D. Abanin, and E. Demler. Bloch oscillations of bosonic lattice polarons. *Phys. Rev. A*, **90**, 063610 (2014).

[200] A. Klein, M. Bruderer, S. R. Clark, and D. Jaksch. Dynamics, dephasing and clustering of impurity atoms in Bose-Einstein condensates. *New J. Phys.*, **9**, 411 (2007).

[201] M. Schecter, D. M. Gangardt, and A. Kamenev. Dynamics and Bloch oscillations of mobile impurities in one-dimensional quantum liquids. *Ann. Phys.*, **327**, 639 (2012).

[202] C. J. M. Mathy, M. B. Zvonarev, and E. Demler. Quantum flutter of supersonic particles in one-dimensional quantum liquids. *Nature Phys.*, **8**, 881 (2012).